An introduction to the two-scale homogenization method for seismology

Yann Capdeville, Paul Cupillard, Sneha Singh

Capdeville, Y., P. Cupillard, and S. Singh (2020). Chapter six - an introduction to the two-scale homogenization method for seismology. In B. Moseley and L. Krischer (Eds.), *Machine Learning in Geosciences*, Volume 61 of *Advances in Geophysics*, pp. 217 – 306. Elsevier.

An introduction to the two-scale homogenization method for seismology

Y. Capdeville[1], P. Cupillard[2], S. Singh[1]

[1] *LPG, CNRS, Université de Nantes, France*
[2] *GeoRessources, Université de Lorraine, France*

Abstract

The Earth is a multi-scale body meaning small scales cannot be avoided in geophysics, particularly in seismology. In this paper, we present an introduction to the two-scale non-periodic homogenization method, which is designed to deal with small scales, both for the forward and the inverse problems. It is based on the classical two-scale periodic homogenization, which requires a periodic or a stochastic media, but has been extended to geological media, which are deterministic and multi-scale with no scale separation. The method is based on the minimum wavelength of the wavefield to separate the scales. It makes it possible to compute an effective medium, valid up to a given maximum source frequency, from a given fine-scale description of a medium. The effective medium is in general fully anisotropic and smooth but not constant. It can be tuned so that the wavefield computed in the effective medium is the same as the true solution up to the desired accuracy for all waves, including reflected, refracted or surface waves. For inverse problems, we will numerically check that a limited frequency band full waveform inversion can retrieve, at best, only the homogenized medium and not the true fine-scale one. We will first present the subject through a numerical experiment in 1-D. Then, we will present the method in 1-D and next in 2-D/3-D. Finally, we will present a series of examples in 2-D and 3-D in the forward modeling and inverse problem contexts.

Keywords: Acoustic Waves, Effective Solution, Elastic Waves, Full Waveform Inversion, Helmholtz Resonator, Homogenization, Multi-scales, Numerical Modeling, Rotational Seismology, Seismology, Synthetic seismograms, Up-scaling

1 Introduction

The Earth is a multi-scale medium: whatever the scale we place ourselves at, there are always heterogeneities of smaller scales. Looking at a cross-section of the global Earth, we would probably see the main layers (crust, mantle, core) along with slabs and plumes. Zooming in on a subduction zone, we would see an accretion prism, magma chambers below volcanoes and more details within the crust. Zooming in again on the shallow crust, we would see thinner layers along with faults and fractures. Zooming in again, we would see grains of many different materials, pores, and

so on and so forth. So, the Earth is definitely multi-scale, but it is also a deterministic medium (as opposed to a stochastic medium): there is only one Earth.

The fact that the Earth is a multi-scale body could be a serious problem for many Earth sciences, including seismology. If one had to know all details about the Earth to model body wave arrival times or frequency band limited seismograms, seismology would not be very useful. Fortunately, it is well known that, somehow, simple Earth models such as PREM (Dziewonski & Anderson, 1981) can model body wave time-arrivals and low-frequency seismic data with a surprising accuracy. Therefore, it is clear that an underlying homogenization process (also called up-scaling or effective process) exists for seismic wave propagation, which makes it possible to model the real Earth with a simple effective media.

For decades, implicitly knowing that a homogenization process exists but having no mathematical theory for this process has been enough. Nowadays, with the emergence of more and more precise modeling tools and inversion techniques, the lack of this theory is becoming a problem. For the forward modeling case, the numerical cost of a simulation in a smooth 3-D medium is directly linked to the maximum frequency emitted at the source (or, equivalently, the inverse of the minimum wavelength) to the power 4. But in a rough medium, the numerical cost is proportional to the inverse of the smallest scale size to the power 4, regardless of the maximum frequency of the source. Therefore, scales smaller than the minimum wavelength can be extremely expensive numerically. They can even make the modeling impossible when the mesh cannot be designed because of the medium complexity. To overcome these issues, the ability to remove small scales to work with a smooth effective medium, whatever the complexity of the original medium, would be a great advantage. For the inverse problem, we know that the media we are trying to image always contain scales below the resolution limit. Understanding the relationship between the small scales and the scales we are can image is a necessity.

A practical example of the reason why this missing tool can be a problem is the following: when working on the very early stage of global scale Full Waveform Inversion (FWI) (Capdeville et al., 2005), the first author of this work faced a difficulty because of the thin layers of the crust. An important ingredient for a successful inversion is a good quality starting model. Because of computing limitations in the early 2000's, the inversion was carried out with very long period data (150 s and above) that led to very long wavelengths (about 600 km and longer). For such long period data, PREM is an appropriate starting model. The problem is that PREM has a 9 km thick lower-crust, which is very small compared to the minimum wavelength of 600 km. This difference in scales poses a serious problem for both the forward modeling (the small layer drastically increases the numerical cost necessary to solve the wave equation with modern solvers) and the inverse problem (the small layer imposes a very fine parameterization, leading to an ill-posed inverse problem).

When facing such a difficulty, it is tempting to remove the small layer or to average it ("it is so small, it should not matter..."). However, these trivial solutions have a surprisingly strong effect on the waveforms, especially on surface wave phase velocities, making them an invalid option (Capdeville & Marigo, 2008). When looking

for a solution (which was the starting point of the present work actually), it appeared that an entire scientific field is dedicated to finding effective or homogenized solutions for different types of equations. The science of dealing with small scales to find effective behaviors, also called homogenization, has been in existence since the sixties. The literature on this subject is very vast and gathers thousands of publications. We do not attempt to give an exhaustive review of this field here but we provide some broad outlines instead.

There are many different approaches to solve the problem of finding effective behaviors. The first one is the two-scale homogenization, or formal asymptotic homogenization analysis (Babuška, 1976; Bensoussan et al., 1978; Sanchez-Palencia, 1980; Murat & Tartar, 1985). It is the method on which the present work is based upon. It involves an explicit scale separation between large and small scales and the introduction of two space variables, one for the large scales and one for the small scales. It is often considered as a mathematical approach because theorems of convergence exist (e.g. Allaire, 1992). However, this method is not exact: it is asymptotic and, as such, it implies some approximations to be applied to practical cases. An advantage of this method is that it can deal with periodic, quasi-periodic, and stochastic (Papanicolaou & Varadhan, 1979) heterogeneous media. A second approach is the variational approach, or the Willis approach (Hashin, 1972; Willis, 1981, 1983). It does not involve an explicit scale separation and it is often dedicated to finding bounds of effective elastic properties of complex material. It does not rely on any specific approximation but it often leads to non-local effective behavior, both in space and time, which makes it difficult to use in practice (Willis, 1985, 2009). Many other approaches, such as the volume average approach (Pride et al., 1992) which is more intuitive and physical, the theory of mixtures (Bowen, 1976) and the numerical homogenization (Engquist & Souganidis, 2008), also exist. Finally, several works have been dedicated to comparing and connecting some of these approaches (see, for instance, Davit et al., 2013; Nassar et al., 2016; Meng & Guzina, 2018).

Many classes of problems are tackled with those various methods, like obtaining bounds of composite materials (e.g. Hashin & Shtrikman, 1962; Hill, 1965; Willis, 1981; Francfort & Murat, 1986) or porous media (Auriault & Sanchez-Palencia, 1977; Burridge & Keller, 1981; Auriault et al., 1985; Boutin & Auriault, 1990; Pride et al., 1992), elasto-dynamics (e.g. Sanchez-Palencia, 1980; Boutin & Auriault, 1993; Willis, 1997), elastic rupture (e.g. Abdelmoula & Marigo, 2000) and so on.

The Earth science communities, including seismology, have long remained mostly aloof from these methods. Nevertheless, some important contributions have been made. One of the main ones is Backus (1962) (often named the "Backus averaging method"), which is dedicated to the upscaling of finely layered media for elastic waves in the low-frequency (long-wavelength) regime. Among other results, Backus has shown that a finely layered isotropic medium gives, in general, an anisotropic effective medium. This is the apparent anisotropy of layered media, which is often seen in nature. Interestingly, the Backus method does not require any hypothesis apart from handling a layered medium (no periodicity requirement, no scale sepa-

ration hypothesis, etc). Since then, some works have been dedicated to improving and attempting to generalize Backus' results (Gold et al., 2000; Grechka, 2003), mostly for exploration geophysics applications (see Tiwary et al. (2009) for a review of layered media upscaling in that domain), without trying to reach the rigor or the quality of the two-scale periodic homogenization method. Similarly, effective elastic properties of mineral media for geophysical applications have been derived from the classical Voigt-Reuss averages (e.g. Thomsen, 1972) and from the Hashin-Shtrikman bounds (e.g. Watt, 1988).

To sum up, keeping in mind that geological media are neither periodic nor stochastic and heterogeneities have no natural scale separation, the situation in the early 2000's offered no option to upscale general geological media for the seismic (elastic or acoustic) wave equation. Going back to the global scale FWI example mentioned above, the first non-naive upscaling attempt was to apply the Backus averaging. While the Backus averaging gives good results for the volume and body waves, it gives deceivingly poor results for shallow layers and the surface waves. Unfortunately, the Backus approach does not provide any direction to go beyond its results. Moreover, solutions provided by the two-scale homogenization community are limited to periodic heterogeneities (Dumontet, 1990; Marigo & Pideri, 2011). The first successful attempt to mix the periodic homogenization approach and the Backus method (at least the fact that it does not require a periodicity hypothesis) was made by Capdeville and Marigo (2007, 2008) for layered media. It shows that the order 0 two-scale homogenization falls back to Backus' results (which was known for long, see for instance Sanchez-Palencia (1980), or more recently Guillot et al. (2010) and C. Lin et al. (2017)) and it makes it possible to go beyond the leading order. This was an improvement, but not yet the desired general solution, as it was limited to the layered case.

To go further, a more general solution has been proposed in 1-D (Capdeville et al., 2010a), then in 2-D (Capdeville et al., 2010b), and finally in 3-D (Capdeville et al., 2015; Cupillard & Capdeville, 2018). Note that alternative approaches have been developed by Fichtner and Hanasoge (2017) in 1-D and Jordan (2015). Homogenization of a rapid topography has been treated by Capdeville and Marigo (2013) and the effect of small scale heterogeneities on seismic sources, more specifically on explosions, by Burgos et al. (2016). Finally, an important emerging topic is the link between the seismic inversion problem and homogenization for full waveform imaging techniques (Capdeville et al., 2013; Afanasiev et al., 2016; Capdeville & Métivier, 2018) and for downscaling and interpreting of seismic results (Fichtner et al., 2013; Wang et al., 2013; Bodin et al., 2015; Alder et al., 2017; Faccenda et al., 2019).

The objective of this work is to propose an introduction to the two-scale homogenization method, in the periodic case first, then in the non-periodic case, and demonstrate its applications to seismology. Homogenization is a non-intuitive approach that can be difficult to step into for someone with a background in geophysics. Not everyone likes it; for example, S. Pride leaves the following comment about it in Pride et al. (1992): "However, the entire (possibly confusing) notion of having all

quantities functionally depend on two independent length scales and of performing asymptotic expansions is unnecessary when direct volume averaging proceeds so directly". Nevertheless, we hope to convince the readers that the gain of such an approach is worth the effort. The first part is dedicated to some mathematical notions that will be useful for the rest of the paper. The second part is dedicated to a numerical experiment in 1-D. This 1-D introduction has no real application but it is meant to show where the idea of the two-scale variables comes from and why it is useful to introduce it. It is also the occasion to introduce Backus' solution. The third part is dedicated to the formal two-scale homogenization in the 1-D periodic case. It is the simplest case and it makes the first contact to the classical two-scale homogenization as simple as it can be. We then move to the 1-D non-periodic case. Once again, there is no real application of this 1-D case, but it is the simplest way to introduce the necessary concepts. The sixth part is dedicated to the 2-D and 3-D cases. Finally, the last part is dedicated to examples and applications of non-periodic homogenization.

2 Mathematical notions and notations

Before getting started, let us introduce some simple mathematical notions and notations that will be useful throughout the paper.

2.1 Periodic functions

Homogenization strongly relies on periodic functions, at least in its classic form. In 1-D, a T-periodic function h is such that, for any x, $h(x+T) = h(x)$. In d dimensions, where d is 2 or 3 for 2-D or 3-D respectively, a function h is $\mathbf{T}$-periodic if, for any $\mathbf{x}$ and for any $i \in \{1, ..., d\}$, $h(\mathbf{x}+T_i\hat{\mathbf{i}}) = h(\mathbf{x})$ with no implicit summation on i and where the $\hat{\mathbf{i}}$ are the space basis unit vectors.

2.2 Two-variable functions

Homogenization makes the scale separation explicit by using two spatial variables: one for the large scales and one for the small scales. In practice, it implies the use of two-scale functions. A two-scale function $h(x, y)$ is a function that depends on two space variables x and y. It is usually periodic for the second variable.

Assuming h is T-periodic in y, we define the "cell average" as

$$\langle h \rangle (x) = \frac{1}{T} \int_0^T h(x, y) dy \,. \tag{1}$$

At this stage, the notion of "cell" is not yet defined. Here, it is one periodicity T. The following properties of h will be useful:

$$\partial_y h = 0 \Leftrightarrow h(x, y) = \langle h \rangle (x) \tag{2}$$

and

$$\langle \partial_y h \rangle = 0\,. \tag{3}$$

Both properties can be demonstrated using the T-periodicity and an integration by parts.

Finally we define $\mathcal{T}$, the functional space of two-variable functions λ_{min}-periodic for the second variable, where λ_{min} is the minimum wavelength of the wavefield (defined in the next section).

2.3 Linear filtering and Fourier domain

It is useful, for any function $h(x)$, to define its wavenumber domain version:

$$\bar{h}(k) = \int_{-\infty}^{+\infty} h(x) e^{\mathrm{i}2\pi k x} dx\,, \tag{4}$$

where k is the spatial frequency and $\lambda = 1/k$ its corresponding wavelength. $\bar{h}$ is the Fourier transform of h; it is a complex function.

One of the important physical scales is the wavefield minimum wavelength λ_{min} to which we can associate the maximum spatial frequency $k_{\text{max}} = 1/\lambda_{\text{min}}$. In the following, we will often use an arbitrarily user-defined wavelength λ_0 and we will measure its position relative to λ_{min} with

$$\varepsilon_0 = \frac{\lambda_0}{\lambda_{\text{min}}}\,. \tag{5}$$

λ_0 is used to define what can be considered fine scales and what can be considered large scales. It is usually small with respect to 1.

We will also make extensive use of linear filtering, mainly low-pass filtering, mostly in the space domain. We introduce a low-pass filter $\mathcal{F}^{\varepsilon_0}$ to be applied in the space domain such that, for any function $h(x)$,

$$\mathcal{F}^{\varepsilon_0}(h)(x) = \int_{-\infty}^{+\infty} h(x') w_{\varepsilon_0}(x - x') dx'\,, \tag{6}$$

where w_{ε_0} is the filter wavelet. There are many types of wavelets with different properties. For low-pass filters, the wavelet is such that its convolution with h removes all spatial variations smaller than λ_0 in $\mathcal{F}^{\varepsilon_0}(h)$. In our notation, i.e. $\mathcal{F}^{\varepsilon_0}$, we emphasize the dependency of the filter to ε_0 instead of λ_0 because we will be working with a fixed λ_{min}.

In the wavenumber domain, the linear low-pass filtering is simply a product:

$$\bar{\mathcal{F}}^{\varepsilon_0}(h)(k) = \bar{h}(k) \bar{w}_{\varepsilon_0}(k)\,. \tag{7}$$

The low-pass filter wavelet is defined such that its amplitude spectrum $|\bar{w}_{\varepsilon_0}|(k)$ is equal to 1 in $[0, k_0]$ (where $k_0 = 1/\lambda_0$) and then goes down to 0 more or less sharply

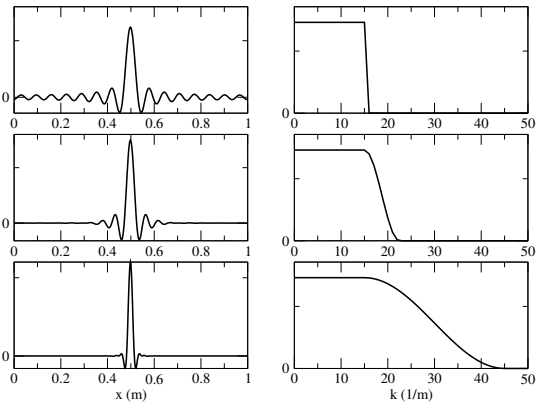

Figure 1: Low-pass filter wavelet w_{ε_0} in the space domain (left) and its spectrum norm $|\bar{w}_{\varepsilon_0}|$ in the spatial frequency domain (right) for different apodizations. The smoother is the spectral apodization, the more compact is the spatial support of the wavelet.

(apodization) depending on the desired support size of the wavelet in the space domain (Fig. 1).

Based on this low-pass filter, we can introduce the notion of "smooth functions" and "rough functions":

- h is said to be smooth if $\mathcal{F}^{\varepsilon_0}(h) = h$. In other words, a smooth function has no spatial variations smaller than λ_0;
- h is said to be rough if $\mathcal{F}^{\varepsilon_0}(h) \neq h$.

We will also make use of the following properties:

i) partial derivatives and $\mathcal{F}^{\varepsilon_0}$ commute, meaning that

$$\mathcal{F}^{\varepsilon_0}\left(\frac{\partial h}{\partial x}\right) = \frac{\partial \mathcal{F}^{\varepsilon_0}(h)}{\partial x}\,, \tag{8}$$

ii) if h is smooth, then for any function g we have

$$\mathcal{F}^{\varepsilon_0}(hg) \simeq h\mathcal{F}^{\varepsilon_0}(g). \tag{9}$$

Note that, for two rough functions h and g, $\mathcal{F}^{\varepsilon_0}(hg) \neq \mathcal{F}^{\varepsilon_0}(h)\mathcal{F}^{\varepsilon_0}(g)$.

In the case of a two-scale function $h(x, y)$, low-pass filters are always applied to the second variable. Even though x and y are independent variables, as we will see later on, in the homogenization theory, y is built from x with the relation $y = x/\varepsilon_0$. This relation also applies in the spectral domain and therefore, to obtain a similar low-pass filtering effect in the y domain like in the x domain, the λ_0 cutoff (for a

function of x) becomes $\lambda_{\min}$ (for a function of y). Indeed, in the y domain, the filter wavelet w_1 is related to w_{ε_0} by $w_1(y) = \varepsilon_0 w_{\varepsilon 0}(\varepsilon_0 y)$. The cutoff of w_1 is therefore $\lambda_1 = \lambda_0/\varepsilon_0 = \lambda_{\min}$ (the corresponding ε_0 is indeed 1). For a two-scale variable, the filtering is therefore independent of ε_0 and is simply noted.

$$\mathcal{F}(h)(x,y) = \int_{-\infty}^{+\infty} h(x,y') w_1(y-y')\, dy' \,. \tag{10}$$

To exemplify the equivalence of the two domain filtering, let us take a simple function $g(y) = h(\varepsilon_0 y)$. Then

$$\begin{aligned}
\mathcal{F}(g)(y) &= \int_{-\infty}^{+\infty} g(y') w_1(y-y')\, dy' && (11)\\
&= \int_{-\infty}^{+\infty} g\left(\frac{x'}{\varepsilon_0}\right) w_1\left(\frac{x-x'}{\varepsilon_0}\right) \frac{dx'}{\varepsilon_0} && (12)\\
&= \int_{-\infty}^{+\infty} h(x') w_{\varepsilon_0}(x-x')\, dx' && (13)\\
&= \mathcal{F}^{\varepsilon_0}(h)(x) && (14)\\
&= \mathcal{F}^{\varepsilon_0}(h)(\varepsilon_0 y)\,. && (15)
\end{aligned}$$

Applying $\mathcal{F}$ to g indeed gives the same result as applying $\mathcal{F}^{\varepsilon_0}$ to h.

2.3.1 Arithmetic and harmonic averages

For any T-periodic function $h(x)$, the arithmetic average is

$$\langle h \rangle = \frac{1}{T} \int_0^T h(x) dx \tag{16}$$

and the harmonic average is

$$\langle h \rangle_H = \left(\frac{1}{T} \int_0^T \frac{1}{h}(x) dx \right)^{-1} . \tag{17}$$

These two averages can give significantly different results. For instance, let us assume a 2-periodic function $h(x)$ such that $h(x) = a$ for $x \in [0,1)$ and $h(x) = b$ for $x \in [1,2)$. The arithmetic average of this function is $\langle h \rangle = (a+b)/2$ whereas the harmonic average is $\langle h \rangle_H = \frac{2ab}{a+b}$. Taking some values for a and b, we see how different $\langle h \rangle$ and $\langle h \rangle_H$ can be:

- $a = 1.01;\ b = 0.99 \ \Rightarrow\ \langle h \rangle = 1;\ \langle h \rangle_H = 0.99990$
- $a = 1.10;\ b = 0.90 \ \Rightarrow\ \langle h \rangle = 1;\ \langle h \rangle_H = 0.990$
- $a = 1.20;\ b = 0.80 \ \Rightarrow\ \langle h \rangle = 1;\ \langle h \rangle_H = 0.960$
- $a = 1.50;\ b = 0.50 \ \Rightarrow\ \langle h \rangle = 1;\ \langle h \rangle_H = 0.750$

Even though the low-pass filtering $\mathcal{F}^{\varepsilon_0}$ we are going to use in this article is different from the cell average $\langle\,\rangle$, the conclusion we are drawing holds for $\mathcal{F}^{\varepsilon_0}$.

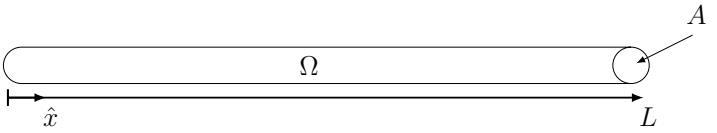

Figure 2: A 1-D bar of length L and section A along the $\hat{x}$ axis.

3 A numerical introduction to the subject

This section is dedicated to a numerical experiment in 1-D. It has little equivalence in the real world but it aims at gradually bringing the reader, through observations of numerical results in a simple setting, to ideas behind the two-scale homogenization method.

3.1 A simple example in 1-D

Now that the mathematical notions have been exposed, we present some trivial numerical experiments to introduce the subject. Let us take a very simple example: a 1-D elastic wave propagating in a 1-D bar with periodic heterogeneities. Let Ω be a fine and long cylinder of length L and section A (Fig. 2). We assume that the radius of the section is very small compared to the wavelength of the wave we are about to consider so that any displacement of any particle in Ω which is not parallel to the bar can be neglected. Let $u(x,t)$ be the displacement of the particle (relative to a position at rest) along the $\hat{x}$ direction as function of x and time t. If an internal force $F(x,t)$ is applied in the bar along the $\hat{x}$ axis, we define the stress σ as

$$\sigma(x,t) = \frac{F(x,t)}{A} \tag{18}$$

We assume that we are in the linear elasticity regime so that a linear relationship between the stress and the strain $\epsilon(x,t) = \partial_x u(x,t)$ exits:

$$\sigma(x,t) = E\partial_x u(x,t)\,, \tag{19}$$

where E is the Young modulus (or the elastic coefficient). This last equation is the material constitutive equation, also called the Hooke's law. Based on Newton's second law, the dynamics equation in the bar is

$$\rho(x)\partial_{tt}u(x,t) - \partial_x\sigma(x,t) = f(x,t)\,, \tag{20}$$

where ρ is the mass per unit length of the bar, $\partial_{tt}u$ the second time derivative of u and f an external force applied to the bar. We assume free stress conditions at both ends

$$\sigma(0,t) = \sigma(L,t) = 0\,, \tag{21}$$

and we assume the bar is at rest at $t = 0$. Equations (20) and (19) together with the boundary conditions (21) make the elastic wave equation in the 1-D bar Ω.

We use a point source located in x_0:

$$f(x,t) = \delta(x - x_0)g(t)\,, \tag{22}$$

where $g(t)$ is the source time wavelet. Here, we use a Ricker function (second derivative of a Gaussian) which can be characterized by its central frequency f_0. The maximum frequency of such a wavelet can be estimated as $f_{\text{max}} \simeq 3f_0$.

Before moving forward, we need to introduce the notion of minimum wavelength λ_{min} associated to f_{max}. Assuming homogeneous mechanical properties and a monochromatic wave of type $u(x,t) = Ue^{i(2\pi kx - \omega t)}$, where ω is the angular frequency and U is the amplitude, equations (19) and (20) leads to the dispersion relation

$$k = \frac{\omega}{2\pi\alpha}\,, \tag{23}$$

where $\alpha = \sqrt{E/\rho}$ is the wave velocity. Note that, in this work, k is the spatial frequency and not the more standard wavenumber (if k was the wavenumber, then the dispersion relation would be $k = \omega/\alpha$). Using the last equation along with $k = 1/\lambda$ and $\omega = 2\pi f$, we find

$$\lambda_{\text{min}} = \frac{\alpha}{f_{\text{max}}}\,. \tag{24}$$

This last equation shows that, for a source with a limited frequency band (i.e. with a maximum frequency f_{max}), the wavefield does not have oscillations smaller than λ_{min}. Note that this is only true in the far-field, i.e a few minimum wavelengths away from the point source. For heterogeneous media, the dispersion relation might be difficult to establish analytically, but it always exists and it is bounded (with a few exceptions in some very particular media, such as metamaterials, see section 8.3 for instance). In general, we can obtain an estimate of the lower bound of λ_{min} using

$$\lambda_{\text{min}} = \frac{\alpha_{\text{min}}}{f_{\text{max}}}\,, \tag{25}$$

where α_{min} is the minimum wave velocity. The minimum wavelength is very useful for solving the wave equation numerically as it provides an estimate of the regularity of the solution, which is always necessary to calibrate the grid spacing of the mesh that comes with the numerical method. It is also very important for the homogenization process because what is small and what is large is determined with respect to λ_{min}.

To solve the wave equation (19-21) in the heterogeneous bar, we rely on the Spectral Element Method (SEM) (Komatitsch & Vilotte, 1998; Chaljub et al., 2007). A good introduction to the method can be found in Igel (2017). SEM is a type of high-degree finite-element method. It has many advantages but the one that interests us the most is its ability to accurately take into account material discontinuities

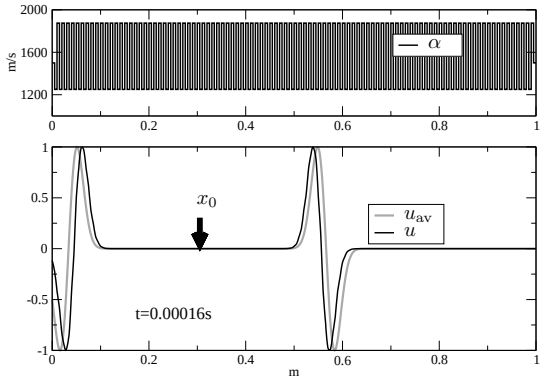

Figure 3: Top: periodic wave speed α along the bar. Bottom: snapshots of the displacement u computed in the bar with the periodic heterogeneity and of the displacement u_{av} computed in a 1-D bar with the average velocity $\langle\alpha\rangle$ for $t = 0.16\,\text{ms}$.

if they are matched by an element boundary. By meshing all the bar mechanical discontinuities, we can obtain a solution accurate enough to be used as a reference solution.

We now assume that the mechanical properties $\rho(x)$ and $E(x)$ vary periodically with a ℓ-periodicity along x and we assume ℓ is smaller than λ_{min}. We take $\ell = 0.01\,\text{m}$ and we set up the properties such that the wave velocity $\alpha(x)$ jumps from $1.25\,\text{km/s}$ to $1.875\,\text{km/s}$ with a ℓ-periodicity (Fig. 3). The corresponding average velocity is $\langle\alpha\rangle = 1.562\,\text{km/s}$. We use a source at $x_0 = 0.3\,\text{m}$ and with $f_0 = 20\,\text{kHz}$ corresponding to $\lambda_{\text{min}} = 0.02\,\text{m}$. Finally, we choose $L = 1\,\text{m}$. In Fig. 3, two snapshots of the displacement along $\hat{x}$ for a time $t = 0.16\,\text{ms}$ are shown: one computed in the periodic heterogeneous bar and one in the average velocity bar. We observe that the wave pulses have a very similar shape in the two cases, even though they seem to propagate at a different speed. It appears that, for the heterogeneous case, the waves propagate the same way as in a homogeneous bar: no scattering or dispersion are observed. Therefore, it seems that an effective propagation occurs. The second observation is that this effective wave propagation has a different wave speed than the average wave speed, which is counter-intuitive. It is interesting to note that the true effective wave propagation is slower than the average wave speed, which is consistent with the "velocity shift" experimentally observed when comparing time arrivals of waves propagating in random media to time arrivals computed with the corresponding average velocity (Shapiro et al., 1996).

From this simple example, we conclude that an effective wave propagation occurs, but it does not correspond to a propagation in a simple average velocity model. We need to understand this mismatch; this is the starting point of this work.

3.2 Small scales heterogeneities and solution smoothness

Based on the observations from the previous section and before moving forward, we make a slight change in notations. In this work, we have two types of scales: the small scales, that are much smaller than λ_{min}, and the large scales, that are comparable or larger than λ_{min}. In reality, it is not obvious to tell what small and large scales are. Only the periodic case makes this distinction simple. We introduce ε, a parameter that somehow measures how small the small scales are compared to λ_{min}. For periodic heterogeneities, it is simply defined as

$$\varepsilon = \frac{\ell}{\lambda_{\text{min}}}\,, \tag{26}$$

where ℓ is still the medium heterogeneity periodicity. For more general heterogeneities (non periodic), there is no simple definition of ε; let us say for now that ε is just a symbol indicating that a given quantity depends on the small scales. A priori, if the mechanical properties contain small scales, all quantities of the problem also depend on the small scales. We, therefore, rewrite the wave equation as

$$\rho^\varepsilon \partial_{tt} u^\varepsilon - \partial_x \sigma^\varepsilon = f^\varepsilon\,, \tag{27}$$

$$\sigma^\varepsilon = E^\varepsilon \partial_x u^\varepsilon\,. \tag{28}$$

Based on the example in the previous section, it appears that effective quantities exist: we will mark them with an *. For example, u^* is the effective displacement. Using the ''averaging operator" $\mathcal{F}^{\varepsilon_0}$ we can define the effective solution to the wave equation:

$$u^* = \mathcal{F}^{\varepsilon_0}(u^\varepsilon)\,, \tag{29}$$

$$\sigma^* = \mathcal{F}^{\varepsilon_0}(\sigma^\varepsilon)\,, \tag{30}$$

$$\epsilon^* = \mathcal{F}^{\varepsilon_0}(\epsilon^\varepsilon)\,. \tag{31}$$

In the following, we choose $\varepsilon_0 > \varepsilon$ such that, for any purely periodic function h^ε, $\mathcal{F}^{\varepsilon_0}(h^\varepsilon)$ is a constant function in x.

3.3 The Backus solution

To analyze the observation made in the previous section, we use the Backus approach to obtain effective media. Backus (1962) indeed developed an elegant solution to upscale finely layered media and obtained widely used results. While his work has been developed for layered media for wave propagation in 3-D, we will apply it to our 1-D case. His method is based on applying a low-pass filter to the wave equation. To do so, Backus determines whether the parameters u^ε, $\partial_x u^\varepsilon$ and σ^ε are smooth or rough based on mathematical arguments. Here, we rely on a simple numerical observation instead of mathematical arguments: in Fig. 4, snapshots of displacement, strain, and stress for an elastic wave propagating in the finely layered bar used in section 3.1 are plotted. One can notice that the displacement and the

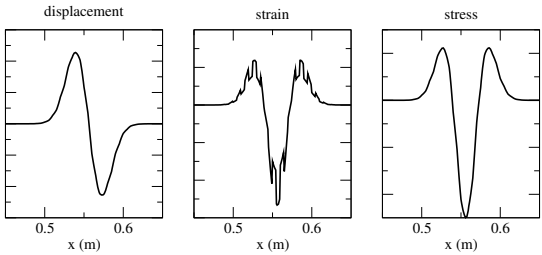

Figure 4: Snapshots of displacement u^ε (left), strain $\partial_x u^\varepsilon$ (middle) and stress σ^ε (right) for an elastic wave propagating in the periodic heterogeneities used in section 3.1.

stress are smooth, meaning that their variations are on scales larger than those of the heterogeneities. The strain, however, displays a large scale variation on which changes at the scale of the heterogeneity layering is superimposed.

In the next step, Backus applies $\mathcal{F}^{\varepsilon_0}$ to the dynamic equation (20) without its second member f:

$$\mathcal{F}^{\varepsilon_0}\left(\rho^\varepsilon \partial_{tt} u^\varepsilon - \partial_x \sigma^\varepsilon\right) = 0\,. \tag{32}$$

Using the linearity of the low-pass filter operator, we have

$$\mathcal{F}^{\varepsilon_0}(\rho^\varepsilon \partial_{tt} u^\varepsilon) - \mathcal{F}^{\varepsilon_0}(\partial_x \sigma^\varepsilon) = 0\,. \tag{33}$$

We know that u^ε is a smooth function (see Sec. 2.3 for a definition of smooth and rough functions), therefore

$$u^* = \mathcal{F}^{\varepsilon_0}(u^\varepsilon) = u^\varepsilon\,. \tag{34}$$

Using this last equation along with (9), it comes

$$\mathcal{F}^{\varepsilon_0}(\rho^\varepsilon \partial_{tt} u^\varepsilon) = \mathcal{F}^{\varepsilon_0}(\rho^\varepsilon)\partial_{tt} u^*\,. \tag{35}$$

Note that, to obtain the last equation, we ignored the time derivatives. This is expected because the filter only acts on space.

Using (8) and the fact that σ^ε is smooth, we have

$$\mathcal{F}^{\varepsilon_0}(\partial_x \sigma^\varepsilon) = \partial_x \mathcal{F}^{\varepsilon_0}(\sigma^\varepsilon)\,, \tag{36}$$

$$= \partial_x \sigma^*\,. \tag{37}$$

Finally, putting together (33), (35) and (37), we obtain

$$\mathcal{F}^{\varepsilon_0}(\rho^\varepsilon)\partial_{tt} u^* - \partial_x \sigma^* = 0\,. \tag{38}$$

The above equation is the effective dynamic equation, and we can see that the effective density is simply

$$\rho^* = \mathcal{F}^{\varepsilon_0}(\rho^\varepsilon)\,. \tag{39}$$

We now move to the constitutive relation (28). Applying the same recipe like the one we just applied, it comes

$$\mathcal{F}^{\varepsilon_0}(\sigma^\varepsilon) = \mathcal{F}^{\varepsilon_0}(E^\varepsilon \partial_x u^\varepsilon)\,. \tag{40}$$

We get stuck here because the right-hand term is the product of E^ε and $\partial_x u^\varepsilon$ which are two rough functions. In that case, property (9) does not apply and we cannot obtain an effective equation. To get around this difficulty, Backus noticed that, in the 1-D or layered case, the constitutive relation can be rewritten as

$$\partial_x u^\varepsilon = \frac{1}{E^\varepsilon}\sigma^\varepsilon\,. \tag{41}$$

We now have, on the right-hand term of the last equation, the product of a rough function ($1/E^\varepsilon$) with a smooth function (σ^ε). Therefore, property (9) can be used, and applying the filter to the last equation leads to

$$\partial_x u^* = \mathcal{F}^{\varepsilon_0}\left(\frac{1}{E^\varepsilon}\right)\sigma^*\,. \tag{42}$$

We finally obtain the effective constitutive relation:

$$\sigma^* = E^* \partial_x u^* \tag{43}$$

with

$$E^* = \left(\mathcal{F}^{\varepsilon_0}\left(\frac{1}{E^\varepsilon}\right)\right)^{-1}\,. \tag{44}$$

Contrary to the density, the effective Young modulus is not the trivial linear filtering of the fine-scale Young modulus. This non-trivial relation is responsible for the difference of wave speeds observed in Fig. 3 and it comes from the difference between the arithmetic and the harmonic average (see Sec. 2.3.1). In the example presented in Sec. 2.3.1, we see that the larger the contrast between a and b, the larger the difference between the two averages. Moreover, we see that the harmonic average is systematically smaller than the arithmetic average. This fact is at the root of the observation showing that true wave propagation is always slower than the propagation in the average velocity media. Similarly, the difference between these two averages is at the origin of the effective anisotropy often observed in nature for finely layered media.

To wrap-up this section, with simple linear filtering rules, Backus found that the effective displacement u^* and stress σ^* are driven by

$$\rho^* \partial_{tt} u^* - \partial_x \sigma^* = 0\,, \tag{45}$$

$$\sigma^* = E^* \partial_x u^*\,, \tag{46}$$

with

$$\begin{aligned} \rho^* &= \mathcal{F}^{\varepsilon_0}(\rho) \\ E^* &= \left(\mathcal{F}^{\varepsilon_0}\left(\frac{1}{E^\varepsilon}\right)\right)^{-1}\,. \end{aligned} \tag{47}$$

Note that Backus does not say anything about the source.

If we apply the Backus formula (47) to the example of the periodic bar in Sec. 3, using $\varepsilon_0 = 0.5$, we obtain a constant effective model with an effective velocity $\alpha^* = \sqrt{E^*/\rho^*}$ which is plotted in Fig. 5a . As expected, it can be seen that α^* is not the average velocity (it is not the average slowness either). A snapshot of the reference displacement u^ε computed in the periodic bar and of the Backus effective displacement u^* computed in the Backus effective bar (Fig. 5b) display a good agreement. The time shift observed in Fig. 3 has gone. Because the Backus solution does not require a periodicity hypothesis of the mechanical properties, we can go further and generate a bar with random mechanical properties (it is, nonetheless, a deterministic case: the bar is generated only once). The resulting velocity and its Backus effective version are shown in Fig. 5c. A snapshot of the reference displacement u^ε computed in the random bar and of the Backus effective displacement u^* computed in the Backus effective bar (Fig. 5d) display, once again, a good agreement.

The Backus (1962) method described here can be applied to a more general case, namely layered media (i.e. a 1-D variation of the properties and 3-D wave propagation) with transversely isotropic elastic properties. Such media carry P and S waves. Beyond the technical aspect of obtaining effective media, Backus (1962) shows that the long-wavelength effective medium of fine isotropic layers is anisotropic in general: this is the so-called apparent anisotropy. For the S waves, two effective parameters come out:

$$L = \left\langle \frac{1}{\mu} \right\rangle^{-1} , \tag{48}$$

$$N = \langle \mu \rangle , \tag{49}$$

where μ is the second Lamé coefficient and the elastic parameters L and N can be related to the vertically (SV) and horizontally (SH) polarized S waves, respectively, with wave speeds $\alpha_{SV} = \sqrt{L/\rho}$ and $\alpha_{SH} = \sqrt{N/\rho}$. Due to the difference between harmonic and arithmetic averages mentioned earlier, α_{SH} and α_{SV} are different in general: this is the shear wave anisotropy. The P wave case is more complex, as shown in Backus (1962).

3.4 Beyond the Backus solution

If we take a closer look at the Backus effective solution and compare it to the reference solution, some differences can still be observed. In Fig. 6, on the left panel, a zoom on the displacement propagating in the 1-D periodic bar, for two different ℓ-periodicities (and, consequently, for two different ε), is plotted. One can notice that the observed differences depend upon ε. In Fig. 6, on the right panel, the residuals $u^\varepsilon - u^*$ for $\varepsilon = 0.5$ and $\varepsilon = 0.25$ are plotted. We see that each residual is the product of a smooth function and a function with fine-scale variations. The amplitude of the smooth function looks proportional to ε, and its variation in x seems independent of ε. On the contrary, the small-scale variations in x look directly tied to ε. Moreover,

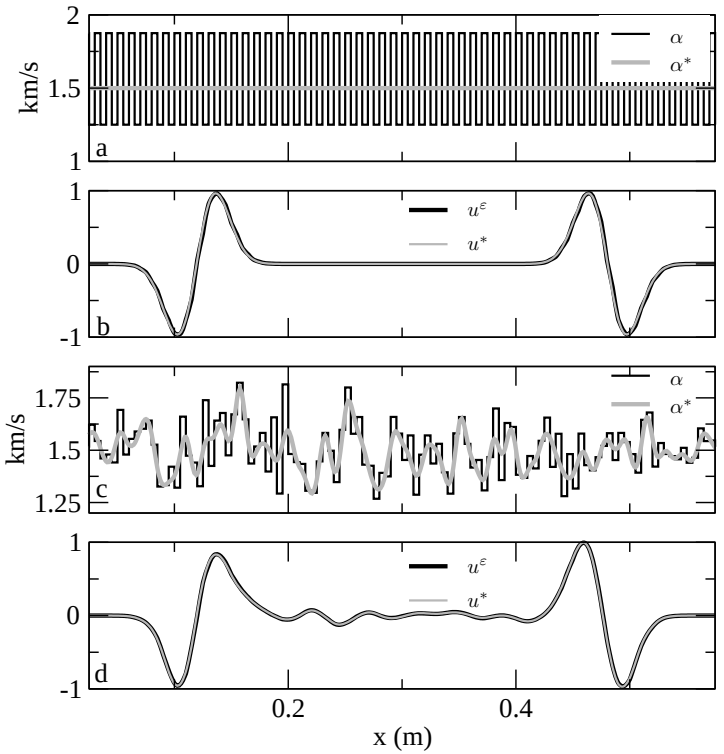

Figure 5: Numerical example used in 3.3.
a: Elastic wave velocities α and α^* in the same periodic model as for Fig. 3 and in the corresponding Backus effective model respectively.
b: Displacement snapshot for $t = 2$ ms computed in the original periodic model (u^ε) and in the corresponding Backus effective model (u^*).
c: Elastic wave velocities in the random model (α) and in the corresponding Backus effective model (α^*) computed for $\varepsilon_0 = 0.5$.
d: Displacement snapshot for $t = 2$ ms computed in the original random model (u^ε) and in the corresponding Backus effective model (u^*).

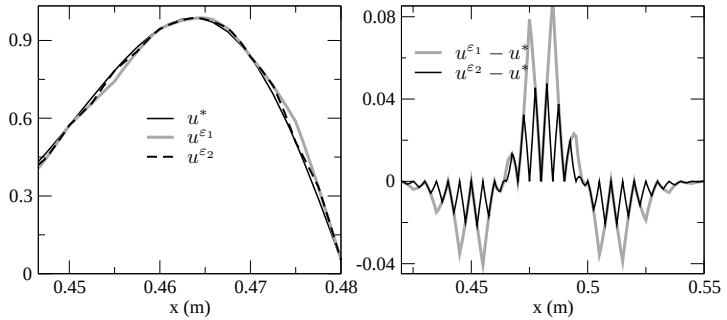

Figure 6: Left: displacement snapshots for $t = 2\,\text{ms}$ computed in the periodic bar for $\varepsilon = \varepsilon_1 = 0.5$ (u^{ε_1}) and $\varepsilon = \varepsilon_2 = 0.25$ (u^{ε_2}) and in the Backus effective model (u^*). Right: residual snapshot $u^\varepsilon - u^*$ for the two ε values.

they look periodic. Translating these observations to an equation, we can write

$$u^\varepsilon(x,t) - u^*(x,t) \simeq \varepsilon r(x, \frac{x}{\varepsilon}, t)\,, \tag{50}$$

where r is a function smooth in x and almost periodic in $\frac{x}{\varepsilon}$.

Let us now observe snapshots of the residual at different times (Fig. 7). It appears that the residual r is a product of two functions, as mentioned previously, and that only the smooth function is propagating and time dependent. Mathematically, this means that

$$r\left(x, \frac{x}{\varepsilon}, t\right) = \chi\left(\frac{x}{\varepsilon}\right) v(x,t)\,, \tag{51}$$

where $\chi\left(\frac{x}{\varepsilon}\right)$ is probably locally periodic and v is a function smooth in space and time dependent. We will see from the theoretical homogenization sections that this observation is confirmed by a mathematical development.

To conclude, even if Backus' results are accurate, visible differences remain between the true and the Backus solutions. These differences argue in favor of the following relation:

$$u^\varepsilon(x,t) \simeq u^*(x,t) + \varepsilon r(x, \frac{x}{\varepsilon}, t)\,, \tag{52}$$

where $r(x,.,t)$ is ℓ-periodic. This could be the first terms of a series expansion such as

$$u^\varepsilon(x,t) = u^0(x, \frac{x}{\varepsilon}, t) + \varepsilon u^1(x, \frac{x}{\varepsilon}, t) + \varepsilon^2 u^2(x, \frac{x}{\varepsilon}, t) + ... \tag{53}$$

This is the starting point of the **two-scale periodic homogenization** that we develop in the next section.

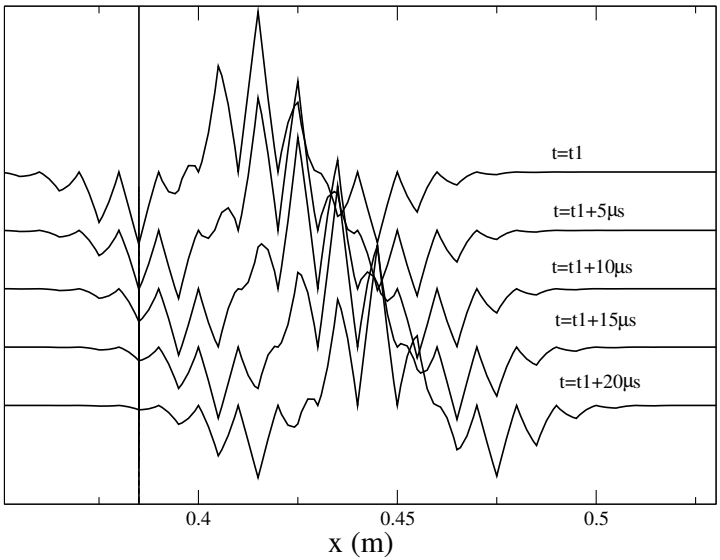

Figure 7: Residual snapshots $u^\varepsilon - u^*$ for $\varepsilon = 0.5$ at five different times. The vertical line at $x = 0.38$ m marks one of the sharp elastic property changes in the bar model.

4 Two-scale homogenization: the 1-D periodic case

In this section, we follow the classical two-scale periodic homogenization technique as, for example, developed by Sanchez-Palencia (1980). Two-scale periodic homogenization technique is based on a mathematical construction that explicitly makes use of two space variables, one for the small scales and one for the large scales. This construction can be puzzling at first: there is of course only one space-variable in nature. The mathematical construction we are about to present could just be an interesting exercise with no connection to the original one space-variable problem. It would not be very useful in the end. Fortunately, a theorem shows that the original one scale problem converges to the two-scale mathematical construction as ε goes to 0. Thanks to this theorem, the results of the two-scale periodic homogenization apply to our original one scale wave propagation problem and make this development useful. The distinction between small and large scales is made simple by the periodicity of the mechanical properties: everything that is periodic, or quasi-periodic, is a small scale and all the rest are large scales.

As one can guess from the examples in the previous sections, the solution to the wave equation in a bar with small periodic heterogeneities depends on two scales: x and $\frac{x}{\varepsilon}$. To explicitly take small-scale heterogeneities into account when solving the wave equation, the small space-variable is introduced (see Fig. 8):

$$y = \frac{x}{\varepsilon}\,, \tag{54}$$

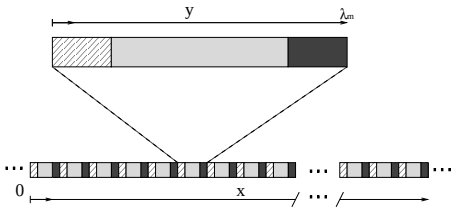

Figure 8: Sketch displaying the x and y variables along a 1-D bar with periodic heterogeneities. y corresponds to a zoom on a single periodic cell.

where $\varepsilon = \frac{\ell}{\lambda_{\text{min}}}$, as defined in (26). In many publications, y is often named the microscopic variable and x the macroscopic variable. In the following, we will also use "fine-scale", "micro-scale" or "small-scale" for y and "large scale" or "macro-scale" for x. When $\varepsilon \to 0$, that is the periodicity is infinitely small compared to λ_{min}, any change in y induces a very small change in x. This leads to the idea of separation of scales: y **and** x **are treated as independent variables**. As already mentioned, there is, of course only one space-variable in the original problem. The introduction of the small scale variable y is a pure mathematical trick that makes sense in the end thanks to the convergence theorem.

The observations made in the previous section suggests that the solution to the wave equation could be sought as an asymptotic power series in ε:

$$\begin{aligned} u^\varepsilon(x,t) &= u^0(x,y,t) + \varepsilon u^1(x,y,t) + \varepsilon^2 u^2(x,y,t) + \dots, \\ \sigma^\varepsilon(x,t) &= \frac{1}{\varepsilon}\sigma^{-1}(x,y,t) + \sigma^0(x,y,t) + \varepsilon\sigma^1(x,y,t) + \dots, \end{aligned} \tag{55}$$

in which coefficients u^i and σ^i depend on both space variables x and y and are λ_{min}-periodic in y (they belong to $\mathcal{T}$, see Sec. 2.2). This ansatz- the x and y dependence of the solution- explicitly incorporates our observations, that the sought solution depends on the wavefield at the large scale, and also on the small variations of elastic properties locally. As we will see it soon, the constitutive relation between the stress and the displacement involves a $1/\varepsilon$. Therefore, if the displacement power series starts at i_0, the stress power series should start at $i_0 - 1$. Starting the displacement series at $i = 0$, as expected, implies to start the stress expansion at $i = -1$.

We now need to build the equations that drive the u^i and σ^i coefficients. The x and y relation (54) implies that partial derivatives with respect to x should become:

$$\frac{\partial}{\partial x} \to \frac{\partial}{\partial x} + \frac{1}{\varepsilon}\frac{\partial}{\partial y}\,. \tag{56}$$

We now introduce ρ and E, the cell mechanical properties:

$$\begin{aligned} \rho(y) &= \rho^\varepsilon(\varepsilon y)\,, \\ E(y) &= E^\varepsilon(\varepsilon y)\,, \end{aligned} \tag{57}$$

E and ρ are the unit cell elastic modulus and density. It is important to note that, with such a definition, ρ and E are λ_{min}-periodic and independent of ε. Indeed, for any function ℓ-periodic h^ε, the function $h(y) = h^\varepsilon(\varepsilon y)$ is λ_{min}-periodic and independent of ε:

$$\begin{aligned} h(y + \lambda_{\text{min}}) &= h^\varepsilon(\varepsilon y + \varepsilon\lambda_{\text{min}})\,, \\ &= h^\varepsilon(\varepsilon y + l)\,, \\ &= h^\varepsilon(\varepsilon y)\,, \\ &= h(y)\,, \end{aligned} \tag{58}$$

where we have use the definition (26) of ε. It shows that h is λ_{min}-periodic whatever the value of ε.

The definitions (57) of the cell properties are important: it implies that all spatial variation of the mechanical properties belong to the small scale domain. This is trivial in the periodic case, nevertheless, in the non-periodic case, this definition will be one of the most difficult but critical points. One of the reasons explaining the simplicity of this definition lies in the outstanding properties of periodic functions: periodic functions remain periodic after most mathematical non-linear manipulations such as taking the product, the square, the square root, or the inverse. For example, it can happen that the cell properties need to be defined (57) on (ρ, α) and not (ρ, E). Nevertheless, due to the periodic nature of the mechanical properties, it does not matter and any other choice than (ρ, E) works. We will see that this simplicity doesn't hold anymore in the non-periodic case.

At this stage, we do not say much about the source f. In the following development, we treat f as a constant term, even if it is obviously not the case, and we postpone the discussion about the source.

Introducing expansions (55) in equations (27-28), using (56) we obtain:

$$\rho\partial_{tt}\sum_{i\geq 0}\varepsilon^i u^i - \left(\partial_x + \frac{1}{\varepsilon}\partial_y\right)\sum_{i\geq -1}\varepsilon^i\sigma^i = f\delta_{i,0} \tag{59}$$

$$\sum_{i\geq -1}\varepsilon^i\sigma^i = E\left(\partial_x + \frac{1}{\varepsilon}\partial_y\right)\sum_{i\geq 0}\varepsilon^i u^i \tag{60}$$

where δ is the Kronecker symbol. It leads to

$$\rho\partial_{tt}\sum_{i\geq 0}\varepsilon^i u^i - \partial_x\sum_{i\geq -1}\varepsilon^i\sigma^i - \partial_y\sum_{i\geq -1}\varepsilon^{i-1}\sigma^i = f\delta_{i,0} \tag{61}$$

$$\sum_{i\geq -1}\varepsilon^i\sigma^i = E\sum_{i\geq 0}\varepsilon^i\partial_x u^i + E\sum_{i\geq 0}\varepsilon^{i-1}\partial_y u^i \tag{62}$$

Renaming $i-1$ as i on the last sums, identifying term by term in ε^i we obtain, $\forall i \geq 0$:

$$\rho\partial_{tt}u^i - \partial_x\sigma^i - \partial_y\sigma^{i+1} = f\delta_{i,0}\,, \tag{63}$$

$$\sigma^i = E(\partial_x u^i + \partial_y u^{i+1})\,, \tag{64}$$

The last equations are the ones that drive the homogenization expansion coefficients. They have to be solved for each i. In this context, for any function $h(x, y)$ λ_{min}-periodic in y, the cell average defined in section 2 is:

$$\langle h \rangle (x) = \frac{1}{\lambda_{\text{min}}} \int_0^{\lambda_{\text{min}}} h(x, y) dy \,. \tag{65}$$

4.1 Resolution of the homogenization problem

We now solve the equation (63) and (64). In the following, the time dependence t is dropped to ease the notations.

4.1.1 Resolution of the homogenized equations, step 1

Equations (63) for $i = -2$ and (64) for $i = -1$ give

$$\begin{aligned} \partial_y \sigma^{-1} &= 0 \,, \\ \sigma^{-1} &= E \partial_y u^0 \,, \end{aligned} \tag{66}$$

which implies

$$\partial_y (E \partial_y u^0) = 0 \,. \tag{67}$$

Multiplying the last equation by u^0, integrating over the unit cell, using integration by parts and taking into account the periodicity of u^0 and $E\partial_y u^0$, we find

$$\int_0^{\lambda_{\text{min}}} (\partial_y u^0)^2 E \, dy = 0 \,. \tag{68}$$

$E(y)$ being a strictly positive function, the unique solution to the above equation is $\partial_y u^0 = 0$. This implies that u^0 doesn't depend on y and we therefore have

$$u^0 = \left\langle u^0 \right\rangle \,, \tag{69}$$

$$\sigma^{-1} = 0 \,. \tag{70}$$

The fact that the order 0 solution in displacement u^0 is independent of the micro scale variable y is an important result, which confirms the observation made in Fig. 4, that the displacement is a smooth function to the leading order.

4.1.2 Resolution of the homogenized equations, step 2

Equations (63) for $i = -1$ and (64) for $i = 0$ give

$$\partial_y \sigma^0 = 0 \,, \tag{71}$$

$$\sigma^0 = E(\partial_y u^1 + \partial_x u^0) \,. \tag{72}$$

Equation (71) implies that $\sigma^0(x,y) = \langle \sigma^0 \rangle (x)$ and, with (72), that

$$\partial_y \left(E \partial_y u^1 \right) = -\partial_y E \, \partial_x u^0 \, . \tag{73}$$

The last equation is a partial differential equation in y. For a fixed x, knowing that u^0 only depends on x, $\partial_x u^0$ is a constant in y. (73) is therefore an equation of type

$$\partial_y (E(y) \partial_y q(y)) = \gamma f(y) \, , \tag{74}$$

where γ is a constant. The last equation is linear with respect to the second member and a general solution takes the form

$$q(y) = \gamma q_0(y) + \beta \tag{75}$$

where q_0 is the solution of (74) for $\gamma = 1$ and a constant β. Applying this observation to (73), we can separate the variables and look for a solution of the form

$$u^1(x,y) = \chi^1(y) \partial_x u^0(x) + \langle u^1 \rangle (x) \tag{76}$$

where $\chi^1(y)$ is called the first order periodic corrector (γ is $\partial_x u^0$ and β is $\langle u^1 \rangle (x)$ in (74) and (75)). To enforce the uniqueness of the solution, we impose $\langle \chi^1 \rangle = 0$. Introducing (76) into (73), we obtain the equation of the so-called cell problem:

$$\partial_y \left[E(1 + \partial_y \chi^1) \right] = 0 \, , \tag{77}$$

χ^1 being λ_{min}-periodic and verifying $\langle \chi^1 \rangle = 0$. Introducing (76) into (72), taking the cell average and using the fact that u^0 and σ^0 do not depend upon y, we find the order 0 constitutive relation,

$$\sigma^0 = E^* \partial_x u^0 \, , \tag{78}$$

where E^* is the order 0 homogenized elastic coefficient,

$$E^* = \left\langle E(1 + \partial_y \chi^1) \right\rangle \, . \tag{79}$$

4.1.3 Resolution of the homogenized equations, step 3

Equations (63) for $i = 0$ and (64) for $i = 1$ give

$$\rho \partial_{tt} u^0 - \partial_x \sigma^0 - \partial_y \sigma^1 = f \, , \tag{80}$$

$$\sigma^1 = E(\partial_y u^2 + \partial_x u^1) \, . \tag{81}$$

Applying the cell average on (80), using the property (3), the fact that u^0 and σ^0 do not depend on y and gathering the result with (78), we find the order 0 wave equation:

$$\begin{aligned} \rho^* \partial_{tt} u^0 - \partial_x \sigma^0 &= f \\ \sigma^0 &= E^* \partial_x u^0 \, , \end{aligned} \tag{82}$$

where

$$\rho^* = \langle \rho \rangle \tag{83}$$

is the effective density and E^* is defined by equation (99). This a remarkable result: the effective wave equation is still a classical wave equation meaning that it can be solved using classical wave equation solvers without any change. Knowing that ρ^* and E^* are constant, solving the wave equation for the order 0 homogenized medium is a much simpler task than solving for the original medium and no numerical difficulty related to the rapid variation of the properties of the bar arises. One of the important results of the homogenization theory is to show that u^ε "converges" towards u^0 when ε tends towards 0 (the so-called convergence theorem, see Sanchez-Palencia (1980) and Sec. 4.2).

Once u^0 is found, the first order correction, $\chi^1(x/\varepsilon)\partial_x u^0(x)$, can be computed. To obtain the complete order 1 solution u^1 using (76), $\left\langle u^1 \right\rangle$ remains to be found. Subtracting (82) from (80) we have,

$$\partial_y \sigma^1 = (\rho - \langle \rho \rangle)\partial_{tt} u^0 \,, \tag{84}$$

which, together with (81) and (76) gives

$$\begin{aligned} \partial_y \left(E \partial_y u^2 \right) &= -\partial_y (E \partial_x u^1) + (\rho - \langle \rho \rangle)\partial_{tt} u^0 \,, & (85) \\ &= -\partial_y E \; \partial_x \left\langle u^1 \right\rangle - \partial_y \left(E \chi^1 \right) \partial_{xx} u^0 + (\rho - \langle \rho \rangle)\partial_{tt} u^0 \,. & (86) \end{aligned}$$

Using the linearity of the last equation we can separate the variables and look for a solution of the form

$$u^2(x,y) = \chi^2(y)\partial_{xx} u^0(x) + \chi^1(y)\partial_x \left\langle u^1 \right\rangle (x) + \chi^\rho(y)\partial_{tt} u^0 + \left\langle u^2 \right\rangle (x) \,, \tag{87}$$

where χ^2 and χ^ρ are solutions of

$$\begin{aligned} &\partial_y \left[E(\chi^1 + \partial_y \chi^2) \right] = 0 \,, & (88) \\ &\partial_y \left[E \partial_y \chi^\rho \right] = \rho - \langle \rho \rangle \;, & (89) \end{aligned}$$

with χ^2 and χ^ρ λ_{min}-periodic and where we impose $\left\langle \chi^2 \right\rangle = \langle \chi^\rho \rangle = 0$ to ensure the uniqueness of the solutions. Introducing (87) into (81) and taking the cell average, we find the order 1 constitutive relation:

$$\left\langle \sigma^1 \right\rangle = E^* \partial_x \left\langle u^1 \right\rangle + E^{1*} \partial_{xx} u^0 + E^{\rho *} \partial_{tt} u^0 \tag{90}$$

with

$$\begin{aligned} E^{1*} &= \left\langle E(\chi^1 + \partial_y \chi^2) \right\rangle & (91) \\ E^{\rho *} &= \langle E \partial_y \chi^\rho \rangle & (92) \end{aligned}$$

The periodicity condition on χ^2 imposes $\partial_y \chi^2 = -\chi^1$ and therefore $E^{1*} = 0$.

Finally using (76) and taking the average of equations (63) for $i = 1$ gives the order 1 wave equation

$$\begin{aligned} \langle\rho\rangle \partial_{tt} \langle u^1 \rangle + \langle \rho\chi^1 \rangle \partial_x \partial_{tt} u^0 - \partial_x \langle \sigma^1 \rangle = 0 \\ \langle \sigma^1 \rangle = E^* \partial_x \langle u^1 \rangle + E^{\rho *} \partial_{tt} u^0 \,. \end{aligned} \tag{93}$$

It can shown (see Capdeville et al. (2010a), appendix A) that $E^{\rho *} = \langle \rho\chi^1 \rangle$ and therefore, renaming $\langle \tilde{\sigma}^1 \rangle = \langle \sigma^1 \rangle - E^{\rho *} \partial_{tt} u^0$, the last equations can be simplified to

$$\begin{aligned} \langle\rho\rangle \partial_{tt} \langle u^1 \rangle - \partial_x \langle \tilde{\sigma}^1 \rangle = 0 \\ \langle \tilde{\sigma}^1 \rangle = E^* \partial_x \langle u^1 \rangle \,. \end{aligned} \tag{94}$$

This is once again a classical wave equation, but with no second member. Knowing that such equations have a unique solution and that knowing that 0 is solution, we conclude that $\langle u^1 \rangle = 0$. Summing u^0 and u^1, and using the fact that $\langle u^1 \rangle = 0$, we obtain the complete order 1 solution:

$$\hat{u}^1(x, y) = u^0(x) + \varepsilon \chi(y) \partial_x u^0(x) \,. \tag{95}$$

We stop the resolution of (63-64) here but it is possible to go up to a higher order (see J. Fish and Nagai (2002) for a 1-D periodic case up to the order 2).

4.1.4 Analytical solution to the cell problem

It is useful to note that a general analytical solution to the cell problem (77) exists and is

$$\chi^1(y) = -y + a \int_0^y \frac{1}{E(y')} dy' + b \,. \tag{96}$$

The periodicity condition imposes

$$a = \left\langle \frac{1}{E} \right\rangle^{-1} , \tag{97}$$

and b can be found using $\langle \chi^1 \rangle = 0$. We therefore have

$$\partial_y \chi^1(y) = -1 + \left\langle \frac{1}{E} \right\rangle^{-1} \frac{1}{E(y)} \tag{98}$$

An interesting follow up to the last equation is that, once introduced in (79), we have

$$E^* = \left\langle \frac{1}{E} \right\rangle^{-1} . \tag{99}$$

This solution for the effective Young modulus is very similar to the Backus solution (44) and both solutions give the same results if applied to the periodic media. There is nevertheless an important difference: the two-scale homogenization solution only applies to periodic media while the Backus solution applies to any media.

4.1.5 Strain leading order

What about strain? The strain can also be expanded as a power series in ε:

$$\epsilon^{\varepsilon}(u^{\varepsilon})(x) = \sum_i \varepsilon^i \epsilon^i \left(x, \frac{x}{\varepsilon}\right) . \tag{100}$$

Using (56) and (55) we have

$$\epsilon^{\varepsilon}(u^{\varepsilon}) = \left(\partial_x + \frac{1}{\varepsilon}\partial_y\right) \sum_i \varepsilon^i u^i \tag{101}$$

and therefore

$$\epsilon^{\varepsilon}(u^{\varepsilon}) = \sum_i \varepsilon^i \left(\partial_x u^i + \partial_y u^{i+1}\right) \tag{102}$$

For the leading order (using $\partial_y u^0(x) = 0$), we have

$$\epsilon^0 = \partial_x u^0 + \partial_y u^1 . \tag{103}$$

Using $\partial_y u^1 = \partial_y \chi^1 \partial_x u^0$, we finally find

$$\epsilon^0(x, y) = \left(1 + \partial_y \chi^1(y)\right) \partial_x u^0(x) . \tag{104}$$

The last equation is interesting: on the contrary to the displacement, the strain depends on y to the leading order. This implies that the strain is not smooth and depends strongly on the small-scale, which has been already observed in Fig. 4. Another example is given in Fig. 9, which shows that the amplitude on the small-scale effect does not change with ε: no matter how small the heterogeneity, if it has a large contrast, it will have a strong effect on strain. This has important consequences for any wavefield gradient measurements such as rotation and strain (see Sec. 6.1.1).

4.1.6 Summary

To summarize, at this stage, we have shown that:

- u^0 and σ^0 do not depend on the small-scale variable y;
- u^0 and σ^0 are solution of effective equations (82) which are the same as the original wave equation, but for the effective coefficients;
- to the order 1, we have

  $$u^{\varepsilon}(x, t) = u^0(x, t) + \varepsilon \chi^1 \left(\frac{x}{\varepsilon}\right) \partial_x u^0(x, t) + O(\varepsilon^2) , \tag{105}$$

  where χ^1 is the first order periodic corrector. ;
- χ^1 is solution of the cell equation (77), a static time independent equation;
- the effective Young modulus E^* is obtained though (79).

It is interesting to note that the equation (105) confirms the numerical observation made in section 3.4, in particular in the Eq. 51.

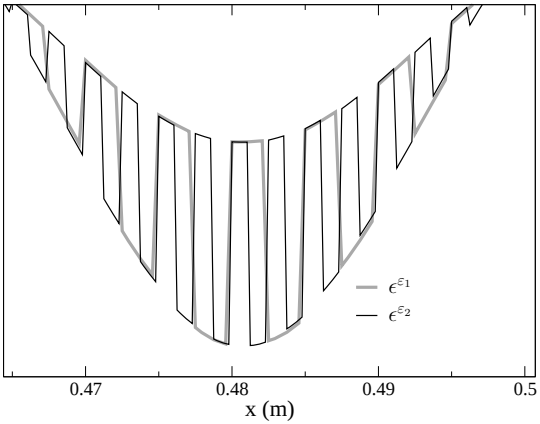

Figure 9: Strain snapshots computed in the same periodic bar as for section 3.1, but for two ε, $\varepsilon_1 = 0.5$, and $\varepsilon_2 = 0.25$. One can notice that if the local periodicity of the strain changes with ε as for the displacement residual, the oscillations' amplitude are independent of ε and does not scale as ε as for the displacement residual.

4.2 Convergence theorem

So far, we have extensively used the ansatz

$$u^\varepsilon(x,t) = u^0\left(x, \frac{x}{\varepsilon}, t\right) + \varepsilon u^1\left(x, \frac{x}{\varepsilon}, t\right) + \varepsilon^2 u^2\left(x, \frac{x}{\varepsilon}, t\right) + ... \tag{106}$$

with $u^i(x,y)$ λ_{min}-periodic for the second variable and the separation of scale (x and y are treated as independent variables) but with no formal proof or justification.

The proof of the homogenization theorem

$$\begin{cases} u^\varepsilon \xrightarrow[\varepsilon\to 0]{} u^0 \text{ weakly in the appropriate space} \\ E^\varepsilon \partial_x u^\varepsilon \xrightarrow[\varepsilon\to 0]{} E^* \partial_x u^0 \text{ weakly in the appropriate space} \end{cases}$$

is an important concern in the homogenization community and has yielded many works. Among them, we can find

- the oscillating test function method (sometimes called the *energy method*) derived by Tartar (Tartar, 1978; Murat & Tartar, 1997). This method does not require the periodicity hypothesis to work. It is also the base of some numerical homogenization methods (Owhadi & Zhang, 2008);
- the two-scale convergence (Nguetseng, 1989; Allaire, 1992), designed for the periodic case. It justifies the scale separation and shows strong convergence when higher order terms of the expansion are used;
- the variational homogenization and the Γ-convergence methods (Giorgi, 1984);

- the convergence issues are also addressed in the general G-convergence and H-convergence theories (Giorgi & Spagnolo, 1973; Murat & Tartar, 1997).

A weak convergence means that the convergence is true on average (integral form), but not for every individual point. For example, the true strain never converges to the order 0 strain, but its average does. Strong convergence (for every individual point) can be obtained if the first order corrector is accounted for (Allaire, 1992).

The convergence theorems justify the ansatz (106) and the explicit scale separation of the two-scale method: as ε becomes smaller and smaller, the true problem converges to the two-scale problem. It implies that the strange two-scale construction makes sense and is useful. Note that, in most standard convergence problems, the approximate solution converges toward the true problem. Here, it is the other way around: we have the solutions to a series of true problems that converge toward the asymptotic solution. In the series of true problems, only one corresponds to the real periodicity of the bar. This has an important consequence: if the periodicity of the real bar corresponds to an ε that is not small, or not small enough, then the effective solution may not be accurate. If it is the case, unfortunately, nothing can be done to improve the solution in the two-scale homogenization framework, besides using a purely numerical solution in the real bar. We will see that it is different for the non-periodic homogenization.

4.3 External point sources

In practice, the external source process often occurs over an area much smaller than the smallest wavelength λ_{min} allowing us to ideally consider it as a point source: $f(x,t) = g(t)\delta(x - x_0)$ or $f(x,t) = g(t)\partial_x\delta(x - x_0)$. There are two ways to deal with a point source or with multiple point sources.

In the first approach, we assume that we are not interested in the near field of the source and we would like to keep the source as a point source. Indeed, forgetting about the near-field, point sources are simple and effective to implement into solvers such as SEM that use the weak form of the wave equation (it is more complex for solvers such as finite differences that use the strong form). Then, two potential issues arise:

1. in the vicinity of x_0, there is no such a thing as a minimum wavelength. The asymptotic development presented here is therefore only valid far away enough from x_0;

2. a point source has a local interaction with the microscopic structure that needs to be accounted for.

The first point is not an issue as we assumed that we are not interested in the near-field. One should nevertheless keep in mind that, very close to x_0, the solution is not accurate, but not less than any standard numerical methods used to solve the wave equation. For example, this is the case for the spectral element method for the

element containing the source and some times for the elements next to it (Nissen-Meyer et al., 2007). The second point is more important and can be addressed in the following way: the hypothetical point source is just a macroscopic representation of a more complex physical process, and what is relevant is to ensure the conservation of the energy released at the source. Therefore we need to find a corrected source f^ε that preserves the energy associated with the original force f up to the desired order (here 1 as an example). We therefore need

$$(u^\varepsilon, f) = \left(u^0, f^\varepsilon\right) + O(\varepsilon^2)\,, \tag{107}$$

where $(\ .\ ,\ .\ )$ is the L^2 inner product, which for any function g and h is:

$$(g, h) = \int_{\mathbb{R}} g(x)h(x)dx\,. \tag{108}$$

Using (105) we have, to the order 1,

$$(u^0, f) + \varepsilon\left(\chi^1\left(y\right)\partial_x u^0(x,t), f\right) = \left(u^0, f^\varepsilon\right) + O(\varepsilon^2)\,, \tag{109}$$

and, using integration by parts, we find

$$f^\varepsilon(x,t) = \left[1 - \varepsilon\chi^1\left(\frac{x}{\varepsilon}\right)\partial_x\right]\delta(x - x_0)g(t)\,. \tag{110}$$

f^ε is the corrected source that needs to be used in the homogenized wave equation (82) instead of f.

If the source term has the form $f(x,t) = g(t)\partial_x\delta(x - x_0)$, which is in the case of earthquake moment tensors, to the leading order,

$$f^\varepsilon(x,t) = \left[1 + \partial_y\chi^1\left(\frac{x}{\varepsilon}\right)\right]\partial_x\delta(x - x_0)g(t)\,. \tag{111}$$

It can be seen from the last equation that no ε appears in front of the corrector, which means source term is strongly modified by the local structure. This leads to significant distortion on the apparent moment tensor in realistic situations and can lead to wrong interpretation of the inverted source tensors (Capdeville et al., 2010b; Burgos et al., 2016).

If we are interested in the near-field, we need a different approach. The second approach implies the two-scale construction of the external source term $f(x,y)$ from the original source term $f(x)$. This can only be done in the non-periodic framework presented in Sec. 5. We will not develop this approach here, it is the subject of publication in preparation. Nevertheless, the near-field can be modeled as another corrector θ, and this corrector appears at the order 0 in the displacement when sources appear as a derivative of a Dirac function, such as for earthquake moment tensors. Therefore, displacement depends on y at the zero order in the vicinity of the source, which is very unusual in homogenization, but consistent with both numerical and real observations. Similarly, an effective source appears, which is not a point source anymore, but a volumetric force map instead.

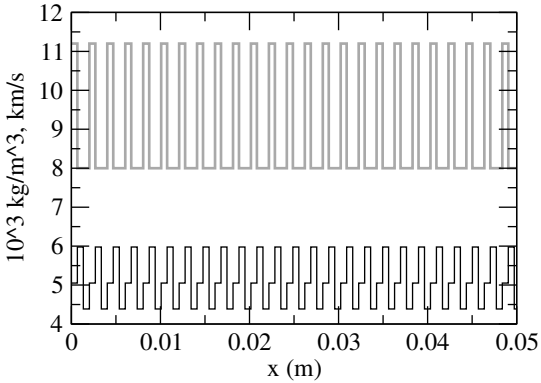

Figure 10: A 5 cm sample of the density in 10^3 kg m^{-3} (gray) and velocity in km s^{-1} (black) for the bar.

4.4 An example

A numerical experiment in a bar of periodic properties shown in Fig. 10 is performed. The periodicity of the structure is l =6 mm. First, the cell problem (77) is solved with periodic boundary conditions using a finite element method based on the same mesh and quadrature like the one that will be used to solve the wave equation. Although this is not necessary for this simple 1-D case (we could use the analytical solution), it is a convenient solution and makes it simple to access E^*, the correctors χ and well as the external source term f^ε. Then, the homogenized wave equation,

$$\rho^* \partial_{tt} u - \partial_x \left(E^* \partial_x u \right) = f \,, \tag{112}$$

where $u = u^0$ and $f = f^\varepsilon$, is solved using the SEM (see Capdeville (2000) or Igel (2017) for a complete description of the 1-D SEM).

The point source is located at $x = 2$ m. The time wavelet $g(t)$ is a Ricker with a central frequency of 50 kHz (which gives a corner frequency of about 125 kHz) and a central time shift t_0 =6.4 10^{-5} s. In the far-field, this wavelet gives a minimum wavelength of about 4 cm which corresponds to a wave propagation with $\varepsilon = 0.15$. In practice, the bar is of course not infinite, but its length (5 m) and the time at which the displacement is recorded (4.9 10^{-4} s) is such that the wave pulse does not reach the extremity of the bar. To be accurate, the reference solution is computed with a SEM mesh matching all interfaces with an element boundary (7440 elements for the 5 m bar). To make sure that only the effect of homogenization is seen in the simulations, the mesh and time step used to compute the reference solution are also used to compute the homogenized solution. Once the simulation is done for the time step corresponding to t =4.9 10^{-4} s, the complete order 1 solution can be computed with (95). We can also compute the incomplete homogenized solution at the order 2 as shown in Capdeville et al. (2010b).

The results of the simulation are shown in Fig. 11. On the upper left plot (Fig. 11a)

the reference solution (bold red line), the order 0 solution (black line) and a solution obtained in the bar with a $E^* = \langle E^\varepsilon \rangle$ ("E average", dashed line) for t =4.9 10^{-4} s are shown as a function of x. As expected, the "E average" solution is not in phase with the reference solution and shows that this "natural" filtering is not accurate. On the other hand, the order 0 homogenized solution is already in excellent agreement with the reference solution. On Fig. 11b the residual between the order 0 homogenized solution and the reference solution $u^0 - u^\varepsilon$ is shown. The error amplitude reaches 2% and contains fine-scale variations. In Fig. 11c the order 1 residual $\hat{u}^1 - u^\varepsilon$ (bold red line) and the partial order 2 residual $\hat{u}^2(x,t) - u^\varepsilon(x,t)$ (see Capdeville et al., 2010a for the order 2 calculus), where $\hat{u}^i$ are the sum of homogenized terms from 0 to i is shown. Comparing Fig. 11b and Fig. 11c, it can be seen that the order 1 periodic corrector removes most of the fine-scale variations present in the order 0 residual. The remaining variations disappear with the partial order 2 residual. The remnant smooth residual is due to the $\langle u^2 \rangle$ that has not computed. In order to check that it is indeed an ε^2 residual, the residual computed for $\varepsilon = 0.15$ is overlapped with a residual computed for $\varepsilon = 0.075$ (which corresponds to l_0=3 mm) and the amplitude is multiplied by a factor 4. The fact that these two signals overlap is consistent with a ε^2 residual.

5 Two-scale homogenization: the 1-D non-periodic case

We now treat the non-periodic case. In the periodic case, we were able to define a series of ε indexed problems by varying the periodicity. Here, this is not possible anymore as the mechanical properties $(\rho(x), E(x))$ can contain all possible scales with no restriction. No ε can be defined simply and here we do not use the superscript ε for the mechanical properties and solution of the wave equation. The wave equations are

$$\begin{aligned} \rho \partial_{tt} u - \partial_x \sigma &= f \,, \\ \sigma &= E \partial_x u \,. \end{aligned} \tag{113}$$

We assume that the source time function has a maximum frequency f_{max} and the a minimum wavelength λ_{min} exists. The solution u, σ to the wave equations implicitly depend upon f_{max}.

5.1 The Backus solution

As shown in Fig. 5c and Fig. 5d, the Backus solution (47) can be applied to non-periodic settings and provide an accurate order 0 solution, at least in 1-D and for layered media. If we take a closer look at the difference between the reference solution and the Backus solution shown in Fig. 12, it can be seen that, similar to the periodic case, the residual is not zero and contains small scale oscillations. The Backus solution does not explain this difference.

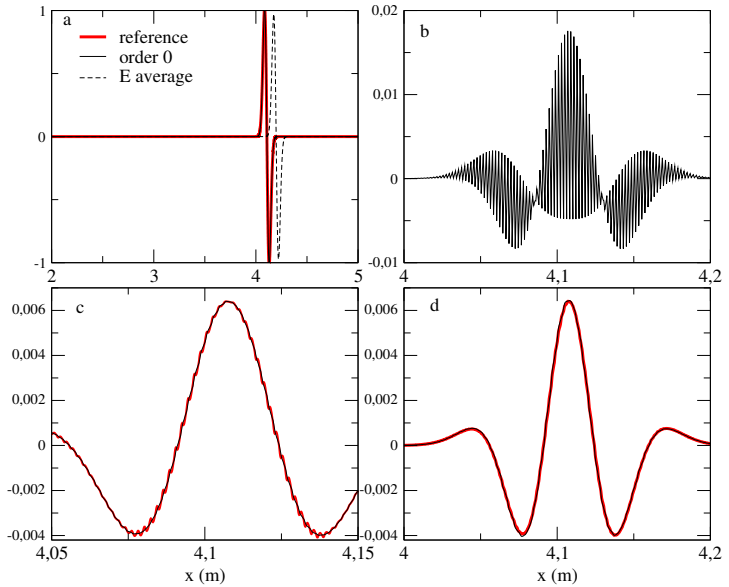

Figure 11: Results of the numerical example in section 4.4.
a: displacement $u^\varepsilon(x,t)$ at t =4.9 10^{-3} s computed in the reference model shown in Fig. 10 (red), the order 0 homogenized solution $\hat{u}^0(x,t)$ (black) and the solution computed in a model obtained by averaging the elastic properties ($\langle\rho^\varepsilon\rangle$ and $\langle E^\varepsilon\rangle$) (dashed).
b: order 0 residual ($u^0 - u^\varepsilon$).
c: order 1 residual ($u^0 + \varepsilon u^1 - u^\varepsilon$) (red) and partial order 2 residual ($u^0 + \varepsilon u^1 + \varepsilon^2 u^2 - u^\varepsilon(x,t)$) (black).
d: partial order 2 residual for $\varepsilon = 0.15$ (red) and partial order 2 residual for $\varepsilon = 0.075$ with amplitude multiplied by 4 (black).

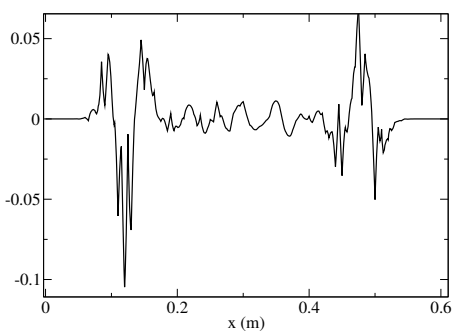

Figure 12: Displacement residual ($u^\varepsilon - u^*$) snapshot at $t = 2$ ms in the same random model as for Fig. 5, where u^* is obtained in the Backus effective medium. The residual is normalized by the maximum amplitude of the reference solution.

5.2 Naive solutions to the two-scale homogenization periodicity limitation

At this stage, we have two different approaches to deal with small scales: the Backus approach and the two-scale homogenization method. On the one hand, the Backus method applies to both periodic and non-periodic heterogeneities and it gives an accurate effective solution. However, as seen above, it does not go beyond the leading order of the effective solution and it does not explain the small oscillations around it (or large oscillations for strain) and it does not propose a solution for the source. Furthermore, it cannot be extended to higher dimensional 2-D or 3-D cases. On the other hand, the two-scale homogenization method is a complete theory that gives solutions for leading order effective solution, corrector, strain, and external sources. Moreover, as we will see in section 6, it extends naturally to dimensions higher than 1-D. However, it only applies to media with periodic heterogeneities, which is an unacceptable limitation for geological media.

It is tempting to directly apply the two-scale periodic method to non-periodic media. But, to do so, what should the periodic cell be? It could be the entire bar. In that case, the effective media is constant all along the bar, with $\rho^* = \frac{1}{L}\int_0^L \rho(x)dx$ and $\frac{1}{E^*} = \frac{1}{L}\int_0^L \frac{1}{E}(x)dx$. In a homogeneous bar, a coda wave after the ballistic wave cannot appear, but we know from Fig. 5d that coda wave is present. Therefore, this solution does not work. Another option is to use a moving window of a size comparable to the wavelength and perform many homogenizations along the bar. Unfortunately, in that case, the cell window acts as a convolution with a boxcar function. In such a case, zero order discontinuities (jump) are transformed into first order discontinuities (kink). The latter are as difficult to mesh as the zero order discontinuities and thus, no gain is obtained.

Another tempting idea is to mix the two methods naively. It is interesting that the filters in the two methods are different. The two scale homogenization uses a cell average (65) whereas the Backus solution use a low-pass filter average (6). Why not just replacing the cell average in the two-scale homogenization development (65) by the Backus low-pass filter average (6)? This would work for the effective density ρ^*, from (39) to (83). Nevertheless, for the effective Young modulus, starting from (96) and applying the periodic condition $\chi^1(0) = \chi^1(\lambda_{\text{min}})$, we have

$$0 + b + 0 = -\lambda_{\text{min}} + a\int_0^{\lambda_{\text{min}}} \frac{1}{E(y')}dy' + b\,, \tag{114}$$

which leads to

$$a = \lambda_{\text{min}}\left(\int_0^{\lambda_{\text{min}}} \frac{1}{E(y')}dy\right)^{-1}, \tag{115}$$

$$= \left\langle \frac{1}{E} \right\rangle^{-1}. \tag{116}$$

We therefore see that (99) remains unchanged. Changing $\langle . \rangle$ by $\mathcal{F}^{\varepsilon_0}$ in (79) leads to

$$E^* = \mathcal{F}^{\varepsilon_0}\left(E(1+\partial_y \chi^1)\right) , \tag{117}$$

which, using (98) implies

$$E^* = \mathcal{F}^{\varepsilon_0}(a) . \tag{118}$$

a is constant and therefore $\mathcal{F}^{\varepsilon_0}(a) = a$ and we fall back on

$$E^* = \left\langle \frac{1}{E} \right\rangle^{-1} . \tag{119}$$

There is no way to avoid this result and we fail to replace $\langle . \rangle$ by $\mathcal{F}^{\varepsilon_0}$ in the last equation. This naive approach is clearly not a solution and we propose a more successful solution in the next section.

5.3 New functional spaces

We want to keep the theoretical results obtained from the two-scale periodic homogenization method while preserving the flexibility of the Backus solution. After a few attempts, we knew there is no trivial way to mix those two methods. Therefore, we need to set up a good theoretical framework to achieve our objective.

We first need to define the functional space to which our solutions should belong. In the periodic case, each two-scale expansion coefficients $(u^i(x,y), \sigma^i(x,y)$ ...) belongs to $\mathcal{T}$, the space of two-scale functions λ_{min}-periodic for the second variable (see Sec. 2.2). For the classical periodic homogenization, the periodicity makes it possible to simply and efficiently define the fine-scales. Moreover, as already mentioned, $\mathcal{T}$ has some very interesting properties: one of them is that the product of two functions $(g,h) \in \mathcal{T}^2$ also belongs to $\mathcal{T}$. Actually, a function h in $\mathcal{T}$ still belongs to $\mathcal{T}$ after a non-linear operation, such as taking its inverse. These unusual properties make the periodic homogenization very special: it warranties that fine scales remain in the fine-scale domain through mathematical manipulations and make sure scales are separated. Unfortunately, it is not possible to keep these properties in the non-periodic case.

For the non-periodic case, we now need to define a new functional space $\mathcal{V}$ that would be the equivalent of $\mathcal{T}$ for the periodic case. The idea is to define a two-scale functional space such that only fine-scale variations exist on the y variable in the Fourier sense. To do so, we use $\mathcal{F}$, the spatial filter on the y variable, defined in (10). It is the same as the $\mathcal{F}^{\varepsilon_0}$ filter defined earlier, but it applies to y instead of x. Let λ_0 be the user-defined spatial wavelength scale separation and $k_0 = \lambda_0^{-1}$ the spatial frequency separation. λ_0 is always defined in the large scale domain (the x domain) because it is the physical domain. In the y domain, because of the relation $y = x/\varepsilon_0$, the separation of scale is always λ_{min}. So, in the x domain, any spatial oscillation smaller than λ_0 is considered as small scale. In the spectral domain, for a function h, any value of $\bar{h}(k)$ for $|k| > k_0$ is considered as a small scale. Practically, for a given

function $h(x)$, in order to tell if it has small scale variations, we need to compute its Fourier transform (4) and check if $\bar{h}(k)$ has non zero values for $|k| > k_0$. Even so, we can guess it makes sense to choose λ_0 smaller than λ_{min}, λ_0 is defined by the user, and therefore, the ratio ε_0 (5) is user-defined.

Based on this definition of small scales, we can define a function space of two-scale functions that only contain fine-scale on the second variable:

$$\mathcal{V} = \{h(x,y), Y - \text{periodic in } y \text{ such that } \mathcal{F}(h)(x,y) = \langle h \rangle (x)\} \ . \tag{120}$$

In this definition, for the sake of simplicity, we have omitted to define precisely Y. Y is a segment in y, centered on x/ε_0 and it has to be wide enough to fit the filter wavelet w_m support. A precise definition can be found in Capdeville et al. (2010a). Graphic examples of a function h not in $\mathcal{V}$ and one in $\mathcal{V}$ are given in Fig. 13.

To try to visualize the concept of functions in $\mathcal{V}$ more, let us assume we need to build a two-scale function $g(x,y)$ in $\mathcal{V}$ from a function $h(x)$ with the constrain $h(x) = g(x, \frac{x}{\varepsilon_0})$. For example, h could be the function plotted in Fig. 13a. The periodic solution $g(y) = h(\varepsilon_0 y)$ would not work because in such a case $\mathcal{F}(g)(y)$ would not be constant (smooth variations would still be present). Instead, for any $(x,y) \in \partial\Omega \times Y$, we define

$$g(x,y) = \mathcal{F}^{\varepsilon_0}(h)(x) + (1 - \mathcal{F}^{\varepsilon_0})(h)(\varepsilon_0 y) \, . \tag{121}$$

Obviously, setting $y = x/\varepsilon_0$ in the last equation leads to $g(x, \frac{x}{\varepsilon_0}) = h(x)$. Moreover, one can check that $\mathcal{F}(g) = \langle g \rangle = \mathcal{F}^{\varepsilon_0}(h)(x)$. Indeed, assuming that $\mathcal{F}^{\varepsilon_0} \circ \mathcal{F}^{\varepsilon_0} = \mathcal{F}^{\varepsilon_0}$ (which is only an approximation because of the apodization of w_{ε_0}), we have

$$\begin{aligned}
\mathcal{F}\left((1 - \mathcal{F}^{\varepsilon_0})(h)(\varepsilon_0 y)\right) &= \mathcal{F}^{\varepsilon_0}\left((1 - \mathcal{F}^{\varepsilon_0})(h)(x)\right) \, , && (122)\\
&= (\mathcal{F}^{\varepsilon_0} - \mathcal{F}^{\varepsilon_0} \circ \mathcal{F}^{\varepsilon_0})(h)(x)) \, , && (123)\\
&= (\mathcal{F}^{\varepsilon_0} - \mathcal{F}^{\varepsilon_0})(h)(x)) \, , && (124)\\
&= 0 \, , && (125)
\end{aligned}$$

where, for (122), we have proceeded in a similar way to (12-15). Therefore, g is indeed in $\mathcal{V}$. We will see more of these type of constructions later on.

To summarize,

- in the periodic case, $(u^i, \sigma^i) \in \mathcal{T}^2$, i.e. the expansion coefficients are λ_{min}-periodic in y;
- in the non-periodic case, $(u^{\varepsilon_0,i}, \sigma^{\varepsilon_0,i}) \in \mathcal{V}^2$, i.e. the expansion coefficients contain only fine-scale in the Fourier sense.

Note that, in the non-periodic case, the expansion coefficients implicitly depend on ε_0, whereas in the periodic case, they do not depend upon ε.

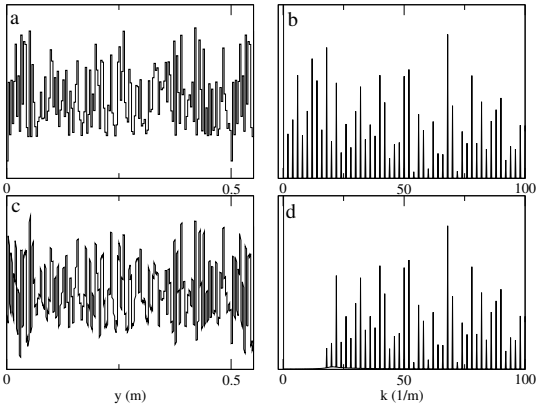

Figure 13: Example of a function $h(x, y)$ not in $\mathcal{V}$ (graph a) and $h(x, y) \in \mathcal{V}$ (graph c) for a $k_0 = 16m^{-1}$ plotted for a given x as a function of y and their respective power spectra (graphs b and d) for positive wavenumber (k). It can be seen that, for $h(x, y) \in \mathcal{V}$ the power spectrum is 0 is the range $]0m^{-1}, 16m^{-1}]$. Both functions are periodic with a periodicity of $0.5m$

5.4 Cell properties in the non-periodic case

We need a similar version of the cell properties (57) to move on. In the periodic case, the construction of cell properties is trivial thanks to the amazing properties of periodic functions mentioned earlier (non-linear manipulation of periodic functions are periodic functions). In the non-periodic case, this construction is not trivial. It is actually the main difficulty of the non-periodic case. We need to find two scales cell properties $\rho^{\varepsilon_0}(x, y), E^{\varepsilon_0}(x, y)$ such that

$$\begin{aligned} \rho(x) &= \rho^{\varepsilon_0}(x, \frac{x}{\varepsilon_0}) \,, \\ E(x) &= E^{\varepsilon_0}(x, \frac{x}{\varepsilon_0}) \,, \end{aligned} \tag{126}$$

and such that the expansion coefficients

$$(u^{\varepsilon_0,i}, \sigma^{\varepsilon_0,i}) \in \mathcal{V}^2 \,. \tag{127}$$

The idea is to assume it is possible to find cell properties such that (126-127) are fulfilled, solve the asymptotic equations and find the necessary condition on $(\rho^{\varepsilon_0}, E^{\varepsilon_0})$ so that a solution exists and then construct them.

5.5 Non-periodic homogenized equations and resolution

The solution to the wave equations (113) is again sought as an asymptotic expansion in ε_0, but this time we look for $u^{\varepsilon_0,i}$ and $\sigma^{\varepsilon_0,i}$ in $\mathcal{V}$:

$$\begin{aligned} u(x,t) &= \sum_{i=0}^{\infty} \varepsilon_0^i u^{\varepsilon_0,i}(x, x/\varepsilon_0, t)\,, \\ \sigma(x,t) &= \sum_{i=-1}^{\infty} \varepsilon_0^i \sigma^{\varepsilon_0,i}(x, x/\varepsilon_0, t)\,. \end{aligned} \tag{128}$$

Note that imposing $u^{\varepsilon_0,i}$ and $\sigma^{\varepsilon_0,i}$ in $\mathcal{V}$ is a strong condition that means that only large scale variations must appear in x and only fine-scale variations in y. One can notice that, in the above equations, the left terms do not depend on ε_0 but the right terms do. For the periodic case, in (55), this is the opposite. Actually, for a consistent mathematical development in the non-periodic case, two epsilons are necessary, ε_0 and ε. If we do so, the ε dependency appears the same way in (128) like in (55). Nevertheless, the role of ε is in that case purely formal and we skip this difficulty here. The complete development can be found in Capdeville et al. (2010a, 2010b); Guillot et al. (2010).

In the following, we work at ε_0 fixed and to simplify the notation further, we drop the explicit ε_0 dependency of u^i and σ^i.

In the non-periodic case, the equations for the two-scale expansion remain unchanged :

$$\rho^{\varepsilon_0}(x,y)\partial_{tt}u^i(x,y) - \partial_x\sigma^i(x,y) - \partial_y\sigma^{i+1}(x,y) = f(x)\delta_{i,0}\,, \tag{129}$$

$$\sigma^i(x,y) = E^{\varepsilon_0}(x,y)(\partial_x u^i(x,y) + \partial_y u^{i+1}(x,y))\,. \tag{130}$$

The only difference from the periodic case is that ρ^{ε_0} and E^{ε_0} depend on ε_0 and both on (x,y) while they depend only on y in the periodic case. To solve these equations, we follow the same procedure as for the periodic case. Because the y periodicity is kept in $\mathcal{V}$, the resolution of the homogenized equations is almost the same as in the periodic case.

- As for the periodic case, equations (129) for $i = -2$ and (130) for $i = -1$ gives $\sigma^{-1} = 0$ and $u^0 = \langle u^0 \rangle$.
- Equations (129) for $i = -1$ and (130) for $i = 0$ implies $\sigma^0 = \langle \sigma^0 \rangle$ and

$$\partial_y \left(E^{\varepsilon_0} \partial_y u^1 \right) = -\partial_y E^{\varepsilon_0}\, \partial_x u^0\,. \tag{131}$$

Using the linearity of the last equation we can separate the variables and look for a solution of the form

$$u^1(x,y) = \chi^{\varepsilon_0}(x,y)\partial_x u^0(x) + \langle u^1 \rangle (x)\,. \tag{132}$$

As $u^1 \in \mathcal{V}$ and $u^0 = \langle u^0 \rangle$, χ^{ε_0} must lie in $\mathcal{V}$ and satisfies

$$\partial_y \left[E^{\varepsilon_0}(1 + \partial_y \chi^{\varepsilon_0}) \right] = 0\,, \tag{133}$$

with periodic boundary conditions. We impose $\langle \chi^{\varepsilon_0} \rangle (x) = 0$. A solution in $\mathcal{V}$ to the last equation exists only if E^{ε_0} has been correctly built, i.e using the general solution (96), $1/E^{\varepsilon_0}$ must lie in $\mathcal{V}$. If this condition is met, $\chi^{\varepsilon_0}(x, y)$ is in $\mathcal{V}$ and

$$\partial_y \chi^{\varepsilon_0}(x, y) = -1 + \left\langle \frac{1}{E^{\varepsilon_0}} \right\rangle^{-1} (x) \ \frac{1}{E^{\varepsilon_0}(x, y)} \,. \tag{134}$$

As for the periodic case, we find the order 0 constitutive relation

$$\sigma^0(x) = E^{*,\varepsilon_0}(x) \partial_x u^0(x) \,, \tag{135}$$

with

$$E^{*,\varepsilon_0}(x) = \langle E^{\varepsilon_0}(1 + \partial_y \chi^{\varepsilon_0}) \rangle (x) \,, \tag{136}$$

$$= \left\langle \frac{1}{E^{\varepsilon_0}} \right\rangle^{-1} (x) \,. \tag{137}$$

- Eqs. (129) for $i = 0$ and (130) for $i = 1$ give

$$\rho^{\varepsilon_0} \partial_{tt} u^0 - \partial_x \sigma^0 - \partial_y \sigma^1 = f \,, \tag{138}$$

$$\sigma^1 = E^{\varepsilon_0}(\partial_y u^2 + \partial_x u^1) \,. \tag{139}$$

From (138) we see that the equation that drives σ^1 has the form

$$\partial_y \sigma^1(x, y) = a(x) \rho^{\varepsilon_0}(x, y) + b(x) \,, \tag{140}$$

where $a(x)$ and $b(x)$ are constants as a function of y. Therefore, to obtain σ^1 in $\mathcal{V}$, (138) implies that ρ^{ε_0} must lie in $\mathcal{V}$. Taking the average of (138) together with (135) leads to the order 0 wave equation:

$$\rho^{*,\varepsilon_0} \partial_{tt} u^0 - \partial_x \sigma^0 = f \tag{141}$$

$$\sigma^0 = E^{*,\varepsilon_0} \partial_x u^0 \,, \tag{142}$$

where $\rho^{*,\varepsilon_0} = \langle \rho^{\varepsilon_0} \rangle$.

We stop the development here, but we could compute order 2 correctors similarly to the periodic case. This is done in Capdeville et al. (2010a). Nevertheless, it is found that, in general, some of the order 2 correctors do not belong to $\mathcal{V}$, which implies there is no general non-periodic solution beyond the order 1, at least in this form. In practice, this is not a strong limitation as only the leading and first order are necessary for most applications. And we will see in the example that the order 2 corrector can still be computed, ignoring the theoretical limitation, and good results can be obtained, at least in that example.

To summarize, we have seen that the non-periodic homogenization is very similar to the periodic case. The main difference is that the effective properties $(\rho^{*,\varepsilon_0}, E^{*,\varepsilon_0})$ depend on the position x, and the corrector χ^{ε_0} depends on both x and y. We have also found the necessary conditions so that a solution in $\mathcal{V}$ is possible. Constructing the cell properties such that these conditions are fulfilled is the purpose of the next section.

5.6 Construction of the cell properties E^{ε_0} and ρ^{ε_0}

Here, we present two ways of building $E^{\varepsilon_0}(x,y)$ and $\rho^{\varepsilon_0}(x,y)$ in $\mathcal{T}$ with the following constraints obtained in the previous sections:

1. ρ^{ε_0} and χ^{ε_0} must lie in $\mathcal{V}$ (see equations (134) and (140));
2. ρ^{ε_0} and E^{ε_0} must be positive functions;
3. $\rho^{\varepsilon_0}(x,x/\varepsilon_0)=\rho(x)$ and $E^{\varepsilon_0}(x,x/\varepsilon_0)=E(x)$.

The first constraint is necessary to obtain solutions in $\mathcal{V}$, at least up to the order 1.

5.6.1 Direct construction

Let us start with the simplest: the cell density property. The condition is that ρ^{ε_0} must be in $\mathcal{V}$. We propose the following construction, for a given x and any $y \in Y_x$:

$$\rho^{\varepsilon_0}(x,y) = \mathcal{F}^{\varepsilon_0}(\rho)(x) + (\rho - \mathcal{F}^{\varepsilon_0}(\rho))(\varepsilon_0 y), \tag{143}$$

and then extended to $\mathbb{R}$ in y by periodicity. Thanks to the fact that, for any h

$$\mathcal{F}^{\varepsilon_0}(\mathcal{F}^{\varepsilon_0}(h)) = \mathcal{F}^{\varepsilon_0}(h), \tag{144}$$

we have

$$\begin{aligned}\mathcal{F}^{\varepsilon_0}((\rho - \mathcal{F}^{\varepsilon_0}(\rho))) &= \mathcal{F}^{\varepsilon_0}(\rho) - \mathcal{F}^{\varepsilon_0}(\rho)\\ &= 0.\end{aligned} \tag{145}$$

$\mathcal{F}^{\varepsilon_0}(\rho^{\varepsilon_0})$ is therefore a constant in y: it contains only fine-scale variations on y, which is the necessary condition to belong to $\mathcal{V}$. It can be easily checked that the condition (3) is met by construction. Finally, it is always possible to find a filter wavelet w such that ρ^{ε_0} is positive. Note that the property (144) is not completely true in practice because the filter w does not have a sharp cutoff, which implies that (144) is not fully accurate. We consider this side effect as being negligible.

For the elastic parameter, it is in general more difficult. Nevertheless, the 1-D case is interesting because it gives an explicit formula to obtain χ^{ε_0} in $\mathcal{V}$. It implies that $1/E^{\varepsilon_0}$ should be in $\mathcal{V}$ (constraint (1)) so that a solution to the non-periodic homogenized problem exists (see Eq. 134). Thanks to this explicit constraint, similar to the density construction, we can propose, for a given x and any $y \in Y_x$,

$$E^{\varepsilon_0}(x,y) = \left[\mathcal{F}^{\varepsilon_0}\left(\frac{1}{E}\right)(x) + \left(\frac{1}{E} - \mathcal{F}^{\varepsilon_0}\left(\frac{1}{E}\right)\right)(\varepsilon_0 y)\right]^{-1}, \tag{146}$$

and then extended to $\mathbb{R}$ in y by periodicity. Similar to the density case, it can easily be checked than $1/E^{\varepsilon_0}$ is in $\mathcal{V}$. This is only true for $1/E^{\varepsilon_0}$ and, for example, E^{ε_0} is not in $\mathcal{V}$.

One can check that $\rho^{\varepsilon_0}(x,x/\varepsilon_0)=\rho(x)$ and $E^{\varepsilon_0}=E(x,x/\varepsilon_0)$ such that the constraint number 3 is fulfilled.

For most standard applications, ρ^{ε_0} and E^{ε_0} are positive functions for any filter wavelet w. Nevertheless, for some extreme cases (e.g. a single discontinuity with several orders of magnitude of elastic modulus contrast), some filter wavelet w designs could lead to a negative E^{ε_0}. In such an extreme case, one should make sure that the design of w allows ρ^{ε_0} and E^{ε_0} to be positive functions.

Finally, we can check that

$$\frac{1}{E^{*,\varepsilon_0}} = \left\langle \frac{1}{E^{\varepsilon_0}} \right\rangle = \mathcal{F}^{\varepsilon_0}\left(\frac{1}{E}\right)(x)\,, \tag{147}$$

which is the Backus solution obtained in section 3.3. We also have

$$\rho^{*,\varepsilon_0} = \mathcal{F}^{\varepsilon_0}(\rho)(x) \tag{148}$$

5.6.2 Implicit construction

For dimensions higher than 1-D, a cell problem, similar to (133), arises (see, for example Sanchez-Palencia, 1980). Unfortunately, there is no explicit solution to this cell problem that leads to an analytical solution equivalent to (134) (there is one for layered media, but it can be considered as a 1-D case). The direct solution explained above to build E^{ε_0} is therefore not available for higher dimensions (it still is for ρ^{ε_0}). Here, we propose a procedure that gives a similar result to the explicit construction without the knowledge that the construction should be done on $1/E$. The main interest of the procedure is that it can be generalized to higher space dimensions. It is based on the work of Papanicolaou and Varadhan (1979) on the homogenization for random media. They suggest working with the gradients of corrector rather than the corrector directly. If we call

$$G^{\varepsilon_0} = \partial_y \chi^{\varepsilon_0} + 1\,, \tag{149}$$

$$H^{\varepsilon_0}(x,y) = E^{\varepsilon_0}(x,y) G^{\varepsilon_0}(x,y)\,, \tag{150}$$

a solution to our problem in $\mathcal{V}$ up to the order 1 can be found if we can build $E^{\varepsilon_0}(x,y)$ such that $(H^{\varepsilon_0}, G^{\varepsilon_0}) \in \mathcal{V}^2$ and $\langle G^{\varepsilon_0} \rangle = 1$. To do so, we propose the following procedure:

1. build a start $E_s^{\varepsilon_0}$ defined as, for a given x and for any $y \in Y_x$, $E_s^{\varepsilon_0}(x,y) = E(\varepsilon_0 y)$ and then extended to $\mathbb{R}$ in y by periodicity ($E_s^{\varepsilon_0}$ is therefore in $\mathcal{T}$). Y_x is a $\mathbb{R}$ segment centered on x/ε_0, at least large enough to contain the support of w_1. Then solve (133) with periodic boundary conditions on Y_x to find $\chi_s^{\varepsilon_0}(x,y)$.
2. Compute $G_s^{\varepsilon_0} = \partial_y \chi_s^{\varepsilon_0} + 1$, then $H_s^{\varepsilon_0}(x,y) = E_s^{\varepsilon_0}(x,y) G_s^{\varepsilon_0}(x,y)$ and finally

$$\begin{aligned} G^{\varepsilon_0}(x,y) &= \frac{1}{\mathcal{F}\left(G_s^{\varepsilon_0}\right)(x, x/\varepsilon_0)} \left(G_s^{\varepsilon_0} - \mathcal{F}\left(G_s^{\varepsilon_0}\right)\right)(x,y) + 1\,, \\ H^{\varepsilon_0}(x,y) &= \frac{1}{\mathcal{F}\left(G_s^{\varepsilon_0}\right)(x, x/\varepsilon_0)} \left[\left(H_s^{\varepsilon_0} - \mathcal{F}\left(H_s^{\varepsilon_0}\right)\right)(x,y) \right. \\ &\qquad \left. + \mathcal{F}\left(H_s^{\varepsilon_0}\right)(x, x/\varepsilon_0)\right]\,. \end{aligned} \tag{151}$$

At this stage, we have, by construction, $(H^{\varepsilon_0}, G^{\varepsilon_0}) \in \mathcal{V}^2$ and $\langle G^{\varepsilon_0} \rangle = 1$.

3. From (150) and (136), we have

$$E^{\varepsilon_0}(x,y) = \frac{H_s^{\varepsilon_0}}{G_s^{\varepsilon_0}}(x,y)\,, \tag{152}$$

$$E^{*,\varepsilon_0}(x) = \langle H^{\varepsilon_0} \rangle (x) = \frac{\mathcal{F}\left(H_s^{\varepsilon_0}\right)}{\mathcal{F}\left(G_s^{\varepsilon_0}\right)}(x, x/\varepsilon_0)\,. \tag{153}$$

4. Once $E^{\varepsilon_0}(x,y)$ is known, following the homogenization procedure to find the different correctors can be pursued.

Once again, we insist on the fact that the main interest of this procedure is that obtaining an explicit solution to the cell problem is not required and it can be extended to 2-D or 3-D.

Remarks:

- in practical cases, the bar is finite and Y_x can be chosen to enclose the whole bar. In that case, the dependence to the macroscopic location x in $\chi_s^{\varepsilon_0}$, $G_s^{\varepsilon_0}$, $H_s^{\varepsilon_0}$ and $E_s^{\varepsilon_0}$ disappears.
- the step (1) of the implicit construction procedure involves solving (133) with periodic boundary conditions on Y_x. This step implies the use of a finite element solver on a single large domain (if Y_0 is set as the whole bar) or on a set of smaller domains (Y_x) and this implies that a mesh, or a set of meshes, of the elastic properties in the Y_x domain must be designed. Therefore, even if the meshing problem for the elastic wave propagation in the order 0 homogenized model is much simpler than for the original model, the problem is still not mesh free. Indeed, fine meshes must still be designed to solve the homogenization problem. Nevertheless, these meshes can be based on tetrahedra even if the wave equation solver is based on hexahedra. Moreover, as the homogenization problem is time independent, the consequences of very small or badly shaped elements on the computing time are limited.

We can check that this procedure gives a correct result on our 1-D case:

1. Taking Y_x as $\mathbb{R}$, the first step allows finding $\partial_y \chi_s^{\varepsilon_0}(y) = \frac{C}{E}(\varepsilon_0 y) - 1$, where $C = \left(\lim_{T\to\infty} \frac{1}{2T}\int_{-T}^{T} \frac{1}{E}(x)dx\right)^{-1}$
2. H^{ε_0} and G^{ε_0} are straight forward to compute from step (i). We have

$$G^{\varepsilon_0}(x,y) = \frac{1}{\mathcal{F}^{\varepsilon_0}\left(\frac{1}{E}\right)}(x)\left(\frac{1}{E} - \mathcal{F}^{\varepsilon_0}\left(\frac{1}{E}\right)\right)(\varepsilon_0 y) + 1 \tag{154}$$

where the fact that, for any h, $\mathcal{F}(h)(x/\varepsilon_0) = \mathcal{F}^{\varepsilon_0}(h)(x)$. We also find $H^{\varepsilon_0}(x,y) = \left(\mathcal{F}^{\varepsilon_0}\left(\frac{1}{E}\right)(x)\right)^{-1}$.

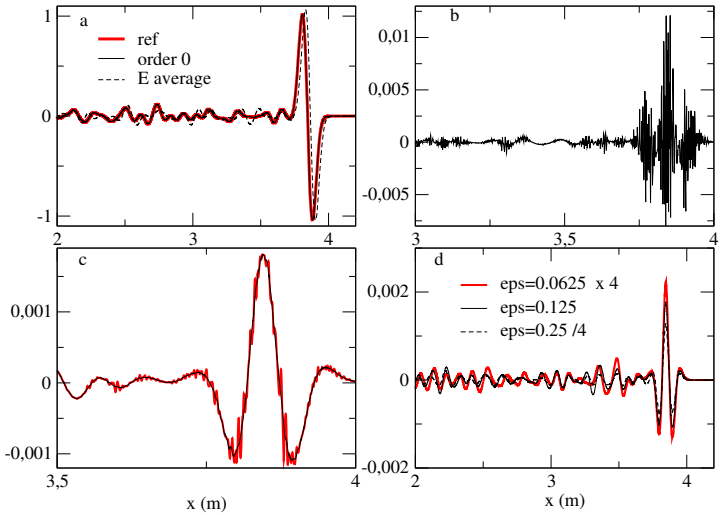

Figure 14: Results of the numerical example in 5.7.1.
a: displacement $u^{\text{ref}}(x,t)$ at t =4.9 10^{-3} s computed in a random bar model (red), the order 0 homogenized solution $u^0(x,t)$ (black) and the solution computed in a model obtained by averaging the elastic properties ($\mathcal{F}^{\varepsilon_0}(\rho)$ and $\mathcal{F}^{\varepsilon_0}(E)$) (dashed).
b: order 0 residual, $u^0(x,t) - u^{\text{ref}}(x,t)$.
c: order 1 residual (red), $u^0(x,t) + u^1(x,t) - u^{\text{ref}}(x,t)$. Partial order 2 residual (it is partial because $\langle u^2 \rangle$ is not computed) (black).
d: Partial order 2 residual for $\varepsilon_0 = 0.125$mm (black), partial order 2 residual for $\varepsilon_0 = 0.0625$mm with amplitude multiplied by 4 (red) and partial order 2 residual for $\varepsilon_0 = 0.25$mm with amplitude divided by 4 (dashed).

3. the third step allows to find

$$E^{\varepsilon_0}(x,y) = \left(\left(\frac{1}{E} - \mathcal{F}^{\varepsilon_0}\left(\frac{1}{E}\right)\right)(\varepsilon_0 y) + \mathcal{F}^{\varepsilon_0}\left(\frac{1}{E}\right)(x)\right)^{-1} \tag{155}$$

$$E^{*,\varepsilon_0}(x) = \left(\mathcal{F}^{\varepsilon_0}\left(\frac{1}{E}\right)(x)\right)^{-1} \tag{156}$$

which are the desired results.

5.7 Two examples

5.7.1 1-D bar with random properties

In Fig. 14, using the same random bar as for Fig. 5, we present some results obtained using the non-periodic method developed above. In Fig. 14a, we compare the reference solution with the order 0 non-periodic homogenized solution and a solution

obtained using a naive up-scaling (with $E^* = \mathcal{F}^{\varepsilon_0}(E)$, the "E average" solution). Note the strong coda wave trapped in the random model on the left of the ballistic pulse which was not at all present in the periodic case. As expected, the "E average" solution is not in phase with the reference solution and shows that this "natural" filtering is not accurate. On the other hand, the order 0 homogenized solution is already in excellent agreement with the reference solution, as we have already seen with the Backus solution. In Fig. 14b the residual between the order 0 homogenized solution and the reference solution $u^0(x,t) - u^{\text{ref}}(x,t)$ is shown. The error amplitude reaches 1% and contains fast variations. In Fig. 14c the order 1 residual $(u^0 + u^1)(x,t) - u^{\text{ref}}(x,t)$ (bold red line) and the partial order 2 residual (it is partial because the $\langle u^2 \rangle$ is not computed) is shown. The order 2 solution development has not been presented, but it can be computed similarly as the order 1 (Capdeville et al., 2010a). By comparing Fig. 14b and Fig. 14c, it can be seen that the order 1 periodic corrector removes most of the fine-scale variations present in the order 0 residual. The remaining fine-scale variations residual disappear with the partial order 2 residual. The remnant smooth residual is due to the $\langle u^2 \rangle$ that is not computed. To check that this residual is indeed a ε_0^2 residual, the same residual, computed for $\varepsilon_0 = 0.125$ is compared to the partial order 2 residual computed for $\varepsilon_0 = 0.0625$ (multiplying its amplitude by 4) and for $\varepsilon_0 = 0.25$ (dividing its amplitude by 4). It can be seen that these three signals overlap but not completely. This is consistent with a ε_0^2 residual but it shows that the approximations made, mainly the fact that support of the filters w_{ε_0} has been truncated to make their support finite, has some effect on the convergence rate (it is not completely an order 2 convergence).

5.7.2 1-D bar with random properties but no smooth variations

From the 1-D bar with random properties used in the previous section, using the homogenization principle, we can create a heterogeneous bar that behaves as a homogeneous bar. For that, we build a medium (ρ^n, E^n) such that

$$\rho^n(x) = \rho^0 + \left(\rho - \mathcal{F}^{\varepsilon_0}(\rho)\right)(x), \tag{157}$$

$$E^n(x) = \left[\frac{1}{E^0} + \left(\frac{1}{E} - \mathcal{F}^{\varepsilon_0}\left(\frac{1}{E}\right)\right)(x)\right]^{-1}, \tag{158}$$

where (ρ, E) are the random properties used in the previous example and (ρ^0, E^0) are two constant mechanical properties. In Fig. 15, a snapshot of the wavefield computed in (ρ, E) and in (ρ^n, E^n) is plotted. Even if (ρ^n, E^n) is strongly heterogeneous and non-periodic, no scattering occurs during the wave propagation and the waves appears to propagate in a homogeneous medium. (ρ^n, E^n) contains only small scales variation and $(\rho^n)^* = \rho^0$ and $(E^n)^* = E^0$.

6 Two-scale homogenization: higher dimensions

On the one hand, the asymptotic expansion, the equations and how the equations are solved in higher dimensions are very similar to the 1-D case. On the other hand,

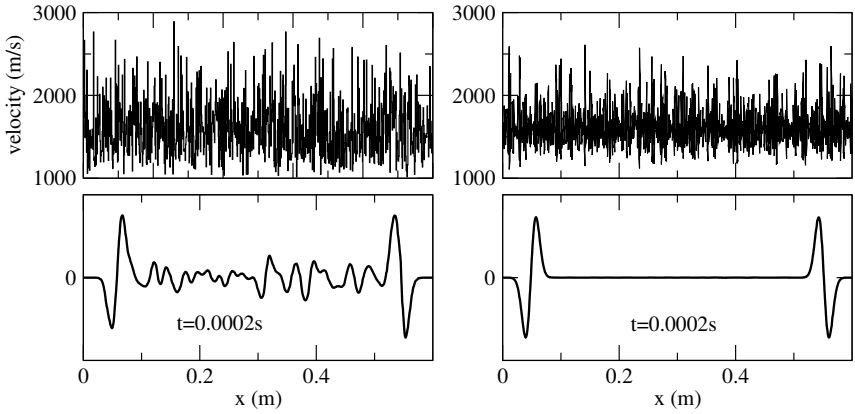

Figure 15: Top: elastic coefficient $E(x)$ along x (left) and elastic coefficient $E^n(x)$ along x following (158) (right). Bottom: displacement $u(x,t)$ snapshot for $t = 2.10^{-4}s$ in the heterogeneous bar (ρ, E) (left) and displacement $u(x,t)$ snapshot for the same time in the heterogeneous bar (ρ^n, E^n) (right).

many things that can be solved simply in 1-D, such as the cell problem, are more complex in 2-D and 3-D. Indeed, as we shall see later, the cell problem has no analytical solution in dimensions higher than 1.

In the following, we distinguish two cases: the elastic and the acoustic case.

6.1 The 2-D and 3-D elastic case

The elastic wave equations are

$$\rho \partial_{tt} \mathbf{u} - \boldsymbol{\nabla} \cdot \boldsymbol{\sigma} = \boldsymbol{f}\,, \tag{159}$$

$$\boldsymbol{\sigma} = \mathbf{c} : \boldsymbol{\epsilon}(\mathbf{u})\,, \tag{160}$$

where $\rho(\mathbf{x})$ is the material density and $\mathbf{c}(\mathbf{x})$ the elastic tensor for any $\mathbf{x}$ in a domain $\boldsymbol{\Omega}$ with boundary $\partial\boldsymbol{\Omega}$ and $\mathbf{c} : \boldsymbol{\epsilon} = \sum_{kl} c_{ijkl}\epsilon_{kl}$. We use the free boundary condition: $\boldsymbol{\sigma}(\mathbf{x}) \cdot \mathbf{n}(\mathbf{x}) = 0$ for $\mathbf{x} \in \partial\boldsymbol{\Omega}$ and where $\mathbf{n}(\mathbf{x})$ is the outward unit normal vector to $\partial\boldsymbol{\Omega}$ in $\mathbf{x}$.

$\mathbf{c}$, which is a 4th order elastic tensor such that in d-dimensions we have

$$\mathbf{c}(\mathbf{x}) = \{c_{ijkl}(\mathbf{x})\},\ (i,j,k,l) \in \{1,..,d\}^4\,,$$

is positive-definite and satisfies the following symmetries:

$$c_{ijkl} = c_{jikl} = c_{ijlk} = c_{klij}\,, \tag{161}$$

These symmetries reduce the maximum number of independent parameters necessary to characterize $\mathbf{c}$ to 6 in 2-D and to 21 in 3-D. The fact that $\mathbf{c}$ is positive-definite

is a necessary condition to ensure the uniqueness of the solution of the wave equation. Breaking this hypothesis leads to unforeseeable, generally wrong, results. This happens when one tries to model acoustic wave setting $V_S = 0$ in $\mathbf{c}$ within the solid wave equations. It is also an important condition for the homogenization.

6.1.1 Total anisotropy and isotropic projection

In the following, we will need represent some components of general, potentially anisotropic, elastic tensors $\mathbf{c}$. To do so, we choose to first project the general anisotropic $\mathbf{c}$ to the nearest isotropic tensor $\mathbf{c}^{\text{iso}}$ following Browaeys and Chevrot (2004). Then, P and S wave velocities are defined as

$$V_P(\mathbf{x}) = \sqrt{(c^{\text{iso}}_{1111}(\mathbf{x})/\rho(\mathbf{x}))}\,, \tag{162}$$

and, for the 2-D case,

$$V_S(\mathbf{x}) = \sqrt{(c^{\text{iso}}_{1212}(\mathbf{x})/\rho(\mathbf{x}))}\,, \tag{163}$$

and the total anisotropy, or the anisotropy index, as

$$\text{aniso}(\mathbf{x}) = \sqrt{\frac{\sum_{ijkl}(c^{\text{iso}}_{ijkl}(\mathbf{x}) - c_{ijkl}(\mathbf{x}))^2}{\sum_{ijkl}(c^{\text{iso}}_{ijkl}(\mathbf{x}))^2}}\,. \tag{164}$$

6.1.2 Asymptotic expansion

We jump directly to the non-periodic case, skipping the periodic case. The procedure is very similar to the 1-D case and, therefore, we show less details. They can nevertheless be found in Guillot et al. (2010); Capdeville et al. (2010b) and Cupillard and Capdeville (2018).

We first assume that we have been able to define $(\rho^{\varepsilon_0}(\mathbf{x},\mathbf{y}), \mathbf{c}^{\varepsilon_0}(\mathbf{x},\mathbf{y}))$ in $\mathcal{T}^2$ with the conditions

$$\begin{aligned} \rho^{\varepsilon_0}(\mathbf{x}, \mathbf{x}/\varepsilon_0) &= \rho(\mathbf{x})\,, \\ \mathbf{c}^{\varepsilon_0}(\mathbf{x}, \mathbf{x}/\varepsilon_0) &= \mathbf{c}(\mathbf{x})\,, \end{aligned} \tag{165}$$

and such that solutions to the following development has a solution.

The solution to the wave equations (159-160) is then sought as an asymptotic expansion in ε_0 with $\mathbf{u}^i$ and $\boldsymbol{\sigma}^i$ in $\mathcal{V}$:

$$\begin{aligned} \mathbf{u}(\mathbf{x},t) &= \sum_{i=0}^{\infty} \varepsilon_0^i \mathbf{u}^i(\mathbf{x}, \mathbf{x}/\varepsilon_0, t) = \sum_{i=0}^{\infty} \varepsilon_0^i \mathbf{u}^i(\mathbf{x}, \mathbf{y}, t)\,, \\ \boldsymbol{\sigma}(\mathbf{x},t) &= \sum_{i=-1}^{\infty} \varepsilon_0^i \boldsymbol{\sigma}^i(\mathbf{x}, \mathbf{x}/\varepsilon_0, t) = \sum_{i=-1}^{\infty} \varepsilon_0^i \boldsymbol{\sigma}^i(\mathbf{x}, \mathbf{y}, t)\,. \end{aligned} \tag{166}$$

where the superscript i is a power on ε_0 but not on $\mathbf{u}^i$ and $\boldsymbol{\sigma}^i$. Once again, the condition for $\mathbf{u}^i$ and $\boldsymbol{\sigma}^i$ to be in $\mathcal{V}$ is a strong condition which means that only large variations in $\mathbf{x}$ and fine variations in $\mathbf{y}$ are allowed. It is equivalent to the $\mathbf{y}$ periodic condition in the periodic case. Like in the 1-D case, both $\mathbf{u}^i$ and $\boldsymbol{\sigma}^i$ depend on ε_0. Note that, as already said for the 1-D case, to be fully consistent, we should define two ε (ε and ε_0) as it is done in Capdeville et al. (2010b). We skip that difficulty for the sake of simplicity.

6.1.3 Series of equations

Introducing expansions (166) in the wave equations (159-160) and using

$$\boldsymbol{\nabla} \to \boldsymbol{\nabla}_{\mathbf{x}} + \frac{1}{\varepsilon_0}\boldsymbol{\nabla}_{\mathbf{y}}\,, \tag{167}$$

we obtain:

$$\rho^{\varepsilon_0}\partial_{tt}\mathbf{u}^i - \boldsymbol{\nabla}_x \cdot \boldsymbol{\sigma}^i - \boldsymbol{\nabla}_y \cdot \boldsymbol{\sigma}^{i+1} = \boldsymbol{f}\delta_{i,0}\,, \tag{168}$$

$$\boldsymbol{\sigma}^i = \mathbf{c}^{\varepsilon_0} : \left(\boldsymbol{\epsilon}_x\left(\mathbf{u}^i\right) + \boldsymbol{\epsilon}_y\left(\mathbf{u}^{i+1}\right)\right)\,. \tag{169}$$

The external source is built as independent of $\mathbf{y}$.

6.1.4 Resolution

Solving (168) and (169) for $i = -2$ and $i = -1$ respectively makes it possible to show that $\boldsymbol{\sigma}^{-1} = 0$ and that $\mathbf{u}^0 = \left\langle \mathbf{u}^0 \right\rangle$. Then, equations (168) for $i = -1$ and (169) for $i = 0$ give

$$u_i^1(\mathbf{x},\mathbf{y}) = \chi_i^{\varepsilon_0,kl}(\mathbf{x},\mathbf{y})\epsilon^0_{x,kl}(\mathbf{x}) + \left\langle u_i^1 \right\rangle(\mathbf{x})\,. \tag{170}$$

where $\boldsymbol{\epsilon}^0_x = \boldsymbol{\epsilon}_x\left(\mathbf{u}^0\right)$ and $\boldsymbol{\chi}^{\varepsilon_0}$ is the first-order corrector, a 3rd order tensor. It is the solution in $\mathcal{V}$ of cell equation

$$\partial_{y_i} H_{ijkl}^{\varepsilon_0} = 0\,, \tag{171}$$

with

$$H_{ijkl}^{\varepsilon_0} = c_{ijmn}^{\varepsilon_0} G_{mnkl}^{\varepsilon_0}\,, \tag{172}$$

$$G_{ijkl}^{\varepsilon_0} = \frac{1}{2}\left(\delta_{ik}\delta_{jl} + \delta_{jk}\delta_{il} + \partial_{y_i}\chi_j^{\varepsilon_0,kl} + \partial_{y_j}\chi_i^{\varepsilon_0,kl}\right)\,, \tag{173}$$

where, to enforce the uniqueness of the solution, $\langle \boldsymbol{\chi}^{\varepsilon_0} \rangle = 0$ is imposed. Like in the 1-D case, we find the order 0 constitutive relation:

$$\left\langle \boldsymbol{\sigma}^0 \right\rangle = \mathbf{c}^{*,\varepsilon_0} : \boldsymbol{\epsilon}_x\left(\mathbf{u}^0\right)\,, \tag{174}$$

where the effective elastic tensor is

$$\mathbf{c}^{*,\varepsilon_0}(\mathbf{x}) = \left\langle \mathbf{H}^{\varepsilon_0} \right\rangle(\mathbf{x})\,. \tag{175}$$

To the contrary to the 1-D case, $\boldsymbol{\sigma}^0$, the order 0 stress, depends on $\mathbf{y}$ and therefore, $\langle \boldsymbol{\sigma}^0 \rangle \neq \boldsymbol{\sigma}^0$.

Equations (168) for $i = 0$ gives

$$\rho^{\varepsilon_0} \partial_{tt} \mathbf{u}^0 - \boldsymbol{\nabla}_x \cdot \boldsymbol{\sigma}^0 - \boldsymbol{\nabla}_y \cdot \boldsymbol{\sigma}^1 = \boldsymbol{f} \,. \tag{176}$$

Taking the cell average of the last equation, using property (3) and taking the $\boldsymbol{f}$ independence on $\mathbf{y}$ into account, we find

$$\rho^{*,\varepsilon_0} \partial_{tt} \mathbf{u}^0 - \boldsymbol{\nabla} \cdot \langle \boldsymbol{\sigma}^0 \rangle = \boldsymbol{f} \,, \tag{177}$$

where $\rho^{*,\varepsilon_0} = \langle \rho^{\varepsilon_0} \rangle$. The last equation together with the order 0 constitutive relation (174) are the order 0 effective wave equations. They form a classical elastic wave equation for the effective elastic model $(\rho^{*,\varepsilon_0}, \mathbf{c}^{*,\varepsilon_0})$.

6.1.5 Construction of the effective elastic tensor and density

To build the two-scale elastic tensor $\mathbf{c}(\mathbf{x}, \mathbf{y})$ and the effective elastic tensor $\mathbf{c}^{*,\varepsilon_0}$, we follow the procedure described in section 5.6.2.

Step 1. For a given elastic model defined by its elastic tensor $\mathbf{c}(\mathbf{x})$, we solve the following set of problems (6 in 3-D), called the cell problem, to find the initial guess for the corrector $\boldsymbol{\chi}_s^{kl}$:

$$\boldsymbol{\nabla} \cdot \boldsymbol{\sigma}^{kl} = -\boldsymbol{\nabla} \cdot (\mathbf{c} : (\hat{\mathbf{k}} \otimes \hat{\mathbf{l}})) \tag{178}$$

$$\boldsymbol{\sigma}^{kl} = \frac{1}{2} \mathbf{c} : \left(\boldsymbol{\nabla} \boldsymbol{\chi}_s^{kl} + {}^t\boldsymbol{\nabla} \boldsymbol{\chi}_s^{kl} \right) \tag{179}$$

with periodic boundary conditions and $\hat{\mathbf{k}}$ and $\hat{\mathbf{l}}$ being the space basis unit vectors.

This is a simple static elastic equation with a set of loading. Currently, we have two solvers, both in 2-D and 3-D, to solve them:

- Based on a finite element method. This method requires a finite element mesh based on tetrahedron but is accurate. It is the approach used in Capdeville et al. (2010b) and Cupillard and Capdeville (2018).
- Based on Fast Fourier Transform (FFT) method (Moulinec & Suquet, 1998; Michel et al., 1999). This method is easy to implement and does not need a mesh. It may present some limitations in the case of discontinuous media with very strong contrast, but experience shows that it gives good results, even in that case (Capdeville et al., 2015).

Step 2. Once the initial corrector $\boldsymbol{\chi}_s^{kl}$ has been obtained,

- We compute the following tensors:

$$\begin{aligned} \mathbf{G}_s(\mathbf{x}) &= \mathbf{I} + \frac{1}{2} \left(\boldsymbol{\nabla} \boldsymbol{\chi}_s + {}^T\boldsymbol{\nabla} \boldsymbol{\chi}_s \right) \\ \mathbf{H}_s(\mathbf{x}) &= \mathbf{c} : \mathbf{G}_s \end{aligned} \tag{180}$$

- The ε_0 effective tensor can be computed as

$$\mathbf{c}^{*,\varepsilon_0}(\mathbf{x}) = \mathcal{F}^{\varepsilon_0}(\mathbf{H}_s) : \mathcal{F}^{\varepsilon_0}(\mathbf{G}_s)^{-1}(\mathbf{x}) \tag{181}$$

- The effective density is then simply:

$$\rho^{*,\varepsilon_0} = \mathcal{F}^{\varepsilon_0}(\rho)$$

- Finally, the two-scale tensor $\mathbf{G}^{\varepsilon_0}(\mathbf{x}, \mathbf{x}/\varepsilon_0)$, $\mathbf{H}^{\varepsilon_0}(\mathbf{x}, \mathbf{x}/\varepsilon_0)$ and $\boldsymbol{\chi}^{\varepsilon_0}(\mathbf{x}, \mathbf{x}/\varepsilon_0)$ can also be built.

Step 3.

- The solution $\mathbf{u}^0$ can be obtained by solving the effective wave equation:

$$\rho^{\varepsilon_0} \cdot \partial_{tt}\mathbf{u}^0 - \boldsymbol{\nabla} \cdot \left\langle \boldsymbol{\sigma}^0 \right\rangle = \boldsymbol{f} \tag{182}$$

$$\left\langle \boldsymbol{\sigma}^0 \right\rangle = \mathbf{c}^{*,\varepsilon_0} : \boldsymbol{\epsilon}\left(\mathbf{u}^0\right) \tag{183}$$

- Once the order 0 solution is obtained, we can access to the order 0 stress and deformation with:

$$\boldsymbol{\sigma}^0(\mathbf{x}, \mathbf{x}/\varepsilon_0) = \mathbf{H}^{\varepsilon_0}(\mathbf{x}, \mathbf{x}/\varepsilon_0) : \boldsymbol{\epsilon}\left(\mathbf{u}^0\right)(\mathbf{x}) \tag{184}$$

$$\boldsymbol{\epsilon}^0(\mathbf{x}, \mathbf{x}/\varepsilon_0) = \mathbf{G}^{\varepsilon_0}(\mathbf{x}, \mathbf{x}/\varepsilon_0) : \boldsymbol{\epsilon}\left(\mathbf{u}^0\right)(\mathbf{x}) \tag{185}$$

- The partial order 1 displacement is then obtained as:

$$\mathbf{u}(\mathbf{x}) = \mathbf{u}^0(\mathbf{x}) + \varepsilon_0 \boldsymbol{\chi}^{\varepsilon_0}(\mathbf{x}, \mathbf{x}/\varepsilon_0) : \boldsymbol{\epsilon}(\mathbf{u}^0)(\mathbf{x}) + O(\varepsilon_0)\,. \tag{186}$$

  In practice, the last formula often converges as $O(\varepsilon_0^2)$ because $\left\langle \mathbf{u}^1 \right\rangle$ is small.

Remark: In the periodic case, the major symmetry of the effective elastic tensor can be demonstrated (e.g. Sanchez-Palencia (1980) or section 2.4 of Pavliotis and Campus (2004)). However, this is not currently the case in the non-periodic case: (181) does not warranty the symmetry of $\mathbf{c}^{*,\varepsilon_0}$. In most cases, $\mathbf{c}^{*,\varepsilon_0}$ is very close to being symmetric, but some cases can lead to a significant non-symmetry, which contradicts the energy conservation of the wave equation. There is currently no solution to this problem and, in practice, we just use the symmetric part of $\mathbf{c}^{*,\varepsilon_0}$ without tampering the convergence and the accuracy of the method.

6.2 The 2-D and 3-D acoustic case

The acoustic case is interesting because it leads to a non-intuitive concept: the density anisotropy. The full description of this case can be found in Cance and Capdeville (2015).

The primary variable of the acoustic wave equation often is the pressure p. Here, we use the velocity potential q, defined by $p = \dot{q}$, so that the acoustic wave equation in a domain $\mathbf{\Omega}$ is

$$\frac{1}{\kappa}\partial_{tt}q - \boldsymbol{\nabla}\cdot\dot{\mathbf{u}} = \dot{g}\,, \tag{187}$$

$$\dot{\mathbf{u}} = \frac{1}{\rho}\boldsymbol{\nabla}q\,. \tag{188}$$

The natural boundary condition on $\partial\mathbf{\Omega}$ is $q = 0$, that is zero pressure.

In the following, it is useful to define the inverse density tensor,

$$\mathbf{L} = \frac{1}{\rho}\mathbf{I}\,, \tag{189}$$

where $\mathbf{I}$ is the identity tensor. (188) can then be rewritten as

$$\dot{\mathbf{u}} = \mathbf{L}\cdot\boldsymbol{\nabla}q\,. \tag{190}$$

Following the elastic case, we can use an asymptotic expansion for q and $\mathbf{u}$:

$$q(\mathbf{x},t) = \sum_{i=0}^{\infty}\varepsilon_0^i q^i(\mathbf{x},\mathbf{y},t)\,, \tag{191}$$

$$\mathbf{u}(\mathbf{x},t) = \sum_{i=0}^{\infty}\varepsilon_0^i \mathbf{u}^i(\mathbf{x},\mathbf{y},t)\,, \tag{192}$$

still with $\mathbf{y} = \mathbf{x}/\varepsilon_0$. The series of equations to be solved can be obtained in a very similar way to the elastic case. Once solved, we obtain that, to the leading order, the effective velocity potential q^* and the effective displace $\mathbf{u}^*$ are solution of the following effective acoustic wave equations:

$$\frac{1}{\kappa^*}\partial_{tt}q^* - \boldsymbol{\nabla}\cdot\dot{\mathbf{u}^*} = \dot{g}^* \tag{193}$$

$$\dot{\mathbf{u}}^* = \mathbf{L}^{*,\varepsilon_0}\cdot\boldsymbol{\nabla}q^* \tag{194}$$

where

$$q^* = q^0\,, \tag{195}$$

$$\mathbf{u}^* = \left\langle \mathbf{u}^0 \right\rangle\,. \tag{196}$$

The effective bulk modulus is obtained similar to effective density of the elastic case:

$$\frac{1}{\kappa^*} = \mathcal{F}^{\varepsilon_0}\left(\frac{1}{\kappa}\right)\,. \tag{197}$$

The procedure for effective inverse density tensor is the same as the elastic tensor

$$\mathbf{L}^{*,\varepsilon_0} = \mathcal{F}^{\varepsilon_0}(\mathbf{P}_s)\cdot\mathcal{F}^{\varepsilon_0}(\mathbf{Q}_s)\,, \tag{198}$$

where $\mathbf{P}_s$ and $\mathbf{Q}_s$ are obtained by first solving the cell problem to obtain the starting corrector $\boldsymbol{\chi}_s$:

$$\boldsymbol{\nabla} \cdot \mathbf{u}^i = -\boldsymbol{\nabla} \cdot (\mathbf{L} \cdot \hat{\mathbf{i}}) \tag{199}$$

$$\mathbf{u}^i = \mathbf{L} \cdot \boldsymbol{\nabla} \chi_s^i \,, \tag{200}$$

with periodic boundary conditions. Then, $\mathbf{P}_s$ and $\mathbf{Q}_s$ are built as:

$$\mathbf{Q}_s = \mathbf{I} + \boldsymbol{\nabla} \boldsymbol{\chi}_s \,, \tag{201}$$

$$\mathbf{P}_s = \mathbf{L} \cdot \mathbf{Q}_s \,. \tag{202}$$

As it can be seen, the principle and process is very similar to the elastic case. Nevertheless, it leads to interesting differences:

- the anisotropy is carried by the inverse density tensor and not the elastic tensor. It implies that the effective density is anisotropic even though the fine-scale density is isotropic. As a result, the apparent density depends on the direction of the wave propagation, which is unusual. For a finely layered horizontal medium, we have

  $$\mathbf{L}^{*,\varepsilon_0} = \begin{pmatrix} \mathcal{F}^{\varepsilon_0}\left(\frac{1}{\rho}\right) & 0 \\ 0 & \frac{1}{\mathcal{F}^{\varepsilon_0}(\rho)} \end{pmatrix} \tag{203}$$

  which implies a simple but real anisotropy;

- the physical acoustic anisotropy (in contrast to the non-physical anisotropy introduced in exploration geophysics to mimic elastic anisotropy in acoustic media (Alkhalifah, 2000)) is different from the elastic anisotropy. It is always purely elliptic (the wavefront is elliptic), whereas the simplest elastic anisotropy (vertically transverse anisotropy, VTI) is rather complex (the wavefront has a diamond shape). See Fig. 6.2 and Cance and Capdeville (2015) for more details.

- The order 0 displacement behaves similarly to the elastic stress and depends on the fine-scale $\mathbf{y}$:

  $$\mathbf{u}^0(\mathbf{x}, \mathbf{y}) = (\mathbf{I} + \boldsymbol{\nabla} \boldsymbol{\chi}(\mathbf{x}, \mathbf{y})) \cdot \boldsymbol{\nabla} q^*(\mathbf{x}) \,. \tag{204}$$

  It can be seen that, to the leading order, the acoustic displacement is sensitive to small structures unlike in the elastic case. It implies that the acoustic displacement is strongly affected by small scale heterogeneities similar to strain in the elastic case.

From the point of view of small scales, the acoustic and the elastic cases are physically different despite being mathematically very similar. These differences can be important: for example, many full waveform inversion tests are performed in the acoustic case, using a spatially constant density and inverting for the acoustic velocity (or κ). This case is a poor proxy of the elastic case as it is similar to only invert for the density in the elastic case. Based on homogenization, we see that it is important to allow density variations so that such tests make sense.

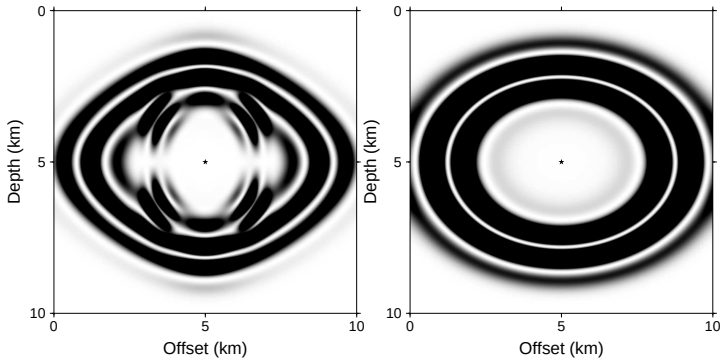

Figure 16: Energy snapshot of a 2-D wave propagation for an isotropic source (an explosion) at the center of each plots in an elastic VTI medium (left) and in an anisotropic acoustic media with similar main axis velocities (right).

7 What we skipped

Some important aspects of the homogenization theory have not been addressed in the present article.

7.1 Spatial filters

In this paper, we have used a single type of spatial filter (Fig. 1). Many other types of filters could be used, depending on applications, and we have not discussed this aspect so far.

The choice of the filter is always a compromise to address as best as possible the following points:

1. the filter spectrum must be as close as possible to 1 in $[0, k_{\max}]$;
2. the filter spectrum must go down to zero as quickly as possible after $k_{\max}$;
3. in the time domain, the filter must be as compact as possible;
4. the effective medium must be defined.

Only a strictly positive filter wavelet can make sure point 4 is achieved for all cases. This is the choice of Backus (1962) using a Gaussian filter. Even if for some very strongly contracted media a Gaussian filter might be the only option available, we try to avoid this possibility because it makes point 1 and 2 more difficult to achieve. Most often, we use the filter presented in Fig. 1 because of its flat spectrum norm between the 0 spatial frequency and $1/\lambda_0$, which is optimal to leave the medium intact in the desired spatial frequency band. Nevertheless, for strongly contrasted media, its negative lobes in the space domain may break point 4. In such cases, it can be necessary to use a positive filter, such as a Gaussian filter.

7.2 Boundary conditions

Domain boundaries are always a difficulty for the homogenization theory because the periodicity of the cell problem makes it impossible to introduce them in a simple way. A classical solution to tackle this difficulty is the matched asymptotic approach, mainly developed for the static periodic case (Sanchez-Palencia, 1986; Dumontet, 1990; Nevard & Keller, 1997; Marigo & Pideri, 2011; David et al., 2012). The idea is to use two asymptotic expansions: one in the volume (let us say $(\mathbf{u}^i, \boldsymbol{\sigma}^i)$) and one specifically for the boundary (let us say $(\mathbf{v}^i, \boldsymbol{\tau}^i)$), and to match them. The area near the boundary where $(\mathbf{v}^i, \boldsymbol{\tau}^i)$ is valid is the boundary layer. Fig. 17 displays a sketch of the situation with a fine-scale topography. The solution in the boundary layer and the matching conditions provide the boundary condition for the effective volumetric solution, which, to the order 1, is in general a Dirichlet-to-Neumann condition:

$$\boldsymbol{\sigma}^0(\mathbf{x}) \cdot \mathbf{n} = \varepsilon_0 \left(h(\mathbf{x}) \partial_{tt} \mathbf{u}^0(\mathbf{x}) + \alpha(\mathbf{x}) \boldsymbol{\nabla}_{\mathbf{p}} \cdot \boldsymbol{\sigma}^0 \cdot \mathbf{p} \right) \text{ for } \mathbf{x} \in \boldsymbol{\Gamma}_s \,, \tag{205}$$

where $\boldsymbol{\Gamma}_s$ is the effective topography, $\mathbf{n}$ the outward unit vector normal to $\boldsymbol{\Gamma}_s$, $\mathbf{p}$ the unit vector tangential to $\boldsymbol{\Gamma}_s$, and h and α two smooth coefficients which depend on the fine-scale topography and on the fine-scale heterogeneities near the free surface. These two coefficients are obtained thanks to the matched conditions. If there is no fine-scale topography and just fine-scale heterogeneities below a smooth free surface, then $\boldsymbol{\Gamma}_s = \boldsymbol{\Gamma}$.

This method has been applied to the dynamic non-periodic case for layered media (Capdeville & Marigo, 2008) and for fine-scale topography (Capdeville & Marigo, 2013). For fine-scale topography, it appears that the effective topography is not the average topography but rather a smooth lower envelop of the fine-scale topography, as sketched in Fig. 17. A casual explanation for this is that surface waves propagate below the fine-scale topography, and the only effect of the fine-scale topography is to weigh on the effective topography (through the coefficient h in (205)). Note that a solution exists to make the boundary condition valid up to the order 1 without changing it if lateral variations below the free surface are smooth (Capdeville & Marigo, 2007). Finally, the case of fine-scale heterogeneity below a smooth or a fine-scale topography remains to be studied, but it is expected to be similar to the fine-scale topography case alone.

7.3 Other aspects to address

Many other aspects have not been mentioned or studied. Among them, the fact that λ_{min} can strongly vary with location in $\boldsymbol{\Omega}$, would need to be studied. For example, in most of the kilometer scale geological models, the S wave speed can vary by a factor 10 from the top to the bottom, implying a factor 10 change of λ_{min} through the domain. Knowing that λ_0 is fixed, the ε_0, and therefore the quality of the solution, changes with depth. This is a problem, and an "adaptive" homogenization, making ε_0 constant through the domain, is needed. A solution valid for layered media exists and is based on a normal mode solution decomposition, a kind of adaptive filtering

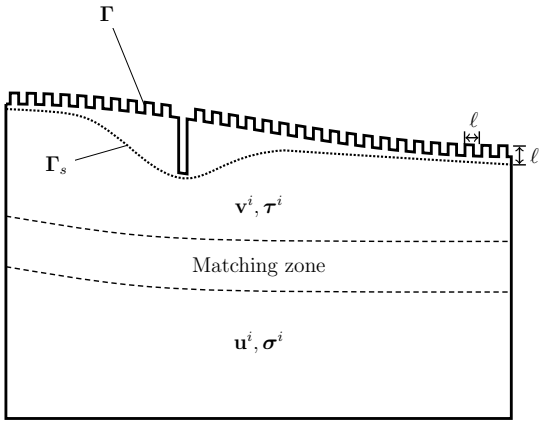

Figure 17: Sketch of the matched asymptotic approach. $\mathbf{\Gamma}$ is the fine-scale free surface; $\mathbf{\Gamma}_s$ is the effective free surface; $(\mathbf{v}^i, \boldsymbol{\tau}^i)$ is the asymptotic expansion valid close to the free surface; $(\mathbf{u}^i, \boldsymbol{\sigma}^i)$ is the asymptotic expansion valid away from the free surface. In this sketch, the topography presents some local periodicity, but it is not necessarily the case as shown by Capdeville and Marigo (2013).

(see Capdeville et al. (2013), appendix B). It needs to be extended to general media and this aspect will be addressed in the near future.

Another aspect that would need a careful study is the solid-fluid coupling when both the solid and fluid domains are larger than λ_{min}.

8 Examples of applications

In this section, we show a series of applications of the two-scale non-periodic homogenization, one in the context of inversion and the rest in the context of forward modeling. Most of them are 2-D examples and one of them is in 3-D (Sec. 8.4). The latter is a typical example of what can be expected from the method to simplify the forward modeling and make it much faster. More examples can be found in the two-scale non-periodic homogenization bibliography already cited.

8.1 2-D refracted waves

One of the concerns often expressed about homogenization is its capacity to model back-scattered or refracted waves. It is not really clear why such a concern exists because there is nothing specific about those waves: the convergence of homogenization is true for the wavefield as a whole and it should work equally well for all waves within the bounds of the method hypothesis. Perhaps the concern about back-scattered waves is linked to the fact that it is more difficult to obtain reflected waves than transmitted waves in smooth media. Similarly, the concern about re-

	V_P (km s^{-1})	V_S (km s^{-1})	ρ (kg m^{-3})
upper layer	2.4	1.2	1500
lower layer	5.6	2.8	2800

Table 1: Elastic properties for the refracted wave tests (see Fig. 18)

fracted waves may be linked to the belief that a sharp contrast is important because such waves propagate along the interface for a long time. In any case, we show in the following example that both back-scattered and refracted waves can be accurately modeled in the homogenized models.

To verify that the reflected and refracted waves are correctly modeled in the homogenized model, we present two tests in a simple 2-D two layer elastic setting with a free surface on the top, as presented in Fig. 18a. The elastic properties are given in Tab. 1. The vertical transition between the two layers is not a simple step, but something a bit more complex. In model a, the elastic properties alternate vertically between the upper and the lower layer properties for 65 m (Fig. 18b). In model b, at a height of 65 m, the elastic properties alternate horizontally between the upper and the lower layer (Fig. 18c). We compute the reference solutions using SEM, meshing all the interfaces and using Perfectly Matched Layers (PML, Festa & Vilotte, 2005) as absorbing boundaries around the domain. The wavefield is generated by an explosion located 500 m below the free surface using a Ricker source time wavelet with a central frequency of 5 Hz and a maximum frequency of 15 Hz. An energy snapshot of the wavefield at $t = 2.6\ s$ is displayed in Fig. 18d for model a. Because of the very fine elements imposed by the heterogeneities, the numerical cost of the simulations is about 100 times more expensive than a similar simulation without the fine structures.

Once the reference solutions are obtained, we compute the two homogenized models with $\varepsilon_0 = 0.6$ where we use the smallest V_S velocity to evaluate λ_{min} (note that we obtain $\varepsilon_0 = 0.25$ if we use the lower layer V_S value instead). Vertical cross-section in the homogenized models are shown in Fig. 19.

The "model a" is purely layered and the Backus homogenization is enough for such a model. The "model b" is not layered and we rely on the two-scale homogenization method presented in the work, using the finite element version of our homogenization tool. The effective model cross-sections show smooth elastic models with a significant anisotropy localized around the interface for both cases.

Vertical velocity traces for the two receivers and for both models are plotted in Fig. 20. The traces computed in a model obtained by low-pass filtering the slowness and the density using the same ε_0 as for the homogenization are also displayed. These traces are plotted to show what happens if one decides to approximate the true model by its low-pass filtered version. These naive up-scaled models are smooth but purely isotropic. Receiver 1 is close to the source and mainly records reflected waves. Receiver 2 has a larger offset and records also many refracted waves. While the "slowness average" traces show large time shifts with respect to the reference solution with increasing time, the homogenized effective traces show a better accu-

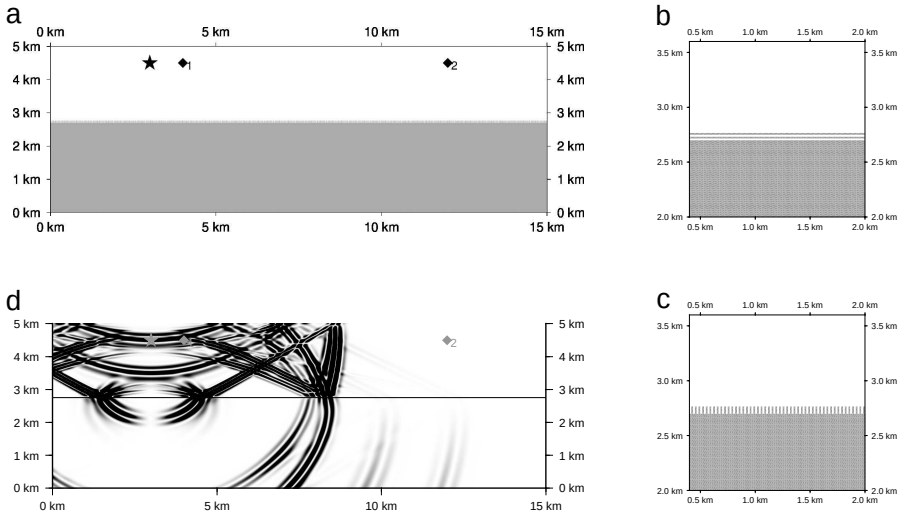

Figure 18: a: Two layered domain used for the "refracted wave" tests. The explosion source location is indicated by the star and the two receivers locations by the diamonds. The gray background corresponds to the elastic properties in the "lower layer" in Tab. 1 and the white background to properties in the "upper layer". b: zoom on the transition area between the lower and upper layer for the "model a". c: same as b but for "model b". d: Energy snapshot in model a at $t = 2.6s$.

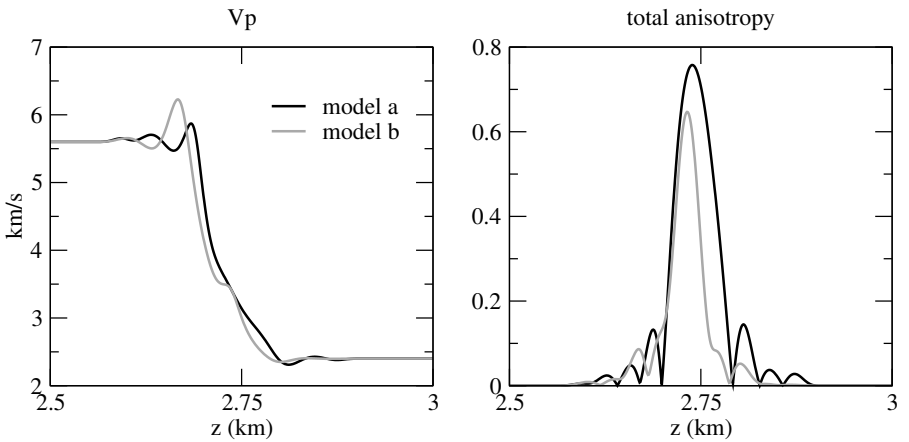

Figure 19: Vertical cross-section in the homogenized effective from "model a" (black) and "model b" (gray). The isotropic projection, as defined in Sec. 6.1, of the effective elastic tensor corresponding to P wave velocity (left panel) and the total anisotropy (right panel) are shown.

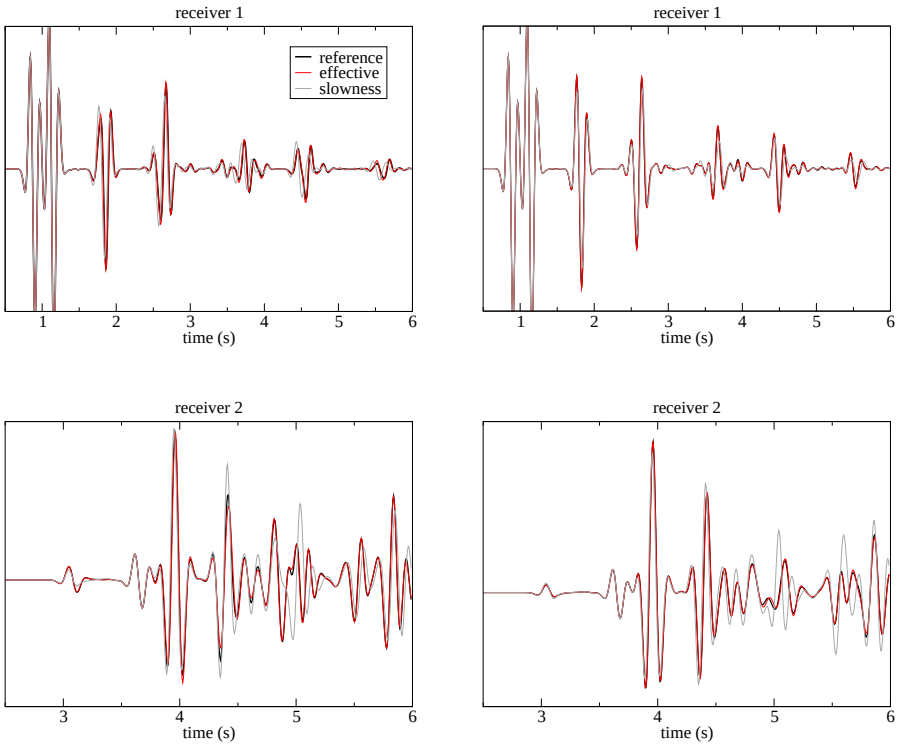

Figure 20: Vertical velocity traces computed in “model a” (top panels) and “model b” (bottom panels) for receivers 1 (left panels) and receivers 2 (right panels). The reference traces are displayed (black) as well as the homogenized effective solution (red) and the slowness averaged solution (gray).

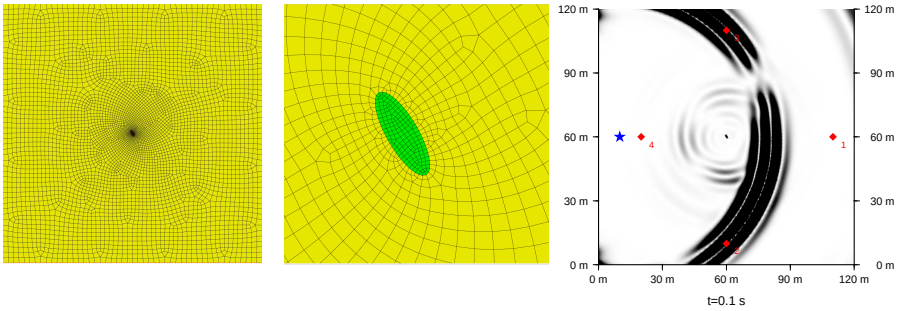

Figure 21: Left: quadrangular mesh of the domain (120x120m^2). The gray lines represent the mesh used to model the wave propagation in the effective medium. Middle: zoom on the elliptic fluid inclusion mesh (the long axis is 1.5mm and the short axis is 0.5mm long). Right: energy snapshot for a moment tensor source (blue star) at t=0.1s.

racy for the whole time window. If a better accuracy is needed, it is enough to lower ε_0 and the error will decrease as ε_0^2 in the case of homogenization but will converge poorly in the slowness average case.

To conclude this example, we can say that homogenized effective models can model back-scattered and refracted waves with no difficulty whatsoever.

8.2 A solid with a fluid inclusion

Media with both solid and fluid parts are common in geophysics. At very large scales, the outer core or the oceans are fluid, and at local scales, fluid regions can be, for example, gas reservoirs. The classical solution to compute the wavefield in such cases is to separate the fluid and solid into two distinct domains, to use the appropriate set of equations in each of them and to couple them. As usual, it creates meshing difficulty and it would be very interesting to be able to homogenize both domains at once. Unfortunately, this is not possible because one of the mathematical conditions to solve the cell problem is that the elastic or acoustic tensor must be positive-definite. This implies that setting V_S to zero in a solid to make it fluid is, in general, not possible and so is the option to mix solid and fluid in a single domain.

Even if it is in principle not possible, we will show in this section that we can homogenize a solid with fluid inclusions if the inclusions are small compared to λ_{min}. As a test example, we use here single elliptic inclusion in an homogeneous media (see Fig. 21 for the geometry and Tab. 2 for the mechanical properties of the domain). The effective medium can be computed using finite element and domain decomposition, with the acoustic equations in the fluid domain and the elastic equation in the solid. Here we have used very small value for V_S in the fluid. Such a simplification is, in general, a bad idea but, as we will see it below, as long as the inclusion remains small, it gives a good result. An example of the obtained effective media is shown in

	V_P (km s^{-1})	V_S (km s^{-1})	ρ (kg m^{-3})
background	1.8	1	2000
ellipse	1	0	1000

Table 2: Elastic properties for the fluid ellipse inclusion test (see Fig. 21)

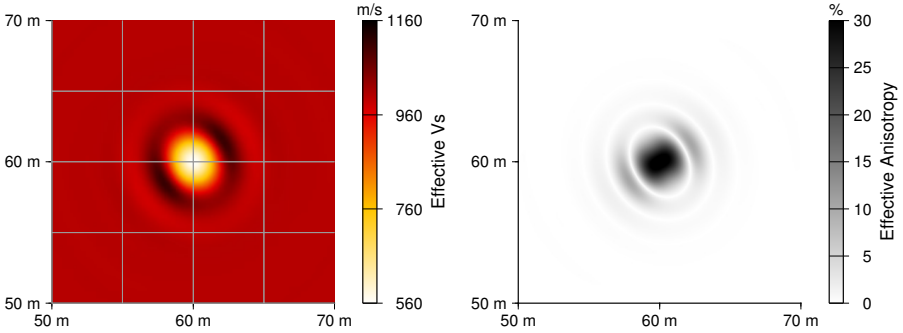

Figure 22: Zoom in on the effective medium computed with $\lambda_0 = 5\,\text{m}$. Left: Isotropic V_S velocity. Right: total anisotropy. (see Sec. 6.1 for the "total anisotropy" and isotropic V_P definitions.)

Fig. 22. It is fully anisotropic and, to represent it, we follow the quantities defined in Sec. 6.1.

For the ellipse presented in Fig. 21, we computed three reference solutions, using three different source wavelet maximum frequencies, such that the minimum wavelengths in the background medium are λ_{min} =10, 5 and 2.5 m. We computed the 3 effective media for each λ_{min}, with $\varepsilon_0 = 0.5$. Then, for each of these effective media, we computed the effective wave equation solutions and compared them with the respective reference solutions as shown in Fig. 23 for receiver 4 (which records the back-scattered wavefield from the ellipse inclusion). It can be seen that the effective solution is of good quality when the size of the inclusion is very small compared to λ_{min} (top panel in Fig. 23), but is of poorer quality when it is not that small (bottom panel in Fig. 23). Although it depends on the desired accuracy, we can say that the effective solution is of good quality if the inclusion is smaller than $\lambda_{\text{min}}/3$. Note that the effective solution is obtained using a very sparse mesh (a sample of the mesh is shown in Fig. 22, left plot) compared to the reference solution. Consequently, the effective solution is obtained more than 100 times faster than the reference solution. This example is interesting but it is clear that this option will fail if one tries to go beyond the small inclusion case, for example, if the small inclusions are connected. The other way (solid inclusions into a fluid) works similarly: it can be homogenized as a single fluid as long as S waves cannot develop in the solid inclusion, that is as long as they are small compared to λ_{min}. Finally, note that void inclusions can be also treated the same way.

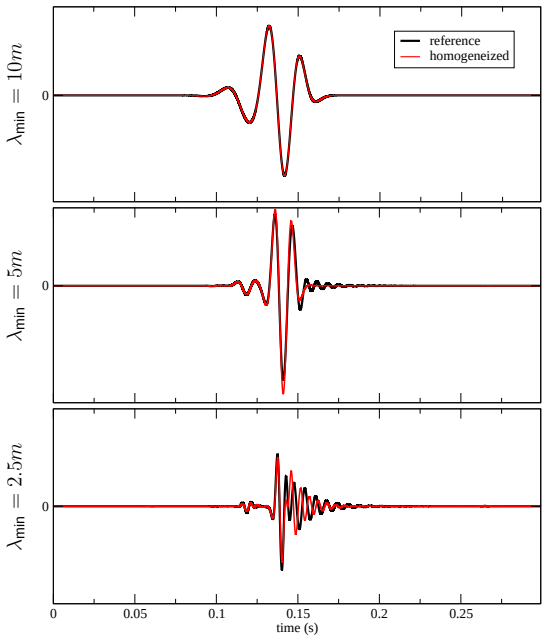

Figure 23: Comparison of vertical velocity traces between the reference solution (black) and the effective solution (red) for receiver 4, which is at a back-scattering location. $\varepsilon_0 = 0.5$ and is fixed. Top: the source maximum frequency is such $\lambda_{\text{min}} = 10$ m; middle: $\lambda_{\text{min}} = 5$ m; bottom: $\lambda_{\text{min}} = 2.5$ m.

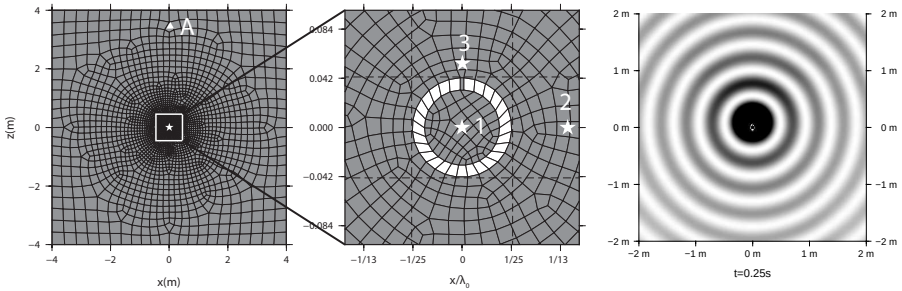

Figure 24: Homogeneous acoustic domain with an Helmholtz ring inclusion at the center. Left: spectral element mesh of the domain. Middle: zoom in on the Helmholtz resonator part. The λ_0 scaling factor for the horizontal axis corresponds to the wavefield dominant wavelength (about $3\lambda_{\text{min}}$). Right: energy snapshot for $t = 0.25\,\text{s}$. Even if the source is in A, the energy clearly rings from the Helmholtz resonator after some time.

8.3 A failing case: Helmholtz resonators

Helmholtz resonators are open cavities that can resonate at a surprisingly low frequency compared to the fundamental eigenfrequency of a similarly closed cavity. In Fig. 24 a numerical example in 2-D is shown: it is a simple open ring made of aluminum immersed in air (see the SEM mesh in the left and middle panels in Fig. 24). If a pressure source is placed a few wavelengths away after the ballistic wave has passed, the Helmholtz resonator continues ringing for a long time as it can be seen on the energy snapshot in the right plot of Fig. 24 and in the pressure trace for receiver 3 in the left plot of Fig. 25. This acoustic resonance is produced by a process analogous to the oscillation of a mass-spring oscillator. The resonator must contain a neck connected to the cavity filled with a large volume of fluid. The large volume of fluid acts as the spring, while the neck acts as the mass. For the specific shape of the Helmholtz resonator example used here (see Fig. 24), the natural frequency of a 2-D Helmholtz resonator as given by Mechel (2013) is approximately

$$f_H \simeq \frac{V_P}{2\pi}\sqrt{\frac{d}{\pi r^2 l}} \tag{206}$$

where l is the length of the neck, r is the diameter of the ring, d is the width of the neck. In the example used here, $f_H \simeq 383\ Hz$, which is much lower than the fundamental resonance frequency of an equivalent closed cavity ($\simeq 4\ kHz$).

This unusual resonance is a remarkable property for such a simple linear elastic system. It can be shown that, when reaching the resonance frequency, the medium dispersion relation becomes singular (Lemoult et al., 2013) and the wavefield no longer exhibits any minimum wavelength. This breaks the main hypothesis of homogenization (λ_{min} is undefined in that case) and makes any interpretation of the obtained effective medium beyond that frequency difficult and probably meaning-

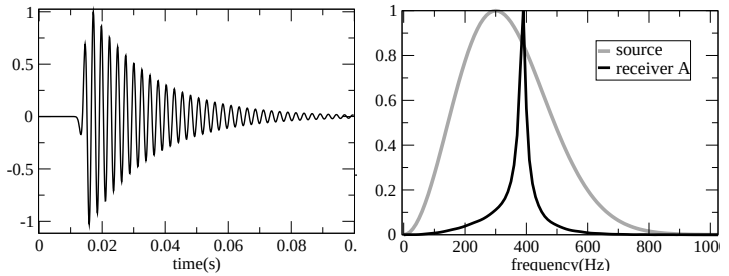

Figure 25: Left: pressure signal recorded for receiver 3 and source A (see Fig. 24). Right: source wavelet and the amplitude spectra of receiver 3.

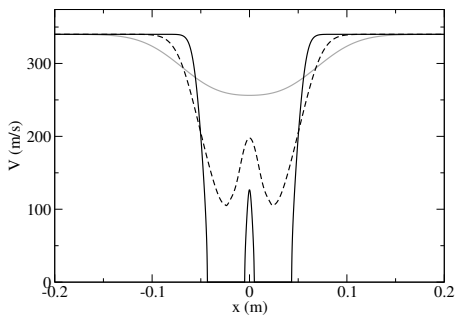

Figure 26: Horizontal cross section in $V_h = \sqrt{\kappa^{\varepsilon_0 *} L_{22}^{*,\varepsilon_0}}$ for $y = 0.02\,m$ (at the Helmholtz resonator neck level) and for three values of ε_0 (computed with the background velocity). $\varepsilon_0 = 0.5$ (solid gray), $\varepsilon_0 = 0.25$ (dashed) and $\varepsilon_0 = 0.125$ (solid) are plotted. For, $\varepsilon_0 = 0.125$, the zero values correspond to places where L_{22}^{*,ε_0} is negative and V_h cannot be computed.

less. Indeed, the effective $\mathbf{L}^{*,\varepsilon_0}$ becomes locally negative and cannot be used anymore. In Fig. 26, we show cross-sections in the quantity V_h, the sound velocity in an isotropic fluid, $V_h = \sqrt{\kappa^{*,\varepsilon_0} L_{22}^{*,\varepsilon_0}}$ for different ε_0. To compute ε_0, we used the background air λ_{min}. When ε_0 is such that the Helmholtz resonance wavelength is filtered out by the homogenization filter, i.e for large ε_0, the effective medium can be computed. However, the resonance cannot be obtained in the effective medium in that case. Lowering ε_0, $\mathbf{L}^{*,\varepsilon_0}$ becomes locally negative and the effective medium cannot be obtained anymore.

8.4 A 3-D geological model

Numerical simulation of seismic wave propagation in 3-D geological media can be extremely challenging. First, meshing geological structures usually requires huge efforts for both seismologists and computers: seismologists have to make sure that the geological structures in study (e.g. horizons, faults, intrusions, cracks, etc) verify all the geological rules (e.g. Caumon et al., 2009; Wellmann & Caumon, 2018) and computers then run meshing algorithms which can possibly requires considerable convergence time or even fail in providing a result, especially when dealing with hexahedra. Second, the obtained mesh can contain extremely small elements because of the complexity of the geological structures to be honored and/or the inefficiency of the meshing algorithm, yielding to gigantic, sometimes prohibitive, computational cost for just a single wavefield simulation. In this section, we illustrate these issues and show how the homogenization enables to overcome most of them. To do so, we use the SEG-EAGE overthrust model (Fig. 27a) as a case-study.

The SEG-EAGE overthrust model is $20\,\text{km} \times 20\,\text{km} \times 4\,\text{km}$ large. It is made of twelve faulted and folded layers. All of them are isotropic. The P-wave velocity ranges from $2\,500\,\text{ms}^{-1}$ to $6\,000\,\text{ms}^{-1}$; the S-wave velocity ranges from $1\,600\,\text{ms}^{-1}$ to $3\,500\,\text{ms}^{-1}$ (Fig. 27a). To perform wave propagation simulations in such a medium, the finite-difference method can be considered at the price of using an extremely small space-step to capture the effect of the discontinuities. Finite-element methods are more suitable for taking discontinuities into account. This kind of methods relies on meshing the medium with simple shapes like tetrahedra, hexahedra, pyramids, prisms, or a mix of those. Because tetrahedra enable the maximum flexibility, we use them to mesh the overthrust (Fig. 27a') and we rely on a mass-lumped finite-element method (Geevers et al., 2019) to compute seismic wave propagation. After an important work of building the best possible mesh, using various surface and volume meshing algorithms in a row (Pellerin et al., 2014; Si, 2015; Kononov et al., 2012) to benefit from the relevant features of each of them, we obtain $75.5\,\text{cm}$ for the inner-sphere radius of the smallest element. Such a small value leads to a small time-step within the wave propagation simulation, for numerical stability reasons. Computing a $12\,\text{s}$ long wavefield (hereafter denoted by $\mathbf{u}^{\text{ref}}$) for a single $f_0 = 3.125\,\text{Hz}$ Ricker source therefore requires 12.6 days on 40 Skylake cores.

Let us now compute the effective overthrust medium. To do so, we use a tetrahedral finite-element method to solve the cell problem (178) and (179). This problem

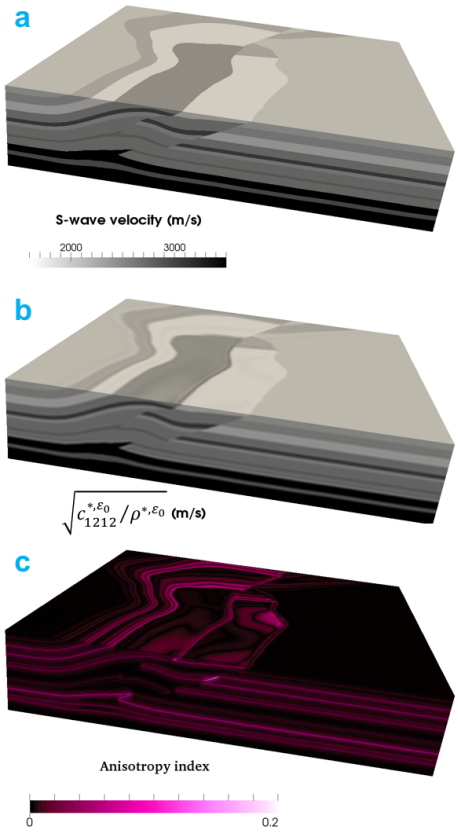

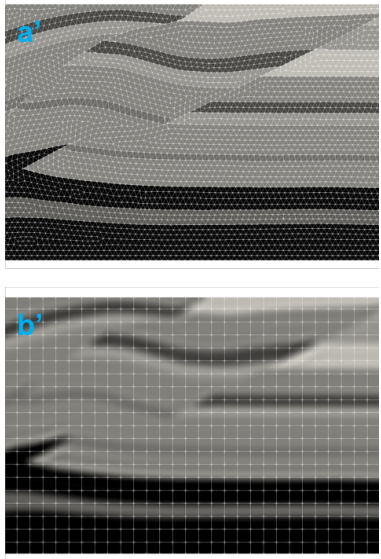

Figure 27: a: S-wave velocity structure of the overthrust model. a': Zoom in a lateral border of the model meshed with tetrahedra. b: The homogenized version of the model; the plotted quantity is the SH-wave velocity. b': Zoom in a lateral border of the homogenized model meshed with hexahedra. c: Total anisotropy of the homogenized overthurst.

is static, so there is no time-step involved and small elements in the mesh do not lead to computational limitations. The main difficulty when solving the cell problem is to handle the large memory requirement: degree-3 polynomials in 16 391 195 tetrahedra (10 904 725 in the model itself along with 5 486 470 mirrored elements to get a solution everywhere, see section 7.2) indeed means a very large linear system to solve. We therefore cut the model into 200 overlapping subdomains, each of them being treated independently from the others (Capdeville et al., 2015; Cupillard & Capdeville, 2018). λ_{min} and ε_0 are set to 200 m and 0.75, respectively, so $\lambda_0 = 150\,m$. In this configuration, the whole computation (i.e. the resolution of the cell problem followed by the filtering of the stress and strain concentrators, see steps 1 and 2 in section 6.1.5) requires 3 hours and 100 Gb on a single PowerEdge M610 for each subdomain. The result is shown in Fig. 27b and c.

By construction, the homogenized overthrust is smooth: it has no spatial variations smaller than λ_0. Computing waveforms in it therefore is very light: the mesh no longer needs to honor geological structures, and the size of the elements is constrained only by λ_0. Fig. 27b' shows a zoom in a regular hexahedral mesh of the homogenized overthrust. All the elements are 200 m^3 large. They are used in a degree-6 SEM (Cupillard et al., 2012) to compute the zeroth-order displacement $\mathbf{u}^0$ corresponding to the wavefield $\mathbf{u}^{\text{ref}}$ generated in the original overthrust model. The computation cost of the spectral-element simulation is $4\,163\,s$ on two Xeon Gold 6130 processors, which is 260 times less than the computation cost required for $\mathbf{u}^{\text{ref}}$. A comparison between $\mathbf{u}^0$ and $\mathbf{u}^{\text{ref}}$ at a given point in space is shown in Fig. 28. The error $\sqrt{\frac{\int(\mathbf{u}^{\text{ref}}-\mathbf{u}^0)^2 dt}{\int(\mathbf{u}^{\text{ref}})^2 dt}}$ at this point is $8.73\,\%$. Such an error averaged over 200 randomly-positioned points is $7.57\,\%$.

Using the same regular hexahedral mesh, we perform a spectral-element simulation in the original overthrust model. In this case, the geological structures are not honored by the mesh. They are smoothed by the numerical method itself, which is not a physical smoothing. As a consequence, the obtained wavefield $\mathbf{u}^{\text{brutal}}$ does not match $\mathbf{u}^{\text{ref}}$. The error between the two wavefields reaches $21.8\,\%$. Refining the regular mesh (using $150\,m^3$, $120\,m^3$, $100\,m^3$, $80\,m^3$ and $60\,m^3$ large elements), the error decreases but the computation cost increases drastically, as shown in Fig. 29. This figure also shows that the refinement has no impact on the wavefield computed in the homogenized medium. This is because all the heterogeneities of the medium are properly captured by the coarsest mesh (i.e. $200\,m^3$ large elements).

8.5 Rotational receivers corrector

From Sec. 4.1.5 and Figs. 4 and 9, we observed that to the leading order, the wavefield, i.e. displacement (and their time derivatives, such as velocities and accelerations) is smooth while wavefield gradients like strain and rotation (and their time derivatives, such as strain rate and rotation rate) are not smooth. A direct consequence of this observation is the relation between data collected in the field and synthetics derived from numerical methods. Here we present an example from the G Ring laser in Wettzell, Germany which records the vertical component of rotation

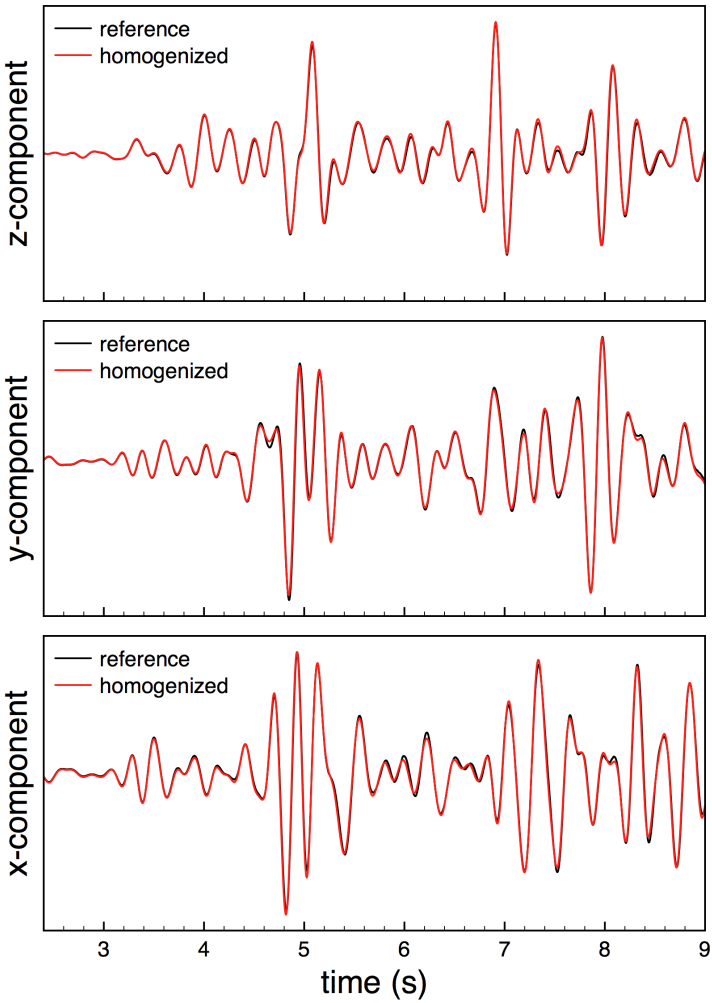

Figure 28: Comparison between $\mathbf{u}^{\text{ref}}$ (black) and $\mathbf{u}^{0}$ (red) at a randomly-chosen point in space. Many wiggles are observed because there is no absorbing boundaries in the two simulations.

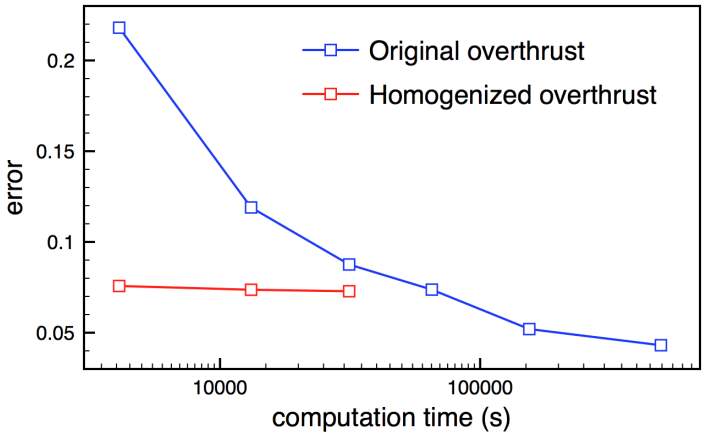

Figure 29: Error of $\mathbf{u}^{\text{brutal}}$ (blue) and $\mathbf{u}^0$ (red) with respect to $\mathbf{u}^{\text{ref}}$. Both $\mathbf{u}^{\text{brutal}}$ and $\mathbf{u}^0$ are computed using a regular hexahedral mesh within a spectral-element method. The error of these two wavefields is plotted as a function of the computation time associated with the size of the hexahedra ($200\,m^3$, $150\,m^3$, $120\,m^3$, $100\,m^3$, $80\,m^3$ and $60\,m^3$).

rates. A collocated seismometer also measures the respective displacements.

The Earth's crust is highly heterogeneous and it is impossible to have a complete information on this heterogeneity. Despite this, we can model very long period surface waves using PREM with good accuracy because per the theory of homogenization, displacements, velocities and accelerations are not sensitive to small-scale structures. For the wavefield gradient measurements, however, small-scales are as important as the large-scales: the effect of the structure, which we call the corrector, appears at the order 0 for the wavefield gradients (see (104) and (185)) whereas it only appears at the order 1 for the wavefield (see (95) and (186)). This implies that, in order to model rotation rates, a complete information on the heterogeneity of the crust is needed. Since we do not have such information, the agreement between rotation rates derived in PREM, i. e. without the corrector, and rotation rate data will not be as good as the agreement between displacements. This is the case in Fig. 30, which shows one of several events recorded at Wettzell where the agreement between displacements is better compared to the agreement between rotation rates.

One way to resolve this issue is of course, to study the behaviour of small-scale structures at the ring laser and understand how they react to wavefield. The problem with this is that for any given scale on the Earth, we can always find something smaller. The simpler solution comes from (104), repeated below for rotation rates.

$$\dot{\omega}_0^{\varepsilon}(\mathbf{x}_r, t; \mathbf{x}_s) = \dot{\omega}^0(\mathbf{x}_r, t; \mathbf{x}_s) + \mathbf{J}(\mathbf{y}_r) : \dot{\boldsymbol{\epsilon}}^0(\mathbf{x}_r, t; \mathbf{x}_s), \tag{207}$$

where $\dot{\omega}_0^{\varepsilon}$ is the rotation rate data while $\dot{\omega}^0$ and $\dot{\boldsymbol{\epsilon}}^0$ are the rotation rate and the

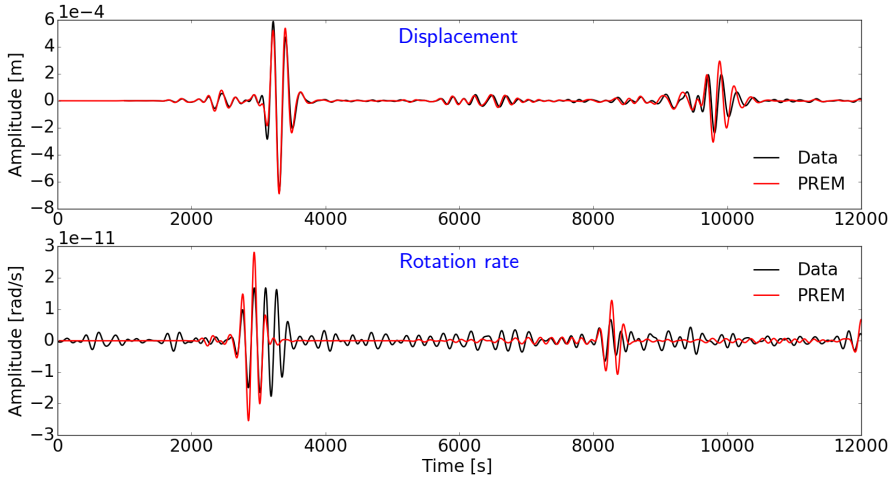

Figure 30: Data vs synthetics derived in PREM for the 201210280304A Queen Charlotte Islands. Top: displacements. Bottom: rotation rates.

strain rate computed in PREM. $\mathbf{x}_s$ denotes the location of the source and $\mathbf{y}_r = \frac{\mathbf{x}_r}{\varepsilon_0}$ denotes the location of the receiver. $\mathbf{J}$ is the corrector and the unknown of the following inverse problem. Since this term depends only on the small-scales located at the receiver, it captures the effect of small-scale structures at that location. Since it does not depend on time or source location, we can invert for $\mathbf{J}$ by solving the over-determined linear problem in the least-squares sense (Tarantola & Valette, 1982) by minimising the L^2 misfit between the synthetics and the data through

$$\mathbf{J} \sim ({}^t\mathbf{F}\,\mathbf{F})^{-1}\,\mathbf{F}\,\delta d, \tag{208}$$

where $\delta d = \dot{\omega}_0^{\varepsilon} - \dot{\omega}^0$ and $\mathbf{F}$ is the matrix with strain rates derived in PREM. Accordingly, $\mathbf{J}$ can be used as a measure of the effect of small-scale structures at the receiver location.

For the ring laser, we invert for $\mathbf{J}$ using 32 events and use it to correct the synthetic rotation rates, i.e. we add the second term on the right-hand side of (207) to the rotation rates derived in PREM. To truly assess the quality of our results, we use the $\mathbf{J}$ to also correct rotation rates not used for the inversion.

From Fig. 31, it can be seen that the agreement between the corrected rotation rates are a better match to data compared to the rotation rates in PREM, also for events not previously used in the inversion. Disagreements are still present but they stem from the fact that the method is asymptotic and implies some unavoidable errors.

Note that correction is needed not just for point-measured wavefield gradient measurements but also for array-derived wavefield gradient measurements. The full study on this topic can be found in Singh et al. (2020).

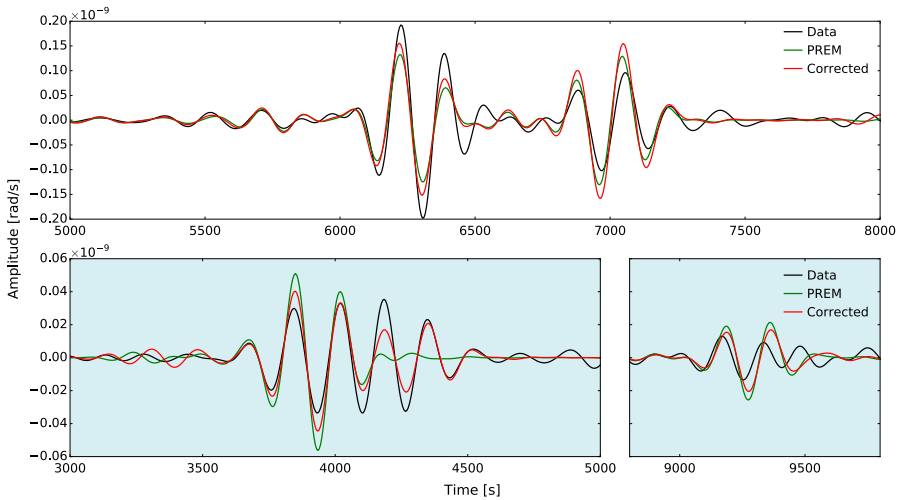

Figure 31: Rotation rates. Top: 201611131102A South Island, New Zealand. One of the 32 events that are used to invert for the coupling tensor **J**. Bottom: 201210280304A Queen Charlotte Islands. An event from the validation data set. It is shown in blue to indicate that this event has not been used for the inversion. Data, synthetic and corrected rotation rates are given in black, green and red respectively.

8.6 Full Waveform Inversion (FWI)

One of the most interesting and promising applications of the homogenization is for the inverse problem. In the inverse problem, the objective is to retrieve information about the medium from seismic data. One of the critical issues, in that case, is the non-uniqueness of the solution. Indeed, we can distinguish two main approaches to solve seismic inverse problems: a global approach and a local approach. In a global approach, the objective is to sample the possible model space and to give statistics about all possible solutions. This is the Bayesian global search method. It is a good solution to handle ill-posed problems such as seismic inverse problems. Unfortunately, the associated numerical cost is out of reach for most applications. The second approach, which is the local optimization, tries to find the best solution based on a least-square minimization scheme. This approach is more commonly used in seismology because it is accessible based on our current numerical power (but is still very challenging). Unfortunately, such method a) can easily be trapped in a local minimum of the misfit function (which measures the difference between synthetic data and real data) and b) does not provide any information about other possible solutions.

In that context, homogenization raises an interesting point: for limited frequency band data, we already know that two models can fit the observed data: the true model and the homogenized version of the true model. Two solutions are already too many for local inversion methods and only one can be found. This aspect is discussed in Capdeville and Métivier (2018) and it appears that the only solution that can be found is the homogenized model: indeed, the true model belongs to an infinite dimension space (we would need an infinite set of parameters, or at least an unknown set of parameters, to describe the true micro-scale model), whereas the homogenized model lives in a finite (known) dimension space. The only possibility is therefore to find the homogenized model and not the true model.

Setting up a basis for the homogenized model space is not trivial and is only possible for layered media (Capdeville et al., 2013). For higher dimensions, we need to set a parameterization such that the model space can contain the homogenized space. The inverted model then needs to be projected into the homogenized model space using a homogenization operator.

In the following, we show a simple 2-D elastic full-waveform inversion (FWI) example. The objective is to show that inversion cannot retrieve the true model but can only find its homogenized version. We first generate synthetic data with a good coverage setting of the area we want to image. The geometry of the sources, the receivers and the heterogeneity is shown in Fig. 32a and Fig. 32c and in Tab. 3. The sources are single forces point sources, using a Ricker source time function with a maximum frequency such that the background $\lambda_{\min}$ is the one used to measure distances as shown in Fig. 32a (this example is dimensionless). An example of the energy wavefield propagating in the domain to generate the data as well as the SEM mesh used is displayed in Fig. 32b. This elastic model (the target model) voluntarily contains heterogeneities of scales much smaller than the minimum wavelength. For example, the slow heterogeneity layers “d” around circle “A” has a thickness of

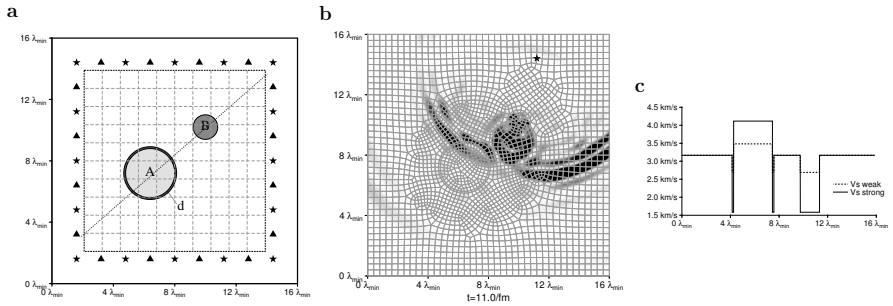

Figure 32: a: Setting of the numerical experiment. The location of sources (stars) and receivers (triangles) are shown. The gray dashed lines represent the elements of an inversion mesh used for that example. The dotted line is the cross-section line used for panel c. b: kinetic energy snapshot for one of the sources shown by the star. c: V_S cross-section along the dotted line in the panel a for weak and strong heterogeneity models. Only the "weak" heterogeneity case is used here.

	V_P (km/s)	V_S (km/s)	ρ (10^3kg/m^3)
background	5.6	3.17	2.61
Circular inclusions, weak heterogeneities case:			
A	6.27	3.48	2.73
B & d	4.85	2.69	2.47

Table 3: Material properties used in the inversion test.

$\lambda_{\text{min}}/8$. Knowing that a FWI has, at best, a resolution of $\lambda_{\text{min}}/2$, the inversion has no chance to recover such a thin layer based on those data. This simple example could mimic a damage zone around an iron bar in concrete. It is a representative example of most real applications: there are always scales much smaller than the minimum wavelength of the data.

To invert the full waveform, we rely on the Gauss-Newton iterative least-square optimization scheme (Pratt et al., 1998). To describe the inverted model, we rely on a piece-wise polynomial basis for the spatial parameterization. More precisely, a square inversion sub-domain $\boldsymbol{\mathcal{I}} \subset \boldsymbol{\Omega}$ is chosen and divided into $n \times n$ non overlapping elements:

$$\boldsymbol{\mathcal{I}} = \cup_{e=1}^{n^2} \boldsymbol{\mathcal{I}}_e^n \, .$$

An example of inversion the domain $\boldsymbol{\mathcal{I}}$ and the associated inversion mesh for $n = 10$ is shown in Fig. 32a. For each element $\boldsymbol{\mathcal{I}}_e^n$, similar to what is done in SEM, elastic parameters and density are represented using a 2-D tensorial product polynomial approximation of degree N in each direction. This defines the parameterization $\boldsymbol{\mathcal{P}}_n^N(\boldsymbol{\mathcal{I}})$ ($n \times n$ elements of degree $N \times N$). We do not impose the continuity of

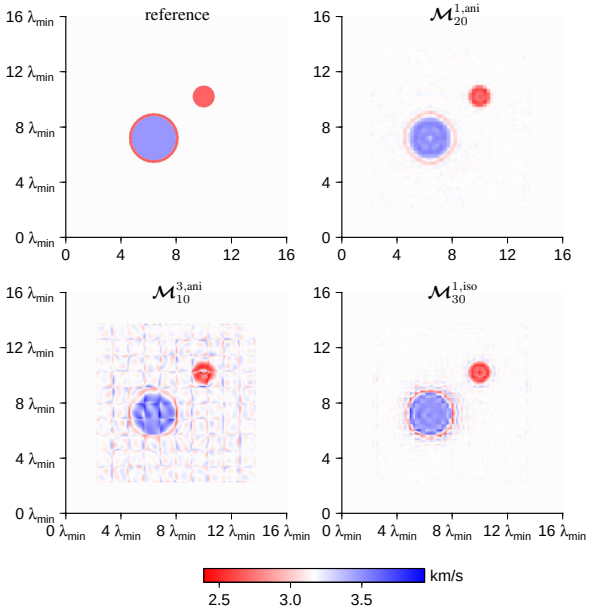

Figure 33: Raw FWI inversion results. V_S for the reference model (upper left panel), raw V_S inversion results for the $\boldsymbol{\mathcal{M}}_{20}^{1,\mathrm{ani}}$ parameterization (upper right panel), $\boldsymbol{\mathcal{M}}_{10}^{3,\mathrm{ani}}$ (lower left panel), and $\boldsymbol{\mathcal{M}}_{30}^{1,\mathrm{iso}}$ (lower right panel) parameterizations are plotted. For $\boldsymbol{\mathcal{M}}_{20}^{1,\mathrm{ani}}$ and $\boldsymbol{\mathcal{M}}_{10}^{3,\mathrm{ani}}$, V_S is the based on the isotropic projection of the anisotropic elastic tensor.

the fields between elements, which implies that $\boldsymbol{\mathcal{P}}_n^N(\boldsymbol{\mathcal{I}})$ has $n^2 \times (N+1)^2$ degrees of freedom for each scalar. We perform three different inversions, each of them using a different parameterization:

- $\boldsymbol{\mathcal{M}}_{30}^{1,\mathrm{iso}}$: $\boldsymbol{\mathcal{P}}_{30}^{1}(\boldsymbol{\mathcal{I}})$ with ρ, V_P and V_S;
- $\boldsymbol{\mathcal{M}}_{10}^{3,\mathrm{ani}}$: $\boldsymbol{\mathcal{P}}_{10}^{3}(\boldsymbol{\mathcal{I}})$ with ρ and $\mathbf{c}$;
- $\boldsymbol{\mathcal{M}}_{20}^{1,\mathrm{ani}}$: $\boldsymbol{\mathcal{P}}_{20}^{1}(\boldsymbol{\mathcal{I}})$ with ρ and $\mathbf{c}$;

These 3 parameterizations have roughly the same number of free parameters (unknowns), $30^2 \times 2^2 \times 3 = 10800$ for $\boldsymbol{\mathcal{M}}_{30}^{1,\mathrm{iso}}$, $10^2 \times 4^2 \times 7 = 11200$ for $\boldsymbol{\mathcal{M}}_{10}^{3,\mathrm{ani}}$ and $20^2 \times 2^2 \times 7 = 11200$ for $\boldsymbol{\mathcal{M}}_{20}^{1,\mathrm{ani}}$.

The raw results of the inversions are shown in Figs. 33 and 34. From the figures it can be seen that the results make sense, but they are different and with a significant noise (it is striking on the cross-section in Fig. 34). The impact of the parameterization choice on the results is obvious. Nevertheless, the three inversion results explain the data equally well. Moreover, their ability to model data that have not been used in the inversion is equally good. In other words, the three results are equally good.

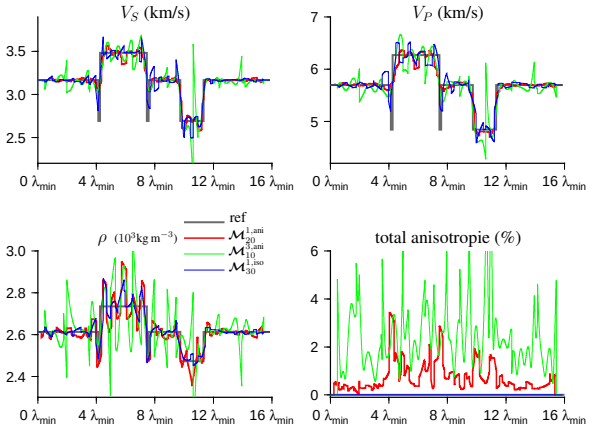

Figure 34: FWI raw inversion results. Cross-sections along the dotted line shown in Fig. 32a, for the reference model ("ref") and for the raw inversion results for the $\mathcal{M}_{30}^{1,\mathrm{iso}}$, $\mathcal{M}_{20}^{1,\mathrm{ani}}$ and $\mathcal{M}_{10}^{3,\mathrm{ani}}$ parameterizations. V_S, V_P, ρ and the total anisotropy are presented. For anisotropic parameterizations, V_P, V_S and the total anisotropy are defined in Sec. 6.1.

We then homogenize the three different results as well as the target model and compare them in Figs. 35 and 36. It appears that all results, once homogenized, are the same and fit the homogenized target model very well. Interestingly, the isotropic inversion, once homogenized, manages to reproduce the necessary effective anisotropy. This is a manifestation of the non-uniqueness of small scales: the inversion was able to find small scales in the parameterization (mainly due to discontinuities between the elements in the parameterization) that have nothing to do with the fine scales in the true model but produce the same anisotropy once homogenized. Through this example, we numerically confirm that results for FWI with a limited frequency band data is at best, the homogenized version of the true model.

This result has important consequences for the FWI design but also the interpretation of the results. It opens the door to a new inverse problem for image interpretation: the downscaling (Hedjazian et al., 2020). A more complete study and discussion about this topic can be found in Capdeville and Métivier (2018).

9 Discussion and conclusions

We have presented an introduction to the two-scale non-periodic homogenization method for the elastic and acoustic wave equations. It is based on the classical asymptotic two-scale homogenization method for periodic or stochastic media. Geological media are neither periodic nor stochastic, but still multi-scale. The objective of the method introduced here is to fill the gap, for two-scale homogenization methods, between the periodic or stochastic media cases and multi-scale deterministic

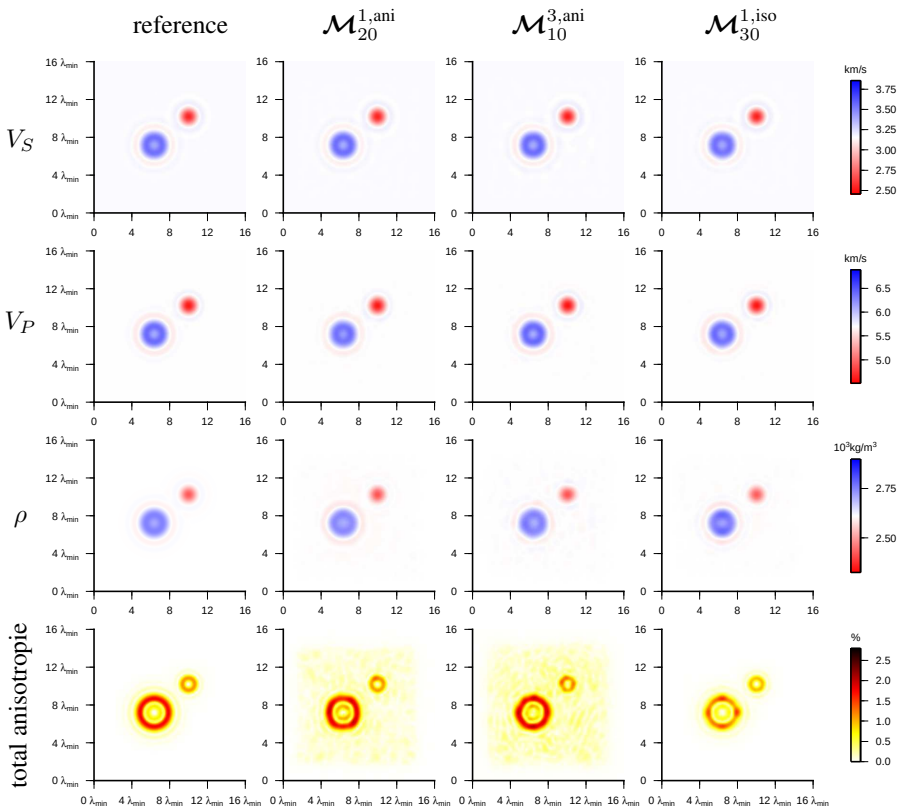

Figure 35: FWI test reference model and three different inversion results, all homogenized with $\varepsilon_0 = 1$. V_S, V_P, ρ and the "total anisotropy" are presented (lines of panels from top to bottom, respectively). Reference, $\mathcal{M}_{20}^{1,\mathrm{ani}}$, $\mathcal{M}_{10}^{3,\mathrm{ani}}$ and $\mathcal{M}_{30}^{1,\mathrm{iso}}$ inverted models are plotted (left to right columns of panels, respectively). V_S, V_P, and the "total anisotropy" are defined in Sec. 6.1

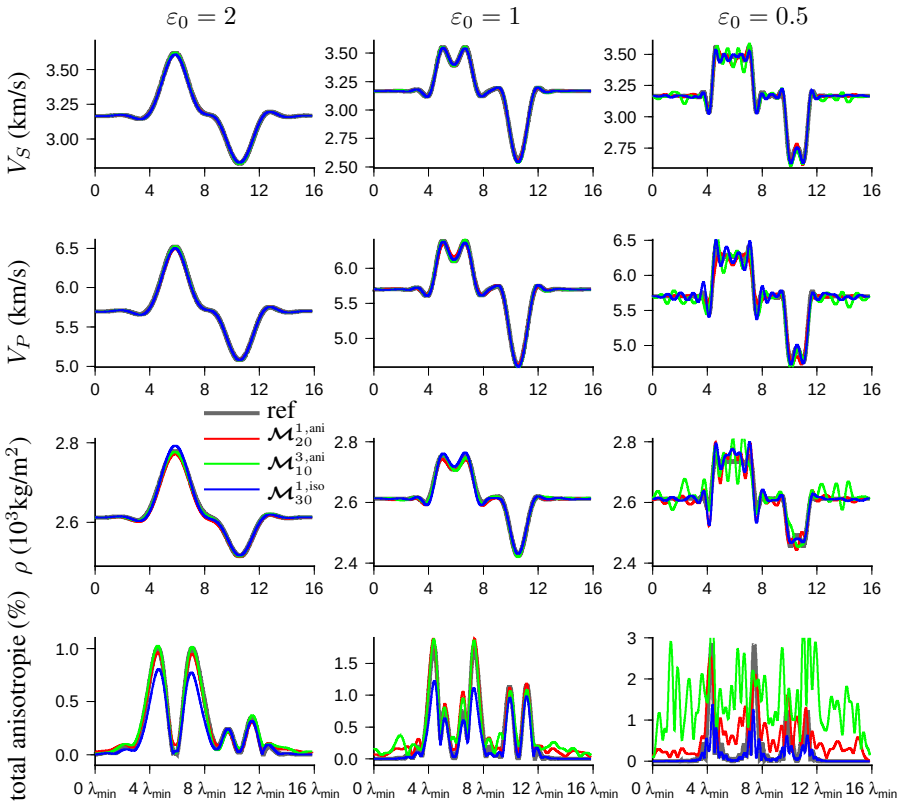

Figure 36: Weak contrast circular inclusion test reference and homogenized inversion results. Cross-sections along the dotted line in Fig. 32a for the reference model ("ref") and for the inversion results for the $\mathcal{M}_{30}^{1,\mathrm{iso}}$, $\mathcal{M}_{20}^{1,\mathrm{ani}}$ and $\mathcal{M}_{10}^{3,\mathrm{ani}}$ parameterizations are represented. Three different values of ε_0 are used ($\varepsilon_0 = 2$, 1 and 0.5). V_P, V_S and the "total anisotropy" are defined in Sec. 6.1.

media with no-scale separation case. In general, homogenization methods require a micro-scale (e.g. the periodic cell) and a macro-scale (e.g. the whole domain). For geological media, there is no scale separation and there is no simple way to tell what is a small scale and what is a large scale. Nevertheless, in the dynamic case (for the wave equations), another scale is present which makes it possible to separate the scales: the minimum wavelength of the propagating wavefield $\lambda_{\min}$. Using this quantity as a scale separator here, we have developed and presented an extension of the two-scale homogenization to the non-periodic case, valid for geological media.

Compared to the classical periodic case, one of the weaknesses of the non-periodic homogenization is that it does not have its mathematical rigor, i.e. no convergence theorem exists. There is, therefore, no warranty that the method works for every case, and indeed, the Helmholtz resonator case shows that the method can fail. Nevertheless, the method has been working for the numerous cases treated for the last ten years and sometimes, even beyond the hypothesis of the underlying method as it is the case for the small fluid inclusion case example. The failure of the Helmholtz resonator case can be physically expected: one of the main hypotheses of the non-periodic homogenization is the presence of a minimum wavelength and, amazingly enough, the Helmholtz resonator has none at its eigenfrequency. It is, therefore, not that surprising that the non-periodic homogenization fails in that specific case. We can conclude that the non-periodic homogenization method is robust enough for all media faced in geosciences and non-destructive testing sciences.

Many aspects of the non-periodic homogenization remain to be studied. One of them is that the effective tensor symmetry is not mathematically ensured, even though it is numerically symmetric for most of the cases we have been working on. This may be a sign that the method is not fully general and in the Helmholtz resonator case, for example, the effective medium becomes strongly non-symmetric just before becoming negative. A deeper study of this aspect would be useful. Another aspect that would deserve attention is that of cases for which the minimum wavelength varies strongly from one place to another. This situation is very common in geophysics where a factor 10 between the top and the bottom model wave-speeds is not exceptional. Using the minimum wave speed in such cases is not optimal and a variable filtering solution is needed. Finally, the two-scale homogenization of the seismic source is also needed. The objective, in that case, is to obtain an effective source (that would not be a point source anymore) and the associated correctors. Development in that direction is currently in preparation and will be submitted soon.

Despite the remaining points to be studied, useful non-periodic homogenization tools are already available. Their first obvious application is forward modeling. By removing interfaces in the media, they significantly ease the meshing and often make the modeling possible (when the meshing is impossible). The gain in computing time is often very significant (several orders of magnitude). Nevertheless, the two-scale non-periodic homogenization does not remove all the meshing difficulties: we still have to adapt the mesh size when the dominant wavelength changes significantly (or at least it is best to) and we still have to mesh the free topography (even if it is smoother once homogenized and therefore easier to mesh) and solid-fluid interfaces.

Another important application of the non-periodic homogenization is the inverse problem. We can speculate and check numerically (Capdeville & Métivier, 2018) that the solution of the full waveform inverse problem is, at best, the homogenized version of the true model. This has important consequences for the inverse problem design. For example, trying to explicitly invert for material discontinuities from limited frequency band data is known to be a difficult ill-posed problem. Still, attempts are made to retrieve sharp discontinuities using sophisticated regularizations (e.g. total variation regularization in Y. Lin & Huang, 2014). Nevertheless, based on the homogenization theory, we know that discontinuities map into an effective smooth anisotropic transition. Inverting for such a smooth media is stable and simple: compared to inverting sharp discontinuities, it drastically reduces the non-linearity of the problem. Homogenization can, therefore, drive our way to design inverse problems and help to stabilize them as shown in Capdeville and Métivier (2018). It also raises the question of the interpretation of the FWI images. If the images do not represent the true model but only its effective version, they must be interpreted with care as the homogenization can have counter-intuitive effects. Their interpretation can be seen as another inverse problem: the downscaling inverse problem. It corresponds to trying to find possible small scale models compatible with the effective image obtained from the FWI and some external a-priori information. This inverse problem is highly non-unique can only be tackled with Monte-Carlo type methods (Hedjazian et al., 2020).

To conclude, we hope to have convinced the reader that, even if the non-periodic homogenization method is not trivial, it is worth the effort and will be useful for many research topics in seismology and geophysics.

10 Acknowledgments

The authors would like to thank Cédric Schmelzbach and Mike Afanasiev for their comments, helping to improve the manuscript. This work has benefited from the contributions of many co-authors since 2007: Jean-Jacques Marigo, Laurent Guillot, Philippe Cance, Gaël Burgos, Ming Zhao and Ludovic Métivier. This work was funded by the three ANR (Agence Nationale pour la Recherche) projects (NR-06-BLAN-0283 “MUSE”, ANR-10-BLAN-613 “mémé” and ANR-16-CE31-0022-01 “HIWAI”). Most of the computations were performed using the “Centre de Calcul Intensif des Pays de la Loire” (CCIPL) resources. We thank the European COST action TIDES (ES1401) for fruitful discussions.

References

Abdelmoula, R., & Marigo, J.-J. (2000). The effective behavior of a fiber bridged crack. *J. Mech. Phys. Solids*, *48*(11), 2419–2444.

Afanasiev, M., Boehm, C., May, D., & Fichtner, A. (2016). Using effective medium theory to better constrain full waveform inversion. In *78th eage conference and exhibition 2016*.

Alder, C., Bodin, T., Ricard, Y., Capdeville, Y., Debayle, E., & Montagner, J. (2017). Quantifying seismic anisotropy induced by small-scale chemical heterogeneities. *Geophys. J. Int.*, *211*(3), 1585–1600.

Alkhalifah, T. (2000). An acoustic wave equation for anisotropic media. *Geophysics*, *65*, 1239-1250.

Allaire, G. (1992). Homogenization and two-scale convergence. *SIAM J. Math. Anal.*, *23*, 1482—1518.

Auriault, J.-L., Borne, L., & Chambon, R. (1985). Dynamics of porous saturated media, checking of the generalized law of darcy. *The Journal of the Acoustical Society of America*, *77*(5), 1641–1650.

Auriault, J.-L., & Sanchez-Palencia, E. (1977). Étude du comportement macroscopique d'un milieu poreux saturé déformable. *J. Mécanique*, *16*(4), 575–603.

Babuška, I. (1976). Homogenization and its application. mathematical and computational problems. In *Numerical solution of partial differential equations–iii* (pp. 89–116). Elsevier.

Backus, G. (1962). Long-wave elastic anisotropy produced by horizontal layering. *J. Geophys. Res.*, *67*(11), 4427–4440.

Bensoussan, A., Lions, J.-L., & Papanicolaou, G. (1978). *Asymptotic Analysis of Periodic Structures*. North Holland.

Bodin, T., Capdeville, Y., Romanowicz, B., & Montagner, J.-P. (2015). Interpreting radial anisotropy in global and regional tomographic models. In *The earth's heterogeneous mantle* (pp. 105–144). Springer.

Boutin, C., & Auriault, J. (1990). Dynamic behaviour of porous media saturated by a viscoelastic fluid. application to bituminous concretes. *International journal of engineering science*, *28*(11), 1157–1181.

Boutin, C., & Auriault, J. (1993). Rayleigh scattering in elastic composite materials. *Int. J. of Engng. Sc.*, 1669-1689.

Bowen, R. (1976). *Continuum physics, chap. theory of mixtures.* Academic Press, New York.

Browaeys, J. T., & Chevrot, S. (2004). Decomposition of the elastic tensor and geophysical applications. *Geophys. J. Int.*, *159*, 667-678.

Burgos, G., Capdeville, Y., & Guillot, L. (2016). Homogenized moment tensor and the effect of near-field heterogeneities on nonisotropic radiation in nuclear explosion. *J. Geophys. Res.*, *121*(6), 4366–4389.

Burridge, R., & Keller, J. B. (1981). Poroelasticity equations derived from microstructure. *The Journal of the Acoustical Society of America*, *70*(4), 1140–1146.

Cance, P., & Capdeville, Y. (2015). Validity of the acoustic approximation for elastic waves in heterogeneous media. *Geophysics*, *80*(4), T161–T173.

Capdeville, Y. (2000). *Méthode couplée éléments spectraux – solution modale pour*

la propagation d'ondes dans la terre à l'échelle globale (Unpublished doctoral dissertation). Université Paris 7.

Capdeville, Y., Guillot, L., & Marigo, J. J. (2010a). 1-D non periodic homogenization for the wave equation. *Geophys. J. Int.*, *181*, 897-910.

Capdeville, Y., Guillot, L., & Marigo, J. J. (2010b). 2D nonperiodic homogenization to upscale elastic media for P-SV waves. *Geophys. J. Int.*, *182*, 903-922.

Capdeville, Y., Gung, Y., & Romanowicz, B. (2005). Towards global earth tomography using the spectral element method: a technique based on source stacking. *Geophys. J. Int.*, *162*, 541-554.

Capdeville, Y., & Marigo, J. J. (2007). Second order homogenization of the elastic wave equation for non-periodic layered media. *Geophys. J. Int.*, *170*, 823–838.

Capdeville, Y., & Marigo, J. J. (2008). Shallow layer correction for spectral element like methods. *Geophys. J. Int.*, *172*, 1135-1150.

Capdeville, Y., & Marigo, J.-J. (2013). A non-periodic two scale asymptotic method to take account of rough topographies for 2-d elastic wave propagation. *Geophys. J. Int.*, *192*(1), 163–189.

Capdeville, Y., & Métivier, L. (2018). Elastic full waveform inversion based on the homogenization method: theoretical framework and 2-d numerical illustrations. *Geophys. J. Int.*, *213*(2), 1093–1112.

Capdeville, Y., Stutzmann, E., Wang, N., & Montagner, J.-P. (2013). Residual homogenization for seismic forward and inverse problems in layered media. *Geophys. J. Int.*, *194*(1), 470–487.

Capdeville, Y., Zhao, M., & Cupillard, P. (2015). Fast fourier homogenization for elastic wave propagation in complex media. *Wave Motion*, *54*, 170–186.

Caumon, G., Collon-Drouaillet, P., de Veslud, C. L. C., Viseur, S., & Sausse, J. (2009). Surface-based 3D modeling of geological structures. *Mathematical Geosciences*, *41*, 927-945.

Chaljub, E., Komatitsch, D., Capdeville, Y., Vilotte, J.-P., Valette, B., & Festa, G. (2007). Spectral element analysis in seismology. In R.-S. Wu & V. Maupin (Eds.), *Advances in wave propagation in heterogeneous media* (Vol. 48, p. 365-419). Elsevier.

Cupillard, P., & Capdeville, Y. (2018). Non-periodic homogenization of 3-d elastic media for the seismic wave equation. *Geophys. J. Int.*, *213*(2), 983–1001.

Cupillard, P., Delavaud, E., Burgos, G., Festa, G., Vilotte, J.-P., Capdeville, Y., & Montagner, J.-P. (2012). RegSEM: a versatile code based on the spectral element method to compute seismic wave propagation at the regional scale. *Geophys. J. Int.*, *188*(3), 1203–1220.

David, M., Marigo, J.-J., & Pideri, C. (2012). Homogenized interface model describing inhomogeneities located on a surface. *Journal of Elasticity*, *xx*, xx-xx.

Davit, Y., Bell, C. G., Byrne, H. M., Chapman, L. A., Kimpton, L. S., Lang, G. E., ... others (2013). Homogenization via formal multiscale asymptotics and volume averaging: How do the two techniques compare? *Advances in Water Resources*, *62*, 178–206.

Dumontet, H. (1990). *Homogénéisation et effets de bords dans les materiaux composites* (Unpublished doctoral dissertation). Univertité Paris 6.

Dziewonski, A. M., & Anderson, D. L. (1981). Preliminary reference Earth model. *Phys. Earth Planet. Inter.*, *25*, 297–356.

Engquist, B., & Souganidis, P. E. (2008). Asymptotic and numerical homogenization. *Acta Numerica*, *17*, 147–190.

Faccenda, M., Ferreira, A. M., Tisato, N., Lithgow-Bertelloni, C., Stixrude, L., & Pennacchioni, G. (2019). Extrinsic elastic anisotropy in a compositionally heterogeneous earth's mantle. *J. Geophys. Res.*, *124*(2), 1671–1687.

Festa, G., & Vilotte, J.-P. (2005). The newmark scheme as velocity-stress time-staggering: an efficient implementation for spectral element simulations of elastodynamics. *Geophys. J. Int.*, *161*, 789-812.

Fichtner, A., & Hanasoge, S. M. (2017). Discrete wave equation upscaling. *Geophys. J. Int.*, *209*(1), 353–357.

Fichtner, A., Kennett, B. L., & Trampert, J. (2013). Separating intrinsic and apparent anisotropy. *Physics of the Earth and Planetary Interiors*, *219*, 11–20.

Francfort, G. A., & Murat, F. (1986). Homogenization and optimal bounds in linear elasticity. *Arch. Rational Mech. Anal.*, *94*(4), 307–334.

Geevers, S., Mulder, W. A., & van der Vegt, J. J. (2019). Efficient quadrature rules for computing the stiffness matrices of mass-lumped tetrahedral elements for linear wave problems. *SIAM journal on scientific computing*, *41*(2), A1041–A1065.

Giorgi, E. D. (1984). G-operators and γ-convergence. In *Proceedings of the international congress of mathematicians (warsazwa, august 1983)* (p. 1175-1191). PWN Polish Scientific Publishers and North Holland.

Giorgi, E. D., & Spagnolo, S. (1973). Sulla convergenza degli integrali dell energia per operatori ellittici del secondo ordine. *Boll. Un. Mat. It.*, 191-411.

Gold, N., Shapiro, S. A., Bojinski, S., & Müller, T. M. (2000). An approach to upscaling for seismic waves in statistically isotropic heterogeneous elastic media. *Geophysics*, *65*(2), 1837-1850.

Grechka, V. (2003). Effective media: A forward modeling view. *Geophysics*, *68*(6), 2055-2062.

Guillot, L., Capdeville, Y., & Marigo, J. J. (2010). 2-D non periodic homogenization for the SH wave equation. *Geophys. J. Int.*, *182*, 1438-1454.

Hashin, Z. (1972). Theory of fiber reinforced materials. *NASA Report No. CR1974*.

Hashin, Z., & Shtrikman, S. (1962). On some variational principles in anisotropic and nonhomogeneous elasticity. *Journal of the Mechanics and Physics of Solids*, *10*(4), 335–342.

Hedjazian, N., Capdeville, Y., & Bodin, T. (2020). Multiscale seismic imaging with inverse homogenization. *Geophys. J. Int.*, *submitted*(0), 0–0.

Hill, R. (1965). A self–consistent mechanics of composit materials. *J. Mech. Phys. Solids*, *13*, 213–222.

Igel, H. (2017). *Computational seismology: a practical introduction*. Oxford University Press.

J. Fish, W., & Nagai, G. (2002). Nonlocal dispersive model for wave propagation in heterogeneous media. part 1: One-dimensional case. *Int. J. Num. Methods Engrg.*, *54*, 331-346.

Jordan, T. H. (2015). An effective medium theory for three-dimensional elastic heterogeneities. *Geophys. J. Int.*, *203*(2), 1343–1354.

Komatitsch, D., & Vilotte, J. P. (1998). The spectral element method: an effective tool to simulate the seismic response of 2D and 3D geological structures. *Bull. Seism. Soc. Am.*, *88*, 368-392.

Kononov, A., Minisini, S., Zhebel, E., & Mulder, W. (2012). A 3D tetrahedral mesh generator for seismic problems. In *74th EAGE Conference and Exhibition incorporating EUROPEC 2012* (pp. cp–293).

Lemoult, F., Kaina, N., Fink, M., & Lerosey, G. (2013). Wave propagation control at the deep subwavelength scale in metamaterials. *Nat. Phys.*, *9*(1), 55–60.

Lin, C., Saleh, R., Milkereit, B., & Liu, Q. (2017). Effective media for transversely isotropic models based on homogenization theory: With applications to borehole sonic logs. *Pure and Applied Geophysics*, *174*(7), 2631–2647.

Lin, Y., & Huang, L. (2014). Acoustic-and elastic-waveform inversion using a modified total-variation regularization scheme. *Geophys. J. Int.*, *200*(1), 489–502.

Marigo, J., & Pideri, C. (2011). The effective behavior of elastic bodies containing microcracks or microholes localized on a surface. *International Journal of Damage Mechanics*.

Mechel, F. P. (2013). *Formulas of acoustics*. Springer Science & Business Media.

Meng, S., & Guzina, B. B. (2018). On the dynamic homogenization of periodic media: Willis2019 approach versus two-scale paradigm. *Proceedings of the Royal Society A: Mathematical, Physical and Engineering Sciences*, *474*(2213), 20170638.

Michel, J., Moulinec, H., & Suquet, P. (1999). Effective properties of composite materials with periodic microstructure: a computational approach. *Comput. methods Appl. Mech. Engrg.*, *172*(1), 109–143.

Moulinec, H., & Suquet, P. (1998). A numerical method for computing the overall response of nonlinear composites with complex microstructure. *Comput. Methods Appl. Mech. Engrg.*, *157*(1), 69–94.

Murat, F., & Tartar, L. (1985). Calcul des variations et homogénéisation. In *Homogenization methods: theory and applications in physics (bréau-sans-nappe, 1983)* (Vol. 57, pp. 319–369). Paris: Eyrolles.

Murat, F., & Tartar, L. (1997). Homogénéisation et compacité par compensation, cours peccot au college de france (1977). f. murat, h-convergence, séminaire d'analyse fonctionnelle et numérique de l'université d'alger (1978). f. murat and l. tartar, h-convergence. *Mathematical Modelling of Composites Materials, A. Cherkaev and RV Kohn.(eds.), Progress in Nonlinear Differential Equations and their Applications, Birkhäuser*.

Nassar, H., He, Q.-C., & Auffray, N. (2016). On asymptotic elastodynamic homogenization approaches for periodic media. *Journal of the Mechanics and Physics*

of Solids, *88*, 274–290.

Nevard, J., & Keller, J. B. (1997). Homogenization of rough boundaries and interfaces. *J. Appl. Math*, *67*(6), 1660-1686.

Nguetseng, G. (1989). A general convergence result for a functional related to the theory of homogenization. *SIAM Journal on Mathematical Analysis*, *20*(3), 608–623.

Nissen-Meyer, T., Fournier, A., & Dahlen, F. A. (2007). A two-dimensional spectral-element method for computing spherical-earth seismograms–i. moment-tensor source. *Geophysical Journal International*, *168*(3), 1067–1092.

Owhadi, H., & Zhang, L. (2008). Numerical homogenization of the acoustic wave equations with a continuum of scales. *Computer Methods in Applied Mechanics and Engineering*, *198*(3-4), 397–406.

Papanicolaou, G. C., & Varadhan, S. (1979). Boundary value problems with rapidly oscillating random coefficients. In *Proceedings of conference on random fields, esztergom, hungary, 27* (p. 835-873). North Holland, 198l.

Pavliotis, G., & Campus, S. K. (2004). Homogenization theory for partial differential equations. *Lecture Notes, Department of Mathematics, South Kensington Campus, Imperial College, London*.

Pellerin, J., Lévy, B., Caumon, G., & Botella, A. (2014). Automatic surface remeshing of 3D structural models at specified resolution: A method based on Voronoi diagrams. *Computers and Geosciences*, *62*, 103-116. doi: doi:10.1016/j.cageo.2013.09.008

Pratt, R., Shin, C., & Hicks, G. (1998). Gauss-newton and full newton methods in frequency domain seismic waveform inversion. *Geophys. J. Int.*, *133*, 341–362.

Pride, S. R., Gangi, A. F., & Morgan, F. D. (1992). Deriving the equations of motion for porous isotropic media. *The Journal of the Acoustical Society of America*, *92*(6), 3278–3290.

Sanchez-Palencia, E. (1980). *Non homogeneous media and vibration theory* (No. 127). Berlin: Springer.

Sanchez-Palencia, E. (1986). Elastic body with defects distributed near a surface. In *Homogenization techniques for composite media.* Springer Verlag.

Shapiro, S. A., Schwarz, R., & Gold, N. (1996). The effect of random isotropic inhomogeneities on the phase velocity of seismic waves. *Geophys. J. Int.*, *123*, 783-794.

Si, H. (2015). Tetgen, a Delaunay-based quality tetrahedral mesh generator. *ACM Trans. Math. Softw.*, *41*(2). doi: 10.1145/2629697

Singh, S., Capdeville, Y., & Igel, H. (2020). Correcting wavefield gradients for the effects of local small-scale heterogeneities. *Geophys. J. Int.*, *220*(2), 996–1011.

Tarantola, A., & Valette, B. (1982). Generalized nonlinear inverse problems solved using the least squares criterion. *Rev. Geophys.*, *20*, 219–232.

Tartar, L. (1978). Quelques remarques sur l'homogénéisation proc. of the japan-france seminar 1976. In *Functional analysis and numerical analysis* (p. 469-

482).

Thomsen, L. (1972). Elasticity of polycrystals and rocks. *Journal of Geophysical Research*, *77*(2), 315–327.

Tiwary, D. K., Bayuk, I. O., Vikhorev, A. A., & Chesnokov., E. M. (2009). Comparison of seismic upscaling methods: From sonic to seismic. *Geophysics*, *74*(2), wa3-wa14.

Wang, N., Montagner, J.-P., Fichtner, A., & Capdeville, Y. (2013). Intrinsic versus extrinsic seismic anisotropy: The radial anisotropy in reference earth models. *Geophysical Research Letters*, *40*(16), 4284–4288.

Watt, J. P. (1988). Elastic properties of polycrystalline minerals: Comparison of theory and experiment. *Physics and Chemistry of Minerals*, *15*(6), 579–587.

Wellmann, F., & Caumon, G. (2018). 3-d structural geological models: Concepts, methods, and uncertainties. In *Advances in geophysics* (Vol. 59, pp. 1–121). Elsevier.

Willis, J. R. (1981). Variational principles for dynamic problems for inhomogeneous elastic media. *Wave Motion*, *3*, 1-11.

Willis, J. R. (1983). The overall elastic response of composite materials. *J. Appl. Mech.*, *50(4b)*, 1202-1209.

Willis, J. R. (1985). The nonlocal influence of density variations in a composite. *International Journal of Solids and Structures*, *21*(7), 805–817.

Willis, J. R. (1997). Dynamics of composites. In *Continuum micromechanics* (pp. 265–290). Springer.

Willis, J. R. (2009). Exact effective relations for dynamics of a laminated body. *Mechanics of Materials*, *41*(4), 385–393.